Chemo-Mechanics of Alloy-Based Electrode Materials for Li-Ion Batteries

A Dissertation
Presented to
The Academic Faculty

by

Yifan Gao

In Partial Fulfillment
of the Requirements for the Degree
Doctor of Philosophy in the
School of Mechanical Engineering

Georgia Institute of Technology
August, 2013

Chemo-Mechanics of Alloy-Based Electrode Materials for Li-Ion Batteries

Approved by:

Dr. Min Zhou, Advisor
G. W. W. School of Mechanical Engineering
Georgia Institute of Technology

Dr. David McDowell
G. W. W. School of Mechanical Engineering
Georgia Institute of Technology

Dr. Ting Zhu
G. W. W. School of Mechanical Engineering
Georgia Institute of Technology

Dr. Gleb Yushin
School Materials Science and Engineering
Georgia Institute of Technology

Dr. Yi Cui
School Materials Science and Engineering
Stanford University

Date Approved: May 10, 2013

To my dad, my mom, and my grandma

ACKNOWLEDGEMENTS

I am deeply grateful to my advisor, Dr. Min Zhou, for his guidance, patience, and support. His enthusiasm for science and his insight into research are inspiring. His emphasis on fundamental training, critical thinking, and clear technical writing helps and motivates me to become a more competent researcher and a better educated person.

I would like to thank my thesis committee members, Dr. David McDowell, Dr. Ting Zhu, Dr. Gleb Yushin, and Dr. Yi Cui, for their help during my entire PhD research and for their insightful comments on my thesis. I would also like to thank my collaborators, especially Dr. Liangbing Hu and Dr. Hui Wu, for the opportunities of working together and enjoying enlightening discussions.

I would like to thank many members of our lab–Ananda Barua, Siddharth Avachat, Yan Li, Chris Lammi, Seokpum Kim, Barrett Hardin, and Jong Boo Jung. I thank Dr. Shuman Xia, Dr. Shan Huang, Dr. Yuan Zhong, and Feifei Fan, for the very helpful discussions. Special thanks to my friends, especially Fan Ming, Chen Li, Wenjie Mai, Cheng Li, Yang Ding, and Chris and Rebecca Gray, for their support, help, and encouragement.

I would like to dedicate this work to my parents, Fei Gao and Qi Li, and my late grandma Kuiyi Zhao. Thank you, dad and mom, for always being there to support me. And thank you, grandma; I know how happy you would be if you could witness what I have done.

Finally, I would like to thank my wife, Yingjie. Thank you for always being there, loving me, and making me feel special.

TABLE OF CONTENTS

LIST OF TABLES

LIST OF FIGURES

SUMMARY

Lithium alloys with metallic or semi-metallic elements are attractive candidate materials for the next-generation rechargeable Li-ion battery anodes, thanks to their large specific and volumetric capacities. The key challenge, however, has been the large volume changes, and the associated stress buildup and failure during cycling. The chemo-mechanics of alloy-based electrode materials entail interactions among diffusion, chemical reactions, plastic flow, and material property evolutions.

In this study, a continuum theory of two-way coupling between diffusion and deformation is formulated and numerically implemented. Analyses based on this framework reveal three major conclusions. First, the stress-to-diffusion coupling in Li/Si is much stronger than what has been known in other electrode materials. Practically, since the beneficial effect of stress-enhanced diffusion is more pronounced at intermediate or higher concentrations, lower charging rates should be used during the initial stages of charging. Second, when plastic deformation and lithiation-induced softening take place, the effect of stress-enhanced diffusion is neutralized. Because the mechanical driving forces tend to retard diffusion when constraints are strong, even in terms of operational charging rate alone, Li/Si nano-particles are superior to Li/Si thin films or bulk materials. Third, the diffusion of the host atoms can lead to significant stress relaxation even when the stress levels are below the yield threshold of the material, a beneficial effect that can be leveraged to reduce stresses because the host diffusivity in Li/Si can be non-negligible at higher Li concentrations.

A theory of coupled chemo-mechanical fracture driving forces is formulated in order to capture the effect of deformation-diffusion coupling and lithiation-induced softening on fracture. It is shown that under tensile loading, Li accumulates in front of crack tips, leading to an anti-shielding effect on the energy release rate. For a pre-cracked Li/Si thin-film electrode, it is found that the driving force for fracture is significantly lower when the electrode is operated at higher Li concentrations -- a result of more effective stress relaxation via global yielding. The results indicate that operation at higher concentrations is an effective means to minimize failure of thin-film Li/Si alloy electrodes.

1. Introduction

Energy capacity per unit mass or unit volume is a key figure of merit for battery materials. In the quest for much-needed high energy density and high performance rechargeable batteries for vehicles and portable electronics devices, Li alloys have attracted tremendous interest since it offers greater specific and volumetric capacities than graphite (the negative electrode material for most existing batteries) and other candidate materials. One of the main challenges with alloy-based Li-ion battery electrodes, however, has been the large volume changes during lithiation and delithiation. The volume changes can induce stresses and degrade the electrode material in a few cycles [1], an effect that has hindered the practical application of electrodes based on Li-alloys for almost a decade.

Recent efforts to improve the cyclability of Li-alloy based electrodes are highlighted by the utilization of nano-structured materials [2-6], including Si nanowires (NWs) [7], crystalline-amorphous Si core-shell nanostructures [8], sealed Si nanotubes [9], nano-structured carbon/silicon composites [10], double-walled silicon nanotubes [3], and nanopowder-alginate mixture [11]. Thanks to their ability to reduce diffusion-induced stresses (DIS) and to better accommodate inhomogeneous volume changes, these novel materials can withstand hundreds or thousands of charge/discharge cycles and have enabled the envelop of battery life and allowable charging rates to be pushed out every few months.

The mechanical behavior and failure mechanism of nano-sized electrode materials can be distinctly different from those of electrode material with characteristic sizes in the micron or millimeter ranges. For example, bulk and thin film Si electrodes mainly fail through cracking [12, 13]; Si NW electrodes, on the other hand, may degrade through internal void formation [14] and/or surface roughening[5]. Sethuraman et al. [15] measured the evolution of stresses in silicon thin films during electrochemical cycling and showed that the flow stress of lithiated Si decreases as Li concentration increases. The finding suggests that parameters which depend on stress singularities such as the mode I fracture toughness K_{IC} are not very relevant for nanostructured Li/Si electrodes. Instead, plastic (or viscoplastic) flow is an important process that cannot be neglected.

Improving the reliability and performance of nano-sized Li-alloy electrode materials requires a fundamental understanding of the complex chemical-mechanical-electrical characteristics of the underlying physical processes and the interplay of many different factors. The multiscale and multiphysics nature of the phenomena involved makes this both a challenging and interesting endeavor which has attracted the attention of many researchers (e.g. [16-22]). The aim of this research is to investigate the chemo-mechanics of alloy-based electrode materials, especially that of Li/Si electrode materials, by using a continuum-level theory. In this introductory chapter, a brief background review is presented in order to bring out the issues to be investigated in this research.

1.1. Alloy-based electrodes for Li-ion batteries

The concept of lithium ion batteries was first proposed by M. S. Whittingham [23] in the 1970s. Although materials and designs vary, a Li-ion battery always conceptually comprises three major parts: the anode, the cathode, and the electrolyte (Fig 1.1). During the discharge half cycle, lithium ions transfer through the electrolyte and electrons transfer through the external circuit, both from the anode to the cathode. During the charge half cycle, the migration directions of lithium ion and electros reverse, but it is customary to term the negative electrode “anode” and the positive electrode “cathode” for both discharge and charge half cycles.

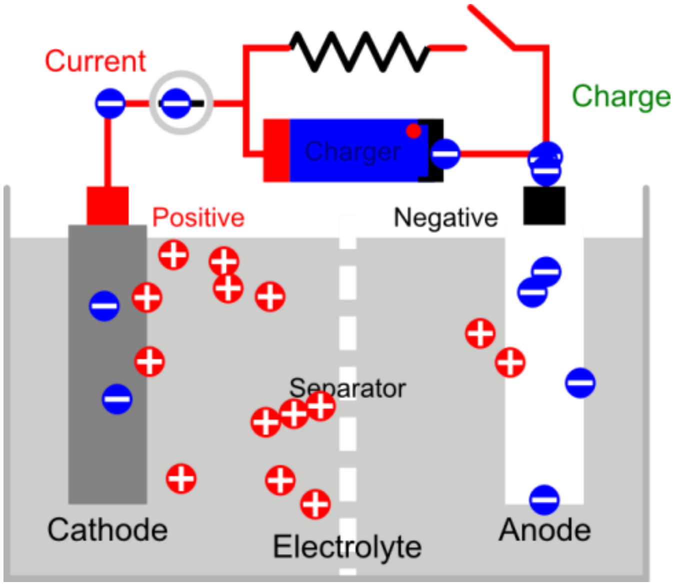

Fig. 1.1 Components of a Li-ion battery. Reproduced from Wikipedia.

The anode material in traditional lithium ion batteries is graphite, which holds one lithium atom per six carbon atoms. The specific and volumetric capacities of Li-alloy based electrodes, on the other hand, are generally ~10 times higher than that of graphite. Among the materials listed in Fig. 1.2, silicon has the highest theoretical capacity of 4,200 mAh g^{-1} and thus attracted the most interest.

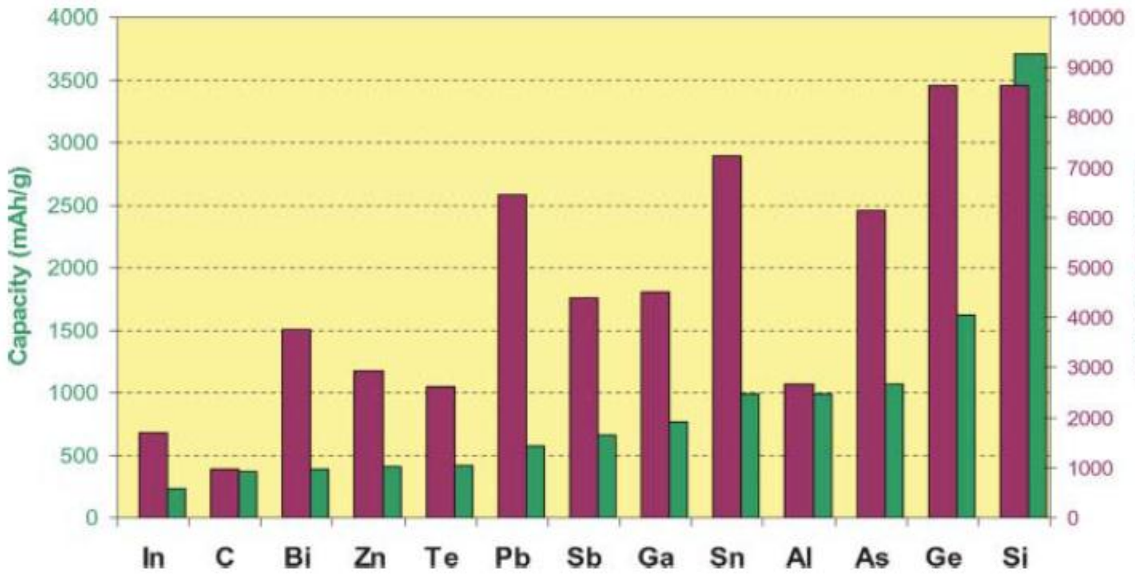

Fig. 1.2 Gravimetric and volumetric capacities for selected alloying reactions. Capacities for graphite are given as references. Reproduced from Ref. [1].

One of the main challenges with alloy-based Li-ion battery electrodes, however, has been large volume changes during lithiation and delithiation. For example, when lithiated at room temperature, silicon-based anodes can expand by up to 311% in volume as Li content is changed from 0 to 4.4 per Si [12]. Graphite anodes in commercial batteries, in contrast, exhibit only ~10% volumetric changes [24]. If the alloy-based active material particles are mechanically constrained by a current collector such as the conductive substrate attached to the electrode or the binder which comprises part of the electrode composite, high stresses develop during charge/discharge cycling. Fig. 1.3 illustrates the cracks generated in thin-film Li/Si electrodes that form due to electrochemical cycling. Similar crack patterns are also seen in other Li-alloy-based electrode material systems, such as Ge [25], Sn [26], and Si-Sn [13].

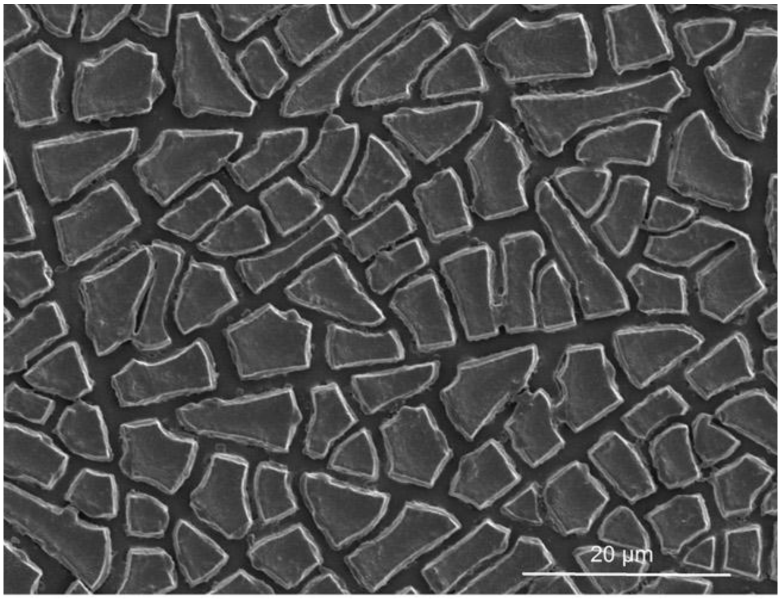

Fig. 1.3 Crack patterns which form due to electrochemical cycling of thin-film Li/Si electrodes. Reproduced from Ref. [27].

Even when mechanical constraints are absent, the inhomogeneity of lithium concentration due to finite lithium diffusivity can still lead to stresses. The buildup of stresses due to composition inhomogeneity during diffusive transport in solid materials is a ubiquitous process seen in many disciplines of science and engineering. Such stresses, called “diffusion-induced stresses” (DIS), has been observed in many areas including oxidation of metals, hydrogen transport in solid-state hydrogen-storage media, dopant diffusion in semiconductor processing, and lithium ion transport in battery electrodes.

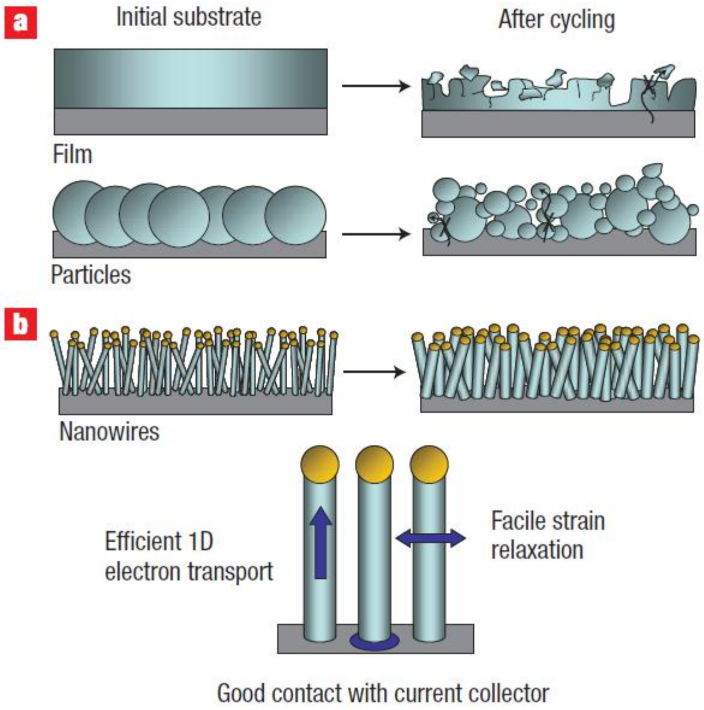

Fig. 1.4 Schematic illustration of morphological changes that occur in Si during electrochemical cycling. (a) The volume of silicon anodes changes by about 300% during cycling. As a result, Si films and particles tend to pulverize during cycling. Much of the material loses contact with the current collector, resulting in poor transport of electrons, as indicated by the arrow. (b) NWs grown directly on the current collector do not pulverize or break into smaller particles after cycling. Rather, facile strain relaxation in the NWs allows them to increase in diameter and length without breaking. This NW anode design has each NW connecting with the current collector, allowing for efficient 1D electron transport down the length of every NW. Reproduced from Ref. [7].

The diffusion-induced stresses due to finite diffusivity can be significantly reduced by decreasing the system dimension [28]. One of the earliest attempts in using silicon nanowires (NWs) as an anode material is made by Chan et al. [7], who achieved the theoretical charge capacity for silicon anodes and maintained a discharge capacity close to 75% of the theoretical maximum, with little fading during cycling. Besides the reduction of stresses, another benefit of using NWs, according to Chan et al. [7], is the maintenance of good electronic contact with the substrate as illustrated in Fig. 1.4.

1.2. Theoretical challenges and recent research trends

While the stress buildup in Li-ion battery electrode materials bears resemblance to the process of thermo-stress development, a phenomenon relatively well-understood, the physics involved in these alloy-based electrodes is much more complex in nature, more challenging to address, and richer in the variety of influencing factors. The reasons not only lie in the fact that the mechanical deformations are much larger, but also arise from the fact that the processes entail interactions among mass diffusion, chemical reactions, non-linear plastic flow and material property evolutions. This richness of physics presents an opportunity for researchers of solid mechanics to explore novel phenomena which are both theoretically interesting and practically important.

Many continuum-level models have been proposed to characterize the buildup and mitigation of stresses, and the associated mechanical failure, in Li-ion battery electrodes. Issues of active studies include concentration-change-induced softening of the alloy materials, inelastic flow, electro-chemical-mechanical coupling, finite deformation, chemical reaction, phase transition, and mass transport. In this section, we provide a simple review of those works that are relevant to this research.

Diffusion-induced stresses

Due to its close relationship with cyclic degradation, diffusion-induced stress in free-standing particle electrodes has been subject to extensive studies [29-33]. By drawing an analogy to the thermal stress problem, Cheng and collaborators analyzed the effect of DIS in battery electrode particles with spherical [29, 30] and cylindrical [31] shapes. They discussed the implications of different charging regimens such as potentiostatic and galvanostatic operations on stress levels [29]. They also identified a dimensionless number that is analogous to the Biot number in heat transfer problems in order to quantify the relative significance of surface kinetics, governed by linearized Butler-Volmer's law, and the bulk diffusion kinetics, governed by the Fick's law [32]. The effect of surface tension on internal stress in spherical particles has been investigated, and it is suggested that the surface effect can significantly reduce the tensile stress in the material when the particle radius is shrank into the nano regime [20].

If the electrode material is constrained by external agencies such as a substrate or current collector, stresses can arise even when the Li concentration is homogeneous. This is the case for thin-film electrodes, in which the active electrode material (e.g., Si or Sn) is deposited on a current collector, usually made of Cu or Ti, via thin-film deposition techniques such as electron beam evaporation or sputtering [15, 34, 35]. To analyze the fracture patterns, Li et al. [27] modified the two-dimensional spring-block model originally proposed by Leung and Neda [36] for the problem of corn starch drying, and successfully explained the experimental observation that cracks are straight with larger islands in thicker films, but show more wiggles with smaller islands in thinner films. The analysis by Li et al. [27] also shows a critical film thickness below which no crack would form in Li/Si thin-film electrodes.

In addition to the findings by Li et al. [27], it turns out that reducing the in-plane dimensions of the islands of active material also mitigates fracture in Li/Si thin-film electrodes [35]. As mentioned before, the stresses in thin-film electrodes arise mainly due to the constraints at the film-substrate interface. Weaker constraints, for example in the form of interfacial sliding, may therefore be beneficial because it helps reduce the stress level. Xiao et al. [35] leveraged this idea by introducing a patterning approach to improve the cycling stability of silicon electrodes. They found an improvement in cycle life when the pattern size is below the critical (7-10 μm) level. To explain the mechanism responsible for their observation, Xiao et al. [35] considered a Si thin film which already contained an array of cracks with spacing L and calculated the minimum crack spacing which is small enough so that no additional crack can be inserted between the existing cracks. The critical spacing thus estimated agreed with the experiments. Later, to analyze the delamination at the Si/Cu interface, a more sophisticated model was developed by Haftbaradaran et al. [37], which leads to yet another length scale that controls the peel-off of the cracked Si film from the Cu substrate.

Plastic deformation and lithiation-induced softening

Although pure silicon in its crystalline or amorphous state is brittle [38], lithiated Si, which is generally amorphous, can undergo significant inelastic deformation. Such a brittle-to-ductile transition of Li/Si is an important embodiment of an effect called “lithiation-induced softening”. There are two aspects of lithiation-induced softening of Li/Si: reduction in yield stress and reduction in elastic modulus as the Li content increases.

In continuum theories, the lithiation-induced changes in mechanical properties have been modeled by assuming that the elastic moduli and yield stress are functions of the local lithium concentration [16, 39, 40], an assumption that is sufficient for capturing most experimental observations with regard to the effects of lithiation-induced softening. More sophisticated theories have also been proposed. For example, it is suggested by Brassart and Suo that the link between mechanical response and electrochemical charging conditions can also be established by reckoning the non-equilibrium driving force $\Omega^{Li}\varsigma$ which is essentially the difference in chemical potentials between the electrode material and the surrounding environment [41, 42]. Here, Ω^{Li} is the partial atomic volume of Li and ς is the osmosis pressure. The key assumption behind this type of treatment is that the concurrent deformation and reaction processes is a non-equilibrium process which is governed by how far the state deviates from thermodynamic equilibrium. Many interesting predictions have been made out from this type treatment, including the prediction that the host under a constant deviatoric stress will flow gradually in response to ramping in the chemical potential, and will ratchet in response to cycling in the chemical potential [41].

Diffusion-deformation two-way coupling

The chemo-mechanical coupling in alloy-based electrode materials involves two aspects, chemical-to-mechanical (CM) coupling and mechanical-to-chemical (MC) coupling: while diffusion induces stresses, stresses can also affect diffusion. Bower et al. [16] developed a comprehensive framework and used it to analyze time-dependent plasticity in thin-film Li/Si. The effect of stress-enhanced diffusion (SED) was analyzed, revealing significant reduction in stress due to a mechanical driving force for diffusion when the deformation is in the elastic regime [43]. This enhancement effect can nevertheless be diminished or even fully reversed when the material deforms plastically [44]. Haftbaradaran and Gao discussed the condition and effect of surface locking due to the modulation effect of stresses on diffusivity [19]. Zhao et al. [45] considered plastic deformation and showed that inelastic flow can significantly alleviate stresses in Li/Si. Numerical frameworks based on the mixed finite element method have also been proposed in order to simulation the deformation-diffusion coupling [18, 46].

Fracture mechanics

Cheng et al. considered a maximum-stress-based fracture initiation criterion [32], and an energy-based criterion [30] that is essentially an electrochemical counterpart of Hasselman's thermal shock model [47]. Based on the concept of cohesive zones, Bhandakkar and Gao [48] developed an analytical model for crack nucleation in an initially crack-free stripe electrode during galvanostatic intercalation and deintercalation by considering a periodic array of cracks in a free-standing thin strip. Li et al. [27] modified the two-dimensional spring-block model originally proposed by Leung and Neda [36] for the problem of corn starch drying, and successfully explained the experimental observation that cracks are straight with larger islands in thicker films, but show more wiggles with smaller islands in thinner films. Xiao et al. [35] considered a Si thin film which already contained an array of cracks with spacing L and calculated the critical L which is small enough so that no additional crack can be inserted between the existing cracks. All of these models consider only the effect of diffusion-induced deformation and stress, but not the converse effect of mechanical-to-chemical coupling.

Bower and Guduru [46] and Grantab and Shenoy [49] used the cohesive finite element method to analyze the fracture behavior of Li/Si electrodes. Both analyses consider the two-way coupling between diffusion and deformation, by using the mixed finite element method [50] or by calculating the pressure gradient from fields in adjacent elements [49]. It is found that the two-way coupling can lead to lithium accumulation at the crack tip [49], similar to the accumulation of hydrogen in hydrogen embrittlement problems. Such accumulations could have a significant impact on near-tip stress fields and, consequently, affect fracture [39]. The use of cohesive elements allows fracture propagation to be explicitly tracked with ease, compared with other propagation-tracking techniques such as crack-tip remeshing [51]. When significant plasticity is involved, however, care must be taken when using cohesive finite elements because the critical separation might be comparable or even larger than nano-sized features in the electrodes.

Since lithiated silicon is highly ductile, fracture criteria based on the energy-release-rate seem to be a logical choice for fracture analyses. Hu et al. [52] used the energy release rate and the Griffith condition to study insertion-induced cracking in $LiFePO_4$ particles caused by the mismatch between different phases. Ryu et al. [53] proposed a framework for calculating the energy release rate J for cracks in Si nanowire electrodes and used the framework to study the size dependence of fracture. This theory nevertheless relies on an effective diffusivity D_{eff} which is applicable only when the material deformation is elastic. In order to overcome this shortcoming, Gao and Zhou [39] developed a fully-coupled finite deformation theory for analyzing the coupled mechano-diffusional driving forces for fracture in electrode materials. The detail of the coupled mechano-diffusional driving forces will be the topic of chapter 5.

1.3. Objective, scope, and organization of this thesis

This research aims at understanding the chemo-mechanical characteristics in nano-sized lithium ion battery electrode materials. We focus on the following issues:

1) How does one capture the chemo-mechanical two-way coupling by using a continuum theory and how does one simulate this coupling effectively by using the finite element method?

2) How does the chemo-mechanical two-way coupling affects the stress and concentration profile in an electrode, and how significantly does the coupling affect the battery cyclablility and operational charging rate?

3) How good is the assumption of zero host diffusivity in Li/Si alloys and what is the effect of small but finite host diffusivity on stresses?

4) How does chemo-mechanical coupling, plasticity, and lithiation-induced softening affect fracture and, in turn, battery design?

Chapters 2 and 3 are dedicated to the first issue, by establishing a continuum framework and then by implementing this framework using the mixed finite element method. In chapter 4, issues 2) and 3) are addressed by using the theoretical tool built in chapter 2 and 3. Chapter 5 focuses on the fourth issue, by modifying the existing Rice J-integral theory so that the theory can capture the effect of mechano-diffusional coupling.

2. Theoretical framework of diffusion-deformation coupling

Based on the work by Wu [54], Bower et al. [16], Zhao et al. [45], Cui et al. [40], and Gao et al. [18], this chapter lays out the continuum framework for the coupling between diffusion and large deformation in alloy-based electrode materials.

We begin with a review of relevant experimental observations and atomistic-level results in section 2.1 for two purposes: first, to establish the motivation to extend the existing continuum theories, and second, to delineate the physical phenomena that the new framework must capture. A focus will be given to the Li/Si material which has the highest known theoretical energy storage capacity. For the completion of the picture, experimental phenomena (e.g. amorphization of crystalline Si) that are potentially important but are beyond the scope of this research are also presented. When such phenomena are introduced, discussions on the range of applicability of the theoretical framework are given.

The physical picture and the mathematical formulation of the deformation-diffusion coupling theory are in section 2.2. Analyses, results, and discussions based on theory will be presented in Chapter 4 and Chapter 5.

2.1. Experimental observations and atomistic mechanisms

2.1.1. Lithiation-induced amorphization of crystalline silicon

During the first lithiation half cycle of a crystalline Si (c-Si) electrode, amorphization occurs, leading to an amorphous material structure for subsequent cycles [55]. In-situ TEM studies indicate that the phase transition of c-Si into amorphous Si (a-Si) takes place by advancing a sharp phase boundary towards the c-Si domain which is devoid of lithium [56, 57]. For subsequent lithiation-delithiation cycles, however, there are no more sharp phase boundaries and the lithium concentration profile is smooth and governed by diffusion kinetics [56].

Recent studies show the existence of sharp phase interfaces during the first lithiation half cycle even if the starting material is a-Si [58, 59]. Specifically, lithiation of a pristine a-Si electrode occurs by the movement of a sharp phase boundary between a Li-rich Li/Si alloy phase and a Li-poor pure a-Si phase. For subsequent cycles, however, no more sharp phase boundaries are observed and the lithiation/delithiation process is governed by diffusion kinetics [59], unless the Li/Si electrode is deep lithiated to a very low cutoff voltage to induce recrystallization to the $Li_{15}Si_4$ phase [60-62].

The sharp phase boundaries are harmful because the abrupt change of Li concentrations at those boundaries may induce high levels of stresses [57, 63-65]. Many interesting phenomena, including the anisotropic interface mobility and swelling [57, 66, 67] and the self-limiting lithiation [68, 69], have been observed during the first half-cycle of c-Si. However, practically feasible Li/Si electrodes would be unlikely to be made from c-Si due to the undesirable effects of the sharp boundaries during the first lithiation cycle [63]. These effects can be avoided by starting with a-Si and by allowing electrodes to undergo careful initial “priming” to bring them to amorphous states which will not generate phase boundaries during subsequent usage [59]. Therefore, unless specified otherwise, discussions in this research focus on situations in which the starting material is fully amorphous. Under this condition, neither phase transition nor phase boundary needs to be considered, and the governing kinetics is diffusion instead of phase transition. Theories and models thus formulated are applicable to the operation of primed Li-Si electrodes but not to the initial priming treatment.

2.1.2. Large deformation due to lithiation and delithiation

It is well-established that during lithiation Li-alloy based electrode materials undergo large volumetric changes. Beaulieu et al. measured the thickness change of thin-film Li/Si during cycling, and found that the volumetric change can reach as high as 311% [12]. Atomistic simulations have also reproduced this large volume expansion [70, 71]. Depending on the design, stresses in an electrode may arise via two mechanisms if the starting material is fully amorphized Si. The first is due to Li concentration inhomogeneity arising from the fact that the diffusivity of Li is finite; the second is due to constraining by external agencies such as a substrate or current collector in contact with the electrode.

The stresses during lithiation and delithiation reciprocally affect the overall deformation by inducing elastic or even plastic deformations. In order to isolate the contribution due to the change of lithium concentration itself, the stress-free (SF) deformation is defined as the deformation of a volume element in the electrode during the change of Li concentration if the whole element is subject to no stresses. For a well-primed a-Si electrode, the stress-free deformation during Li concentration change is isotropic with only volumetric changes.

For the first lithiation half-cycle of a c-Si electrode, however, the stress-free deformation can be anisotropic [57, 59, 69]. This anisotropic expansion can lead to undesirable effect of stress intensification and fracture at certain locations [69]. For electrodes made of a-Si, the first lithiation half-cycle is also a two-phase process but without expansion anisotropy [59]. This difference in expansion behaviors implies that a-Si undergoes more manageable physical transformations than c-Si during the first priming cycle, which may make it a more desirable active material [59]. After the first priming cycle, however, both c-Si and a-Si are fully amorphized and further lithiation-delithiation cycles only induce isotropic expansions. As discussed in section 2.1.1, this research mainly focuses on situations in which the starting material is fully amorphous, such that the governing kinetics is diffusion instead of phase transition, and the stress-free expansion can be assumed to be isotropic.

2.1.3. Plastic deformation and lithiation-induced softening

Sethuraman et al. employed an experimental technique with a multi-beam optical sensor (MOS) to measure the in-situ stress evolution in a thin-film Si electrode [72]. The technique entails the measurement of the curvature change of the film-substrate system during electrochemical cycling and the calculation of the stresses in the thin film from the curvature via the Stoney equation [73, 74]. Fig. 2.1 shows the cell potential and the film stress so obtained as functions of the capacity of the silicon thin-film electrode [15]. This capacity level (the horizontal axis) is linearly related to the Li content ξ in the chemical composition $Li_\xi Si$. During the lithiation process, an initial linear increase in the bi-axial compressive stress is attributed to elastic deformation. At compressive stress of about 1.7 GPa (which corresponds to a capacity of *ca.* 325 mAhg^{-1}), the film appears to reach the elastic limit and begins deform inelastically with further lithiation. This response is needed in order to accommodate the additional volume expansion. The flow stress is seen to decrease with further lithiation, reaching a value of about 1 GPa at a capacity of *ca*. 1875 mAhg^{-1}, at the cut-off potential. Upon delithiation, the unloading is initially elastic; the stress reverses elastically until it reaches *ca.* 1 GPa in tension, where the film begins to flow in tension in order to accommodate the reduction in volume. The flow stress increases to about 1.75 GPa when the upper limit of 1.2 V is reached. What Sethuraman et al. [15] observed clearly indicates that lithiated Si undergoes inelastic deformation, and the associated yield stress σ_Y decreases as the Li content ξ in $Li_{\xi}Si$ increases. Such a decrease in σ_Y is an important manifestation of what is called lithiation-induced softening.

In terms of the atomistic mechanisms that underlie the observed behavior, Zhao et al. [75] proposed that the brittle-to-ductile transition with increasing Li concentration and associated large plastic deformation is due to continuous lithium-assisted breaking and re-forming of Si-Si bonds and the creation of nanopores.

Besides the decrease in σ_Y, the effect on mechanical properties of Li/Si of lithiation also entails the decrease in elastic moduli [72, 76, 77]. One of the earliest studies on the elastic softening of Li-Si due to lithiation was by Shenoy et al. [77], who carried out density functional theory (DFT) calculations of the elastic moduli of a-Si and c-Si in different lithiation states. They found that the elastic properties of a-Si and c-Si depend strongly on the lithiation state, i.e. the ξ value in the chemical formula $Li_{\xi}Si$. This dependence approximately follows the rule of mixing that connects the elastic properties of $Li_\xi Si$ at the two end compositions, i.e. $\xi=0$ and $\xi=\xi_{max}$. In terms of atomistic mechanism, they attributed the elastic softening to the increase in the population of ionic Li–Si bonds that are weaker than the covalent Si–Si bonds [77].

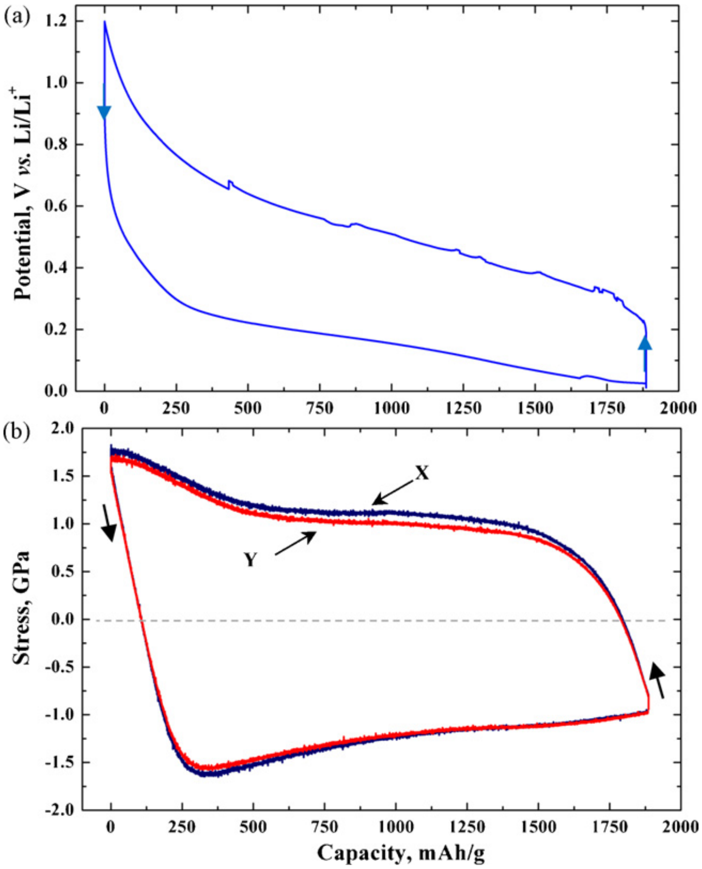

Fig. 2.1 Cell potential vs. capacity curve corresponding to lithiation and delithiation of a-Si thin-film electrode cycled at C/4 rate between 1.2 and 0.01 V vs. Li/Li^+, and (b) the corresponding stress calculated from the substrate curvature using the Stoney equation. The curves labeled X and Y correspond to the stresses calculated from the averaged horizontal and vertical displacements of the spots, respectively. The arrows in both figures indicate cycling direction. Reproduced from Ref. [15].

Hertzberg et al. [76] arrived at a conclusion consistent with those drawn by Sethuraman et al. [15] and Shenoy et al. [77] for the Young's modulus and hardness through ex-situ depth-sensing indentation experiments. The measurements by Hertzberg et al. [76] indicate that the Young's modulus decreases from an initial value of 92 GPa for pure Si to 12 GPa at full lithium insertion (Li_5Si_4), and the corresponding hardness change is from an initial value of 5 GPa for Si to 1.5 GPa for $Li_{15}Si_4$. The measured modulus-concentration dependence by Hertzberg et al. deviates slightly from the simple rule of mixing suggested by the DFT calculations of Shenoy et al. [77]. Such a deviation could have important implications, but is nevertheless considered to be as higher-order effect in most continuum models that consider the lithiation-induced softening (e.g. [16, 40, 43]).

In continuum theories, the lithiation-induced changes in mechanical properties are usually modeled by assuming that the elastic moduli and yield stress are functions of the local lithium concentration [16, 39, 40], an assumption that is sufficient for capturing most experimental observations with regard to the effects of lithiation-induced softening. More sophisticated theories have also been proposed [41, 42]. In this study, we assume that the elastic moduli and yield stress are functions of the local lithium concentration via the rule of mixing.

2.1.4. Interdiffusion of lithium and host atoms

Most existing continuum models of Li-ion battery electrode materials are based on the assumption that host atoms are immobile. Nevertheless, DFT calculations by Kim et al. [78] show that the bonding environment of silicon atoms changes significantly as lithium concentration increases, indicating that the diffusive migration of silicon may become non-negligible. Recently, Johari et al. [79] calculated the diffusivity of both Li and Si (D^{Li} and D^{Si}) in crystalline and amorphous Si (c-Si and a-Si) electrodes using ab initio molecular dynamics.

They found that $D^{Li} = 1.67\times10^{-10} \sim 4.88\times10^{-9}$ cm^{2}s^{-1} and $D^{Si} = 1.97\times10^{-14} \sim 5.74\times10^{-13}$ cm^{2}s^{-1} for c-Si and $D^{Li} = 1.25\times10^{-9} \sim 3.69\times10^{-8}$ cm^{2}s^{-1} and $D^{Si} = 1.53\times10^{-11} \sim 5.13\times10^{-10}$ cm^{2}s^{-1} for a-Si. The associated diffusivity ratio in a-Si falls into the range of $D^{Si} / D^{Li} = 0.8\times10^{-2} \sim 1.39\times10^{-2}$. It should be noted that the study by Johari et al. was conducted on Li/Si systems with the composition of Li$_{1.0}$Si. For higher Li contents, the diffusivity ratio D^{Si} / D^{Li} could be even higher since more Si-Si covalent bonds are broken. In Li/Ge, another promising alloy-based electrode material, host diffusion could be even more significant since the Ge-Ge covalent bond is much weaker than the Si-Si bond (the melting temperatures of crystalline Si and Ge are 1687 K and 1211.40 K, respectively).

Finite diffusivity values of host atoms may have interesting implications on the performance and cyclability of alloy-based electrode materials. For example, in Li/Si and Li/Ge nano-electrodes, cycling-induced formation of nano-pores indicates that the host material has been irreversibly moved away from the voided regions [5, 80]. If reversible expansion and elastic deformation were the only mechanisms for material deformation, the nano-pores would not form because the host network must revert back to its original configuration upon unloading. Two mechanisms have been proposed to account for the irreversible migration of host atoms. The first is inelastic flow (a form of continuous convection) driven by deviatoric stresses during which material flows in the normal direction of the nucleated pore, leading to void enlargement [5]. The second mechanism is vacancy aggregation during selective dealloying, which involves diffusive migration of host atoms and allows nucleated voids to coalesce and grow [80]. Either or both mechanisms might be relevant, their relative significance depends on the specific material system.

The continuum framework in this study takes the effect of non-zero host diffusivity into consideration. As will be discussed in section 4.3, the finite diffusivity of host can also bring up a stress relaxation mechanism even at stress levels below the yield threshold. For other parts of this study, the assumption of immobile host lattice will be taken in order to simplify the model and allow more focused discussions.

2.1.5. Effect of stress on Li chemical potential

While the mass diffusion of lithium, a chemical process, induces volume changes and stresses, the stresses also affect the chemical process. Specifically, since the lithium chemical potential increases when the material is under compressive stresses and *vice versa* when the material is under tensile stresses, the mechanical stresses can take effect on the diffusive transport of lithium. The question is how much change in chemical potential can be induced by this mechanical-to-chemical coupling. Sheldon et al. measured the stress contributions to solution thermodynamics in Li/Si alloys, and found that the stresses can alter the electrochemical potential by 50 mV or more [81]. On the capacity-voltage curve, this stress-induced chemical potential shift can be responsible for 40% of the energy loss, i.e. of the area enclosed by the hysteresis [15, 72, 82, 83].

It turns out that the chemical potential shift induced by stresses, although only about 50 mV, is big enough to significantly affect the diffusive transport in Li/Si [43], as will be discussed in section 4.1. Section 2.2 therefore takes the two-way coupling between deformation and diffusion as an essential part of the theoretical framework.

2.2. Theory of diffusion-deformation coupling

The lithiation and delithiation of alloy-based electrodes are electrochemical processes. Still, the electric conductivities of most alloy-based electrodes are high enough so that the electric potential inside the solid domain of the electrode particles can be regarded as uniform. Therefore, most particle-level continuum models of electrode materials entail only the coupling between Li diffusion and mechanical deformation, but not electric fields [16, 18, 40, 45], although exceptions exist [16]. In this study, sufficient electric conductance is assumed so that the whole electrode has a uniform electric potential, and only the deformation and diffusion processes need to be analyzed explicitly.

The electrode is assumed to be composed of two chemical species: host (denoted as H) and guest (lithium). Vacancies are not treated as chemical species due to the lack of site-conservation constraint in amorphous materials [84].

Based on the background information in section 2.1, in establishing the continuum framework for diffusion-deformation coupling in alloy-based electrodes, it is desirable to capture the following:

1) The geometric non-linearity due to deformation up to 300% volume expansion,
2) The material non-linearity due to incremental inelastic flow,
3) Small but finite host diffusivity,
4) The two-way deformation-diffusion coupling, especially the effect of stresses on diffusion,
5) The phase transformation during the first lithiation cycle, and

6) The anisotropic stress-free expansion during first lithiation cycle.

Because this study focuses on well-primed a-Si electrodes, we focus on (1)-(4) but not on (5) and (6). Nevertheless, internal state variables are considered in the thermodynamics and arbitrary stress-free deformation is used in the kinematics, so that (5) and (6) can be captured with minor extension of the framework.

2.2.1. Kinematics

Since the material of interest is highly amorphous with small but non-zero host diffusivity [79], the notion of continuous deformation must be used with caution. Following the treatment by Stephenson [84], we identify two types of host atom movement during guest (lithium) insertion: collective convection and diffusive transport. To illustrate the relative displacement between neighboring host atoms, network lines (solid black) linking adjacent hosts are introduced in Fig. 2.2. It should be noted that these lines do not necessarily represent host-host bonds, although recent studies do indicate that a significant portion of Si atoms tend to remain in rings, chains or pairs even in highly lithiated amorphous Li/Si [78]. It should also be noted that the regular arrangement of the initial network [Fig. 2.2 (a)] is used only to facilitate the illustration without implying any regularity or periodicity in atomic structure. As the material expands due to guest insertion, two scenarios may arise in terms of the movement of the host atoms. In the first scenario (consider atom B as the example), the network lines linking the host atom (B) with its neighbors (B-C, B-D, B-E) remain; and the movement of the host (B) can be tracked by bookkeeping the continuum deformation $\mathbf{x}=\mathbf{x}(\mathbf{X},t)$ of the network. We call this type of host movement collective convection. In the second scenario (consider atom A as the example), the local distortion of the network is so significant that the atom’s nearest neighbors completely change. The displacement of atom A can be decomposed into two parts: the first part is from the initial position of A to an imaginary point A′ and is due to collective convection; the second part is from A′ to the final position of A. The second part of displacement (from A′ to the final position) is highly random compared with the collective convection, and the effect is the diffusive transport of the host atom relative to the collectively deformed configuration. Here, the position of A′ can be obtained by averaging the positions of atoms within a representative volume element (RVE) around A [A, C, D, F and G in Fig. 2.2 (a)]. The deformed network so obtained (to which A′ is attached) reflects the structural deformation of the material and defines the updated Lagrangian configuration.

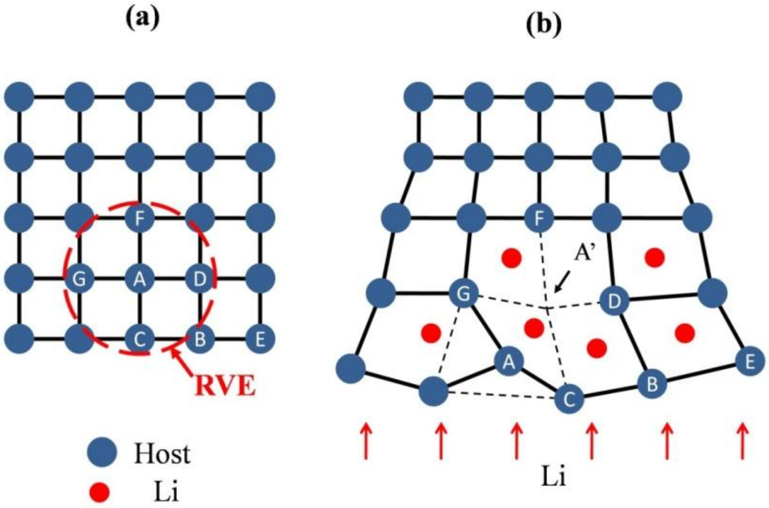

Fig. 2.2 The distinction between collective convection and diffusive transport. (a) The original host network. The solid black lines represent the network lines linking each host atoms to its neighboring hosts. These network lines do not necessarily represent host-host bonds. (b) When guest atoms (Li here) are inserted, the host network is distorted and some host atoms (e.g. atom A) may migrate relative the network. The dashed lines in (b) gives the host network site A′ which is given by averaging the movement of atoms (i.e. A, C, D, F and G) in a RVE around A.

If the diffusive transport dominates the host atom movement, the arrangement of the hosts is reshuffled quickly (too many host atoms move like A) and a continuum mapping $\mathbf{x}=\mathbf{x}\left(\mathbf{X},t\right)$ between the reference and current configurations may not be well-defined. Here, we assume that the diffusivity of the hosts is much smaller than that of the guests (Li) so that the host network can be identified and, consequently, the continuous deformation $\mathbf{x}=\mathbf{x}\left(\mathbf{X},t\right)$ is well-defined. Note that $\mathbf{x}=\mathbf{x}\left(\mathbf{X},t\right)$ should be construed in an average sense which may involve statistically averaging the displacement of atoms in a specific RVE [c.f. Fig. 2.2].

The Eulerian concentrations of the host (e.g., Si) and the guest (lithium), namely the atomic numbers per unit current volume, are denoted by c^H and c^{Li}, respectively. Their Lagrangian counterparts C^H and C^{Li} in the reference configuration are related to c^H and c^{Li} by $C^H=\det\left(\mathbf{F}\right)c^H$ and $C^{Li}=\det\left(\mathbf{F}\right)c^{Li}$, where $\mathbf{F}=\partial\mathbf{x}/\partial\mathbf{X}$ is the deformation gradient. The dimensionless compositions $x^H\equiv c^H/\left(c^{Li}+c^H\right)$, $x^{Li}\equiv c^{Li}/\left(c^{Li}+c^H\right)$ and $\xi\equiv c^{Li}/c^H$, on the other hand, can be used to measure the proportions of the concentrations of the host and the guest. Here, composition ξ corresponds to the lithium number per host in the chemical formula $\mathrm{Li}_\xi\mathrm{H}$. The maximum ξ at the fully charged state is denoted as $\xi_{\max}$, and the state of charge (SOC) relative to this fully charged state is denoted as $\Xi\equiv\xi/\xi_{\max}$.

Following the standard theory of large deformation plasticity, a Lee-type decomposition [16, 85] can be performed for the deformation gradient, i.e.,

$$\mathbf{F}=\mathbf{F}^e\cdot\mathbf{F}^{SF}\cdot\mathbf{F}^p \tag{2-1}$$

where $\mathbf{F}^e$, $\mathbf{F}^{SF}$ and $\mathbf{F}^p$ are the elastic, stress-free volumetric and plastic deformation gradients, respectively [16, 40]. Here, the plastic part $\mathbf{F}^p$ is volume-conserving [i.e., $\det\left(\mathbf{F}^p\right)=1$], and the volumetric part $\mathbf{F}^{SF}$ is termed "stress-free" because it corresponds to the shape changes of the material due to composition change without stress. One assumption that is typically made for amorphous silicon (a-Si) is that $\mathbf{F}^{SF}$ is isotropic, although the theoretical framework depicted by Eq. (2-1) by itself does require such isotropy and can also be used for situations where $\mathbf{F}^{SF}$ is anisotropic (cf. section 2.1.2).

The decomposition in Eq. (2-1) implies linking the reference (or Lagrangian) state and the current (or Eulerian) state via two imaginary and incompatible states, as shown in Fig. 2.3. When a piece of electrode material is lithiated from the top layer, the top part expands in the actual charged state, leading to deformation gradient $\mathbf{F}$ and associated stresses. This total deformation gradient is decomposed such that the material first deforms plastically to reach incompatible state I, and then undergoes expansion $\mathbf{F}^{SF}$ to reach incompatible state II. Here incompatible states I and II are stress-free but discontinuous. To maintain continuity, an elastic accommodation $\mathbf{F}^e$ is needed. This elastic deformation pieces the incompatible state II together back to the actual charged and stressed state.

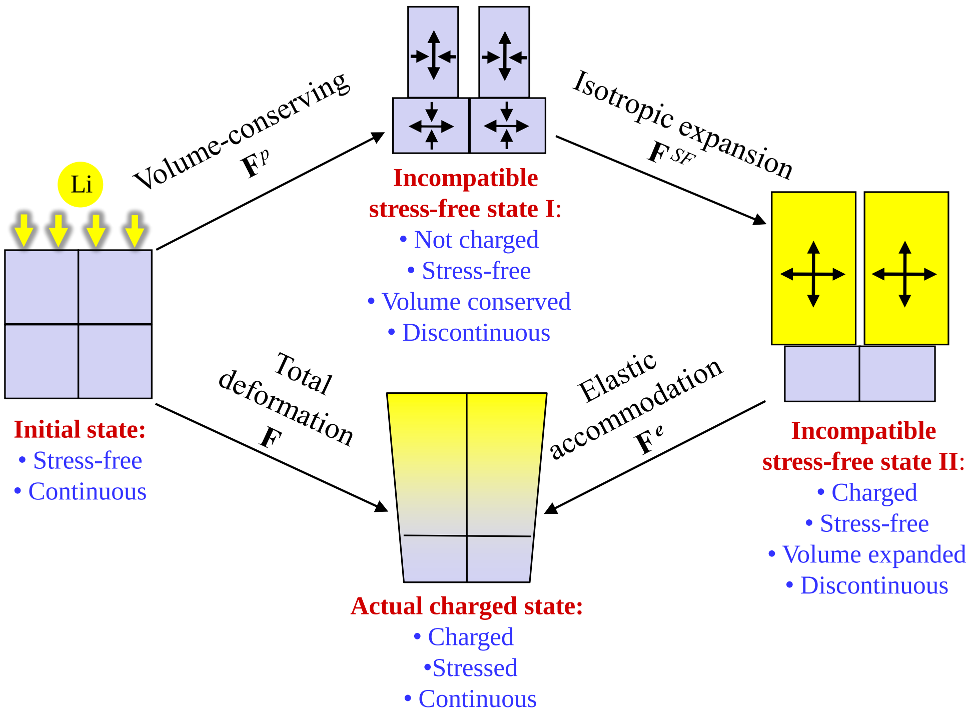

Fig. 2.3 Illustration of the Lee-type decomposition. The total deformation gradient $\mathbf{F}$ *is decomposed into three parts linked by two incompatible stress-free states.*

Given the Lee decomposition delineated in Eq. (2-1) and Fig. 2.3, the mechanical properties of an electrode material can be prescribed by laying out the constitutive equations that govern $\mathbf{F}^e$, $\mathbf{F}^{SF}$ and $\mathbf{F}^p$ one by one. In order to account for incremental large deformations, this is done via the associated rates of deformation

$$\left.\begin{aligned}
&\mathbf{D}^{e} \equiv \left[\dot{\mathbf{F}}^{e}\left(\mathbf{F}^{e}\right)^{-1}\right]_{sym},\\
&\mathbf{D}^{SF} \equiv \left[\mathbf{F}^{e}\cdot\dot{\mathbf{F}}^{SF}\cdot\left(\mathbf{F}^{SF}\right)^{-1}\cdot\left(\mathbf{F}^{e}\right)^{-1}\right]_{sym},\\
&\mathbf{D}^{p} \equiv \left[\mathbf{F}^{e}\cdot\mathbf{F}^{SF}\cdot\dot{\mathbf{F}}^{p}\cdot\left(\mathbf{F}^{p}\right)^{-1}\cdot\left(\mathbf{F}^{SF}\right)^{-1}\cdot\left(\mathbf{F}^{e}\right)^{-1}\right]_{sym},\ \text{and}\\
&\mathbf{D} = \left[\dot{\mathbf{F}}\left(\mathbf{F}\right)^{-1}\right]_{sym} = \mathbf{D}^{e}+\mathbf{D}^{SF}+\mathbf{D}^{p}.
\end{aligned}\right\} \tag{2-2}$$

2.2.2. Conservation of mass and momentum

The diffusive fluxes of lithium and host can be measured either in the Lagrangian frame as $\mathbf{J}^{Li}$ and $\mathbf{J}^{H}$ or in the updated Lagrangian frame as $\mathbf{j}^{Li}$ and $\mathbf{j}^{H}$. These quantities are related through $\mathbf{f} \equiv \mathbf{F}^{-1}$ as:

$$J_K^S = \det\left(\mathbf{F}\right) f_{Ki} j_i^S, \quad \left(S = Li, H\right). \tag{2-3}$$

The associated equation for mass conservation in the Lagrangian frame is

$$\frac{\partial C^S}{\partial t} + \frac{\partial J_K^S}{\partial X_K} = R_b^S, \quad \left(S = Li, H\right), \tag{2-4}$$

where R_b^S is the body source of species S (=Li, H) measured in the Lagrangian frame.

It is important to notice that $\mathbf{j}^{Li}$ and $\mathbf{j}^{H}$ are measured in the updated Lagrangian frame relative to the moving host network which undergoes convection $\mathbf{x} = \mathbf{x}\left(\mathbf{X}, t\right)$, instead of in the Eulerian frame. If the fluxes were to be measured relative to the Eulerian frame, the conservation of mass would take the form of a mixed convection-diffusion equation in order to avoid double counting the movement of Li and H [84]. That approach is not used here. Again, vacancies should not be treated as chemical species here due to the lack of site-conservation constraint in amorphous materials, as discussed by Stephenson [84].

Finally, under the conditions of zero body force and negligible inertia effect, balance of momentum takes the form

$$\frac{\partial \sigma_{ji}}{\partial x_j} = 0, \tag{2-5}$$

where σ_{ij} is the mechanical Cauchy stress. Contributions due to the electromagnetic Maxwell stress is neglected since its magnitude is much smaller than the contribution due to σ_{ij} in typical battery electrode applications [16].

2.2.3. Thermodynamics

The thermodynamic properties of the electrode material can be characterized by the Lagrangian density of the Helmholtz free energy ϕ [54]. We assume

$$\phi = \phi(\mathbf{F}^e, C^H, C^{Li}, \theta, \alpha), \tag{2-6}$$

where θ is the temperature and α is an internal state variable (also known as the order parameter) describing the non-equilibrium metastable states. Physically, α can be the degree of amorphization [55, 86], porosity [14], or degree of damage. Consider an infinitesimal virtual deformation $\delta\mathbf{x}$ during which C^H, C^{Li}, θ, and α are kept constant. The virtual work done by the external agent is related to the 1st Piola-Kirchhoff stress $\sigma_{Kj}^{PK1} = \det(\mathbf{F}) f_{Ki}\sigma_{ij}$ through

$$\delta W_{mech} = \int_{V_0} \sigma_{Kj}^{PK1} \frac{\partial \delta x_j}{\partial X_K} dV_0, \tag{2-7}$$

where $\int_{V_0} (\bullet) dV_0$ stands for integration over the Lagrangian volume. On the other hand,

$$\begin{aligned} \delta W_{mech} = \delta\phi &= \int_{V_0} \left[\phi\left(\mathbf{F}^e + \frac{\partial \delta\mathbf{x}}{\partial \mathbf{x}} \cdot \mathbf{F}^e, C^H, C^{Li}, \theta, \alpha \right) - \phi\left(\mathbf{F}^e, C^H, C^{Li}, \theta, \alpha \right) \right] dV_0 \\ &= \int_{V_0} \left[\left. \frac{\partial \phi}{\partial F_{jk}^e} \right|_{C^H, C^{Li}, \theta, \alpha} \frac{\partial \delta x_j}{\partial x_l} F_{lk}^e \right] dV_0 = \int_{V_0} \left[\left. \frac{\partial \phi}{\partial F_{jk}^e} \right|_{C^H, C^{Li}, \theta, \alpha} \frac{\partial \delta x_j}{\partial X_K} f_{Kk}^* \right] dV_0. \end{aligned} \tag{2-8}$$

Here, $\mathbf{f}^{SF} \equiv \left(\mathbf{F}^{SF}\right)^{-1}$, $\mathbf{f}^P \equiv \left(\mathbf{F}^P\right)^{-1}$ and $\mathbf{f}^* \equiv \mathbf{f}^P \cdot \mathbf{f}^{SF}$. A comparison of (2-7) and (2-8) leads to

$$\sigma_{Kj}^{PK1} = \left. \frac{\partial \phi}{\partial F_{jk}^e} \right|_{C^H, C^{Li}, \theta, \alpha} f_{Kk}^* \tag{2-9}$$

and

$$\sigma_{ij} = \frac{1}{\det\left(\boldsymbol{F}\right)} F_{iK} \sigma_{Kj}^{PK1} = \frac{1}{\det\left(\boldsymbol{F}\right)} F_{ik}^e \left. \frac{\partial \phi}{\partial F_{jk}^e} \right|_{C^H, C^{Li}, \theta, \alpha}. \tag{2-10}$$

Following Wu [54], the chemical potential of lithium is given by

$$\mu^{Li} = \left.\frac{\partial \phi}{\partial C^{Li}}\right|_{\mathbf{F},C^{H},\theta,\alpha,\mathbf{F}^{P}} = \left.\frac{\partial \phi}{\partial F^{e}_{ij}}\right|_{C^{H},C^{Li},\theta,\alpha} \left.\frac{\partial F^{e}_{ij}}{\partial C^{Li}}\right|_{\mathbf{F},C^{H},\theta,\alpha,\mathbf{F}^{P}} + \left.\frac{\partial \phi}{\partial C^{Li}}\right|_{\mathbf{F}^{e},C^{H},\theta,\alpha} . \tag{2-11}$$

Since $\frac{\partial \mathbf{f}^{SF}}{\partial C^{Li}} = -\mathbf{f}^{SF} \frac{\partial \mathbf{F}^{SF}}{\partial C^{Li}} \mathbf{f}^{SF}$,

$$\left.\frac{\partial \mathbf{F}^{e}}{\partial C^{Li}}\right|_{\mathbf{F},C^{H},\theta,\alpha,\mathbf{F}^{P}} = \left.\frac{\partial\left(\mathbf{F}\cdot\mathbf{f}^{p}\cdot\mathbf{f}^{SF}\right)}{\partial C^{B}}\right|_{\mathbf{F},C^{H},\theta,\alpha,\mathbf{F}^{P}} = -\mathbf{F}^{e}\cdot\left.\frac{\partial \mathbf{F}^{SF}}{\partial C^{B}}\right|_{\mathbf{F},C^{H},\theta,\alpha,\mathbf{F}^{P}} \cdot\mathbf{f}^{SF}. \tag{2-12}$$

Substitution of eq. (2-12) into eq. (2-11) leads to

$$\mu^{Li} = \left.\frac{\partial \phi}{\partial C^{Li}}\right|_{\mathbf{F}^{e},C^{H},\theta,\alpha} - \left.\frac{\partial \phi}{\partial F^{e}_{ij}}\right|_{C^{H},C^{Li},\theta,\alpha} F^{e}_{ik} \left.\frac{\partial F^{SF}_{kl}}{\partial C^{Li}}\right|_{\mathbf{F},C^{H},\theta,\alpha,\mathbf{F}^{P}} f^{SF}_{lj} . \tag{2-13}$$

With Eqs. (2-10) and (2-13), the guest (lithium) chemical potential can be related to the Cauchy stress by

$$\mu^{Li} = \left.\frac{\partial \phi}{\partial C^{Li}}\right|_{\mathbf{F}^{e},C^{H},\theta,\alpha} - \det\left(\boldsymbol{F}\right) f^{e}_{mi}\sigma_{ij}F^{e}_{jk} \left.\frac{\partial F^{SF}_{kl}}{\partial C^{Li}}\right|_{\mathbf{F},C^{H},\theta,\alpha,\mathbf{F}^{P}} f^{SF}_{lm} . \tag{2-14}$$

By the same token, the chemical potential of the host atoms can be written as

$$\mu^{H} = \left.\frac{\partial \phi}{\partial C^{H}}\right|_{\mathbf{F}^{e},C^{Li},\theta,\alpha} - \det\left(\boldsymbol{F}\right) f^{e}_{mi}\sigma_{ij}F^{e}_{jk} \left.\frac{\partial F^{SF}_{kl}}{\partial C^{H}}\right|_{\mathbf{F},C^{Li},\theta,\alpha,\mathbf{F}^{P}} f^{SF}_{lm} . \tag{2-15}$$

2.2.4. Kinetics

According to Wu [54], the Clausius-Duhem inequality can be stated in the Lagrangian frame as

$$\begin{aligned}&-\left[\dot{\phi}+\eta\dot{\theta}-\boldsymbol{\sigma}^{PK1}_{Ki}\dot{F}_{iK}-\mu^{H}\dot{C}^{H}-\mu^{Li}\dot{C}^{Li}\right]\\&+\theta\mathbf{J}^{(q)}\cdot\nabla_{\boldsymbol{X}}\left(\frac{1}{\theta}\right)+\theta\boldsymbol{J}^{H}\cdot\nabla_{\boldsymbol{X}}\left(-\frac{\mu^{H}}{\theta}\right)+\theta\mathbf{J}^{Li}\cdot\nabla_{\boldsymbol{X}}\left(-\frac{\mu^{Li}}{\theta}\right)\geq 0,\end{aligned}\tag{2-16}$$

where $\mathbf{J}^{(q)}$ is the heat flux measured in the Lagrangian frame and η is the Lagrangian density of entropy. Under isothermal conditions with $\dot{\theta}=0$ and $\nabla_{\boldsymbol{X}}\theta=\mathbf{0}$,

$$-\left[\dot{\phi}-\boldsymbol{\sigma}^{PK1}_{Ki}\dot{F}_{iK}-\mu^{H}\dot{C}^{H}-\mu^{Li}\dot{C}^{Li}\right]+\theta\mathbf{J}^{H}\cdot\nabla_{\boldsymbol{X}}\left(-\frac{\mu^{H}}{\theta}\right)+\theta\mathbf{J}^{Li}\cdot\nabla_{\boldsymbol{X}}\left(-\frac{\mu^{Li}}{\theta}\right)\geq 0.\tag{2-17}$$

On the other hand, because $\dot{\theta}=0$,

$$\dot{\phi}=\left.\frac{\partial\phi}{\partial F^{e}_{ij}}\right|_{C^{H},C^{Li},\theta,\alpha}\dot{F}^{e}_{ij}+\left.\frac{\partial\phi}{\partial C^{H}}\right|_{\mathbf{F}^{e},C^{Li},\theta,\alpha}\dot{C}^{H}+\left.\frac{\partial\phi}{\partial C^{Li}}\right|_{\mathbf{F}^{e},C^{H},\theta,\alpha}\dot{C}^{Li}+\left.\frac{\partial\phi}{\partial\alpha}\right|_{\mathbf{F}^{e},C^{H},C^{Li},\theta}\dot{\alpha}.\tag{2-18}$$

Since $\boldsymbol{\sigma}^{PK1}_{Ki}\dot{F}_{iK}=\det\left(\mathbf{F}\right)\sigma_{ij}D_{ji}$, Eqs. (2-18), (2-14), (2-15), (2-10) and (2-2) lead to

$$\begin{aligned}&\dot{\phi}-\boldsymbol{\sigma}^{PK1}_{Ki}\dot{F}_{iK}-\mu^{H}\dot{C}^{H}-\mu^{Li}\dot{C}^{Li}\\&=\det\left(\mathbf{F}\right)f^{e}_{mi}\sigma_{ij}F^{e}_{jk}f^{SF}_{lm}\left[\left.\frac{\partial F^{SF}_{kl}}{\partial C^{Li}}\right|_{\mathbf{F},C^{H},\theta,\alpha,\mathbf{F}^{P}}\dot{C}^{Li}+\left.\frac{\partial F^{SF}_{kl}}{\partial C^{H}}\right|_{\mathbf{F},C^{Li},\theta,\alpha,\mathbf{F}^{P}}\dot{C}^{H}\right]\\&+\left.\frac{\partial\phi}{\partial\alpha}\right|_{\mathbf{F}^{e},C^{H},C^{Li},\theta}\dot{\alpha}-\det\left(\mathbf{F}\right)\sigma_{ij}D^{SF}_{ji}-\det\left(\mathbf{F}\right)\sigma_{ij}D^{P}_{ji}\end{aligned}\tag{2-19}$$

The isothermal Clausius-Duhem inequality in the updated Lagrangian frame therefore takes the form

$$\gamma_P + \gamma_\alpha + \mathbf{j}^{Li} \cdot \nabla_{\boldsymbol{x}} \left(-\mu^{Li} \right) + \mathbf{j}^{H} \cdot \nabla_{\boldsymbol{x}} \left(-\mu^{H} \right) \geq 0, \tag{2-20}$$

where the plastic dissipation rate γ_P and the local dissipation rate γ_α are defined as

$$\begin{cases} \gamma_P \equiv \sigma_{ij} D_{ji}^{P}, \\ \gamma_\alpha \equiv \sigma_{ij} D_{ji}^{SF} - f_{mi}^{e} \sigma_{ij} F_{jk}^{e} f_{lm}^{SF} \left[\left. \dfrac{\partial F_{kl}^{SF}}{\partial C^{Li}} \right|_{\mathbf{F}, C^H, \theta, \alpha, \mathbf{F}^P} \dot{C}^{Li} + \left. \dfrac{\partial F_{kl}^{SF}}{\partial C^{H}} \right|_{\mathbf{F}, C^{Li}, \theta, \alpha, \mathbf{F}^P} \dot{C}^{H} \right] \\ \qquad - \dfrac{1}{\det\left(\boldsymbol{F} \right)} \left. \dfrac{\partial \phi}{\partial \alpha} \right|_{\mathbf{F}^e, C^H, C^{Li}, \theta} \dot{\alpha}. \end{cases} \tag{2-21}$$

In general, the stress-free deformation $\mathbf{F}^{SF}$ can be a function of C^{Li}, C^{H} and the internal state variable α, i.e.,

$$\mathbf{F}^{SF} = \mathbf{F}^{SF} \left(C^{H}, C^{Li}, \alpha \right) . \tag{2-22}$$

By Eq. (2-2),

$$\sigma_{ij} D_{ji}^{SF} = \sigma_{ij} F_{jk}^{e} \dot{F}_{kl}^{SF} f_{lm}^{SF} f_{mi}^{e}. \tag{2-23}$$

Therefore, Eqs. (2-21)-(2-23) combine to give

$$\begin{cases} \gamma_\alpha = f_\alpha \dot{\alpha}, \\ f_\alpha \equiv f^e_{mi} \sigma_{ij} F^e_{jk} f^{SF}_{lm} \left. \dfrac{\partial F^{SF}_{kl}}{\partial \alpha} \right|_{\mathbf{F}, C^H, C^{Li}, \theta, \mathbf{F}^P} - \dfrac{1}{\det(\boldsymbol{F})} \dfrac{\partial \phi}{\partial \alpha}. \end{cases} \tag{2-24}$$

The kinetic driving force can be defined as

$$\mathbf{X}_{kin} \equiv \left[\boldsymbol{\sigma},\, f_\alpha, \nabla_{\boldsymbol{x}} \left(-\mu^{Li} \right), \nabla_{\boldsymbol{x}} \left(-\mu^H \right) \right]^T \tag{2-25}$$

and the associated response is

$$\mathbf{J}_{kin} \equiv \left[\mathbf{D}^P, \dot{\alpha}, \mathbf{j}^{Li}, \mathbf{j}^H \right]^T = \mathbf{J}_{kin} \left(\mathbf{X}_{kin} \right). \tag{2-26}$$

The kinetic response of the electrode material is specified through the driving force-response relation $\mathbf{J}_{kin} = \mathbf{J}_{kin} \left(\mathbf{X}_{kin} \right)$ which must satisfy the Clausius-Duhem inequality in the form of

$$\mathbf{J}_{kin}{}^T \cdot \mathbf{X}_{kin} \geq 0. \tag{2-27}$$

In this study, the simplest linear “diagonal” form is chosen for Eq. (2-26) such that

$$\begin{cases} \mathbf{D}^P = \dot{\lambda} \dfrac{\partial Q}{\partial \boldsymbol{\sigma}}, \\ \dot{\alpha} = c_\alpha f_\alpha, \\ j^{Li}_i = -\dfrac{D^{Li}_{ik}}{k_B \theta} c^{Li} \dfrac{\partial \mu^{Li}}{\partial x_k}, \text{ and} \\ j^H_i = -\dfrac{D^H_{ik}}{k_B \theta} c^H \dfrac{\partial \mu^H}{\partial x_k}. \end{cases} \tag{2-28}$$

In the above relations, D_{ik}^{Li} and D_{ik}^{Li} are the positive-definite tensorial diffusivity of lithium and host, respectively; c_α is the linear coefficient for internal state variable evolution; k_B is the Boltzmann constant; $Q = Q(\boldsymbol{\sigma})$ is the dissipation potential for plastic flow; and $\dot{\lambda}$ is the scalar rate coefficient for plasticity. For visco-plastic materials, $\dot{\lambda} = \dot{\lambda}(\boldsymbol{\sigma})$; for rate-independent materials, $\dot{\lambda}$ can be determined through the consistency condition.

It is often convenient to evaluate the fluxes in the Lagrangian frame. When the diffusivities are isotropic [see Eqn. (2-33)], the Lagrnangian fluxes can be obtained from the fluxes in the updated Lagrangian frame in Eqn. (2-28) through

$$\begin{cases} J_K^{Li} = -\dfrac{D^{Li}}{k_B\theta} f_{Ki} f_{Ji} C^{Li} \dfrac{\partial \mu^{Li}}{\partial X_J}, \text{ and} \\ J_K^{H} = -\dfrac{D^{H}}{k_B\theta} f_{Ki} f_{Ji} C^{H} \dfrac{\partial \mu^{H}}{\partial X_J}. \end{cases} \tag{2-29}$$

2.2.5. Constitutive behaviors of fully amorphized isotropic electrode materials

Equations (2-6), (2-10), (2-14), (2-15), (2-25) and (2-26) provide a general framework for two-species electrode materials that undergo large elastic-plastic deformations. The formulation is capable of capturing anisotropic behavior through anisotropic $\mathbf{F}^{SF}$ and the effects of phase transformations through the internal state variable α. To proceed, material-specific relationships [Eqs. (2-6), (2-22) and (2-26)] need to be specified. Since the electrode material of interest here is fully primed amorphized Li-alloys, several further assumptions are in order.

Full amorphization

The theoretical framework in this study is capable of phenomenologically capturing the amorphization process in the first few charging cycles via a double-well potential of ϕ in terms of α [cf. Eq. (2-6)]. Such a phase field model of amorphization is not considered here, mainly due to the lack of experimental data on the evolution law of α. Instead, the alloy is assumed to have fully amorphized, with saturated degree of amorphization, i.e. $\dot{\alpha} = 0$. This assumption is reasonable because full amorphization is achieved after only a few charge-discharge cycles for an initially crystalline Si electrode. The isothermal free energy thus becomes

$$\phi = \phi(\mathbf{F}^e, C^H, C^{Li}). \tag{2-30}$$

Small elastic deformation

The elastic deformation is assumed to be small compared with the total deformation and can be characterized by the elastic strain

$$\boldsymbol{\varepsilon}^e \equiv \frac{1}{2}\left(\left(\mathbf{F}^e\right)^T\left(\mathbf{F}^e\right) - \mathbf{I}\right). \tag{2-31}$$

The free energy ϕ can therefore be written as the sum of a stress-free (SF) part ϕ^{SF} and an elastic part w [54], i.e.,

$$\begin{cases} \phi = \phi(\mathbf{F}^e, C^H, C^{Li}, \theta) = \phi^{SF}(C^H, C^{Li}, \theta) + w, \text{ where} \\ w = J^{SF} C_{ijkl} \varepsilon_{ij}^e \varepsilon_{kl}^e. \end{cases} \tag{2-32}$$

$C_{ijkl} = C_{ijkl}\left(C^{H}, C^{Li}\right)$ is the elastic modulus which depends on the local material composition in general. $J^{SF} = \det\left(\mathbf{F}^{SF}\right)$ is the Jacobian of the stress-free expansion.

Isotropy

The physical properties of the electrode material are assumed to be isotropic. Specifically, the diffusivities are assumed to be of the forms

$$\left.\begin{array}{l} D_{ik}^{Li} = D^{Li}\delta_{ik}, \text{ and} \\ D_{ik}^{Si} = D^{Si}\delta_{ik}; \end{array}\right\} \tag{2-33}$$

the stress-free expansion is

$$\mathbf{F}^{SF} = \left[J^{SF}\left(C^{H}, C^{Li}\right)\right]^{1/3}\mathbf{I} = V^{SF}\left(C^{H}, C^{Li}\right)\mathbf{I} \;; \tag{2-34}$$

and the elastic response is also assumed to be isotropic such that

$$w = J^{SF}\left[\frac{9}{2}K\varepsilon_{m}^{e\,2} + G\varepsilon_{ij}^{e'}\varepsilon_{ij}^{e'}\right]. \tag{2-35}$$

Here, $\varepsilon_{m}^{e} \equiv \varepsilon_{kk}^{e}/3$ and $\varepsilon_{ij}^{e\prime} \equiv \varepsilon_{ij}^{e} - \varepsilon_{m}^{e}\delta_{ij}$ are, respectively, the isotropic and deviatoric parts of the elastic strain; K and G are the bulk and shear modulus, respectively. $J^{SF} = \det\left(\mathbf{F}^{SF}\right)$ is the stress-free volume change, and $V^{SF} = \left(J^{SF}\right)^{1/3}$ is the associated stretch. Equations (2-10) and (2-35) lead to

$$\sigma_{ij} = F_{iK}^{e}\left(3K\varepsilon_{m}^{e}\delta_{KL} + 2G\varepsilon_{KL}^{e'}\right)F_{jL}^{e}, \tag{2-36}$$

where 2nd order terms of $\boldsymbol{\varepsilon}^e$ have been neglected due to the assumption of small elastic deformation. With Eqs. (2-15), (2-35), and (2-36), the chemical potential of the host and lithium can be shown to be

$$\begin{cases} \mu^{H} = \left.\dfrac{\partial \phi}{\partial C^{H}}\right|_{C^{Li}} - \det\left(\mathbf{F}^{e}\right)\Omega^{H(SF)}\sigma_{m}, \text{ and} \\ \mu^{Li} = \left.\dfrac{\partial \phi}{\partial C^{Li}}\right|_{C^{H}} - \det\left(\mathbf{F}^{e}\right)\Omega^{Li(SF)}\sigma_{m}; \end{cases} \tag{2-37}$$

where $\sigma_m \equiv \sigma_{kk}/3$ is the hydrostatic stress; $\Omega^{H(SF)} \equiv \partial J^{SF}/\partial C^{H}\big|_{C^{Li}}$ and $\Omega^{Li(SF)} \equiv \partial J^{SF}/\partial C^{Li}\big|_{C^{H}}$ are the stress-free partial atomic volume of the host and lithium, respectively.

Under the assumption that elastic strain $\boldsymbol{\varepsilon}^e$ is small and by using Eq. (2-32), Eq. (2-37) can be further simplified into

$$\begin{cases} \mu^{H} = \mu_{SF}^{H} - \det\left(\mathbf{F}^{e}\right)\Omega^{H(SF)}\sigma_{m}, \text{ and} \\ \mu^{Li} = \mu_{SF}^{Li} - \det\left(\mathbf{F}^{e}\right)\Omega^{Li(SF)}\sigma_{m}, \end{cases} \tag{2-38}$$

where

$$\begin{cases} \mu_{SF}^{Li} = \dfrac{\partial \phi^{SF}}{\partial C^{Li}} = \mu_{*}^{Li} + k_{B}\theta \ln \gamma^{Li} x^{Li}, \text{ and} \\ \mu_{SF}^{H} = \dfrac{\partial \phi^{SF}}{\partial C^{H}} = \mu_{*}^{H} + k_{B}\theta \ln \gamma^{H} x^{H} \end{cases} \tag{2-39}$$

are the isothermal chemical potential of host and lithium at zero stress. Here, μ_*^H and μ_*^{Li} are the reference-state chemical potentials; and γ^H and γ^{Li} are the stress-free activity coefficients.

Finally, substituting Eqs. (2-37) and (2-38) into Eqn.(2-29) and neglecting 2nd order terms of $\boldsymbol{\varepsilon}^e$ lead to

$$\begin{cases} J_K^H = -\dfrac{D^H}{k_B\theta} f_{Ki} f_{Ji} C^H \dfrac{\partial \mu_{SF}^H}{\partial X_J} + \dfrac{D^H}{k_B\theta} f_{Ki} f_{Ji} C^H \dfrac{\partial\left[\Omega^{H(SF)}\sigma_m\right]}{\partial X_J}, \text{ and} \\ J_K^{Li} = -\dfrac{D^{Li}}{k_B\theta} f_{Ki} f_{Ji} C^{Li} \dfrac{\partial \mu_{SF}^{Li}}{\partial X_J} + \dfrac{D^{Li}}{k_B\theta} f_{Ki} f_{Ji} C^{Li} \dfrac{\partial\left[\Omega^{Li(SF)}\sigma_m\right]}{\partial X_J}. \end{cases} \qquad (2\text{-}40)$$

To proceed, the dependency of μ_{SF}^{Li} and μ_{SF}^H on the Li composition ξ (or x^{Li} and x^H) need to be specified. According to the Gibbs-Duhem equation, μ_{SF}^{Li} and μ_{SF}^H are mutually dependent and the overall relationship of $\mu_{SF}^{Li} = \mu_{SF}^{Li}(\xi)$ and $\mu_{SF}^H = \mu_{SF}^H(\xi)$ can be reflected by a single function of thermodynamic factor $\Phi(\xi)$ such that

$$\Phi(\xi) \equiv 1 + \frac{x^{Li}}{\gamma^{Li}} \frac{\partial \gamma^{Li}}{\partial x^{Li}} = 1 + \frac{x^H}{\gamma^H} \frac{\partial \gamma^H}{\partial x^H} \ . \qquad (2\text{-}41)$$

This thermodynamic factor characterizes the non-ideality of the binary solution of $Li_\xi H$ [87]. When $\Phi = 1$, the solution model reduces to the ideal solution case. Using the thermodynamic factor [Eqn. (2-41)], Eqn. (2-40) can be transformed into

$$
\begin{cases}
J_K^H = -D^H f_{Ki} f_{Ji} \Phi \cdot \left(x^{Li} \dfrac{\partial C^H}{\partial X_J} - x^H \dfrac{\partial C^{Li}}{\partial X_J} \right) + \dfrac{D^H}{k_B \theta} f_{Ki} f_{Ji} C^H \dfrac{\partial \left[\Omega^{H(SF)} \sigma_m \right]}{\partial X_J}, \text{ and} \\
J_K^{Li} = -D^{Li} f_{Ki} f_{Ji} \Phi \cdot \left(x^H \dfrac{\partial C^{Li}}{\partial X_J} - x^{Li} \dfrac{\partial C^H}{\partial X_J} \right) + \dfrac{D^{Li}}{k_B \theta} f_{Ki} f_{Ji} C^{Li} \dfrac{\partial \left[\Omega^{Li(SF)} \sigma_m \right]}{\partial X_J}.
\end{cases} \tag{2-42}
$$

Generally speaking, $\mu_{SF}^{Li} = \mu_{SF}^{Li}(\xi)$ and $\mu_{SF}^{H} = \mu_{SF}^{H}(\xi)$ [cf. Eqn. (2-39)] can be determined by fitting the activity coefficients γ^{Li} and γ^{H} to experimentally measured open circuit potential (OCP) data [43, 88, 89]. If this approach is used, Eqn. (2-42) is more convenient to calculate the fluxes. On the other hand, if the model is based on simplifying assumptions such as the ideal solution assumption [20, 45, 90-92], regular solution assumption [93-95], or lattice-gas assumption [96-98], Eqn. (2-40) allows easier calculation of fluxes than Eqn. (2-42).

In the results and discussions part (i.e. chapter 4 and chapter 5), section 4.1 and 4.3 are based on chemical potentials fitted using OCP data, and therefore use Eqn. (2-42); section 4.2 and chapter 5 are based on the idealized $\mu_{SF}^{Li} = \mu_{SF}^{Li}(\xi)$ curve , and therefore use Eqn. (2-40).

Yield surface and flow rule

The plastic deformation is assumed to follow an associated flow rule with a composition-dependent yield surface $\boldsymbol{\sigma}_Y = \boldsymbol{\sigma}_Y(\xi)$, i.e.,

$$
Q = \frac{1}{2} \boldsymbol{\sigma}^{dev} : \boldsymbol{\sigma}^{dev} - \frac{1}{3} \left(\boldsymbol{\sigma}_Y \right)^2 = 0 \ , \tag{2-43}
$$

where $\boldsymbol{\sigma}^{dev} \equiv \boldsymbol{\sigma} - tr(\boldsymbol{\sigma})/3\mathbf{I}$ is the deviatoric part of the Cauchy stress. Below the yielding threshold, $\mathbf{D}$ [Eqn. (2-2)] is simply given by the rate form of Eqs.(2-36) and (2-34), i.e.

$$\mathbf{D} = \left(\frac{1}{9K} - \frac{1}{6G}\right) tr\left(\overset{\circ}{\boldsymbol{\sigma}}\right)\mathbf{I} + \frac{\overset{\circ}{\boldsymbol{\sigma}}}{2G} + \frac{1}{3}\left[\frac{\partial\left(\ln J^{SF}\right)}{\partial C^{Li}}\dot{C}^{Li} + \frac{\partial\left(\ln J^{SF}\right)}{\partial C^{H}}\dot{C}^{H}\right]\mathbf{I}. \qquad (2\text{-}44)$$

Here, $\overset{\circ}{\boldsymbol{\sigma}} \equiv \dot{\boldsymbol{\sigma}} - \mathbf{W}\cdot\boldsymbol{\sigma} + \boldsymbol{\sigma}\cdot\mathbf{W}$ is the objective Jaumann rate of $\boldsymbol{\sigma}$, with $\mathbf{W} = \left(\mathbf{L} - \mathbf{L}^{T}\right)/2$ being the spin tensor. Upon yielding, the rate of deformation including plasticity is [cf. Eqn. (2-28)]

$$\begin{aligned}\mathbf{D} = {} & \left(\frac{1}{9K} - \frac{1}{6G}\right) tr\left(\overset{\circ}{\boldsymbol{\sigma}}\right)\mathbf{I} + \frac{\overset{\circ}{\boldsymbol{\sigma}}}{2G} \\ & + \frac{1}{3}\left[\frac{\partial\left(\ln J^{SF}\right)}{\partial C^{Li}}\dot{C}^{Li} + \frac{\partial\left(\ln J^{SF}\right)}{\partial C^{H}}\dot{C}^{H}\right]\mathbf{I} + \dot{\lambda}\frac{\partial Q}{\partial \boldsymbol{\sigma}}.\end{aligned} \qquad (2\text{-}45)$$

where the scalar rate factor $\dot{\lambda}$ can be determined from plastic consistency conditions if plastic model is used [69-71, 75], or from the stress-strain rate relationship if visco-plastic model is used [15, 37].

For perfectly plastic case with no strain hardening but lithiation-induced softening, closed-form relationship between $\dot{\lambda}$ and stress state takes the form of

$$\dot{\lambda} = \frac{3}{2}\frac{1}{\sigma_Y^2}\mathbf{D}:\boldsymbol{\sigma}^{dev} + \frac{1}{2G}\frac{\frac{\partial \sigma_Y}{\partial \xi}}{\sigma_Y}\dot{\xi}^{Li}. \qquad (2\text{-}46)$$

In finite element implementations, however, relationship of Eq. (2-46) is generally inconvenient to use, and $\dot{\lambda}$ is solved by using the so-called return-mapping algorithm (see section 3.4).

3. Numerical framework based on the mixed finite element method

In equation (2-40) [and also Eqn. (2-42)], the diffusion fluxes of the host and guest consist of two parts each. The stress-free (chemical) parts

$$\begin{cases} J_K^{H,chem} = -D^H f_{Ki} f_{Ji} \Phi \cdot \left(x^{Li} \dfrac{\partial C^H}{\partial X_J} - x^H \dfrac{\partial C^{Li}}{\partial X_J} \right), \text{ and} \\ J_K^{\mathrm{Li},chem} = -D^{Li} f_{Ki} f_{Ji} \Phi \cdot \left(x^H \dfrac{\partial C^{Li}}{\partial X_J} - x^{Li} \dfrac{\partial C^H}{\partial X_J} \right) \end{cases} \tag{3-1}$$

are due to chemical interactions between the guest and host atoms. The mechanical parts

$$\begin{cases} J_K^{H,mech} = \dfrac{D^H}{k_B \theta} f_{Ki} f_{Ji} C^H \dfrac{\partial \left[\Omega^{H(SF)} \sigma_m \right]}{\partial X_J}, \text{ and} \\ J_K^{Li,mech} = \dfrac{D^{Li}}{k_B \theta} f_{Ki} f_{Ji} C^{Li} \dfrac{\partial \left[\Omega^{Li(SF)} \sigma_m \right]}{\partial X_J} \end{cases} \tag{3-2}$$

are due to stresses which tend to squeeze the atoms from compressive regions to tensile regions; $J_K^{H,mech}$ and $J_K^{Li,mech}$ embody what is termed “mechanical-to-chemical” coupling. To illustrate the significance of this coupling, consider a piece of $\mathrm{Li}_\xi\mathrm{Si}$ alloy in which ξ is spatially homogeneous and Si is immobile. If one side of the alloy is compressed and the other side is stretched, the resultant stress gradient would induce a driving force that squeezes lithium from the compressive side to the tensile side, as shown in Fig. 3.1. It has been suggested that the stress-induced contributions may significantly affect concentrations and stresses in Li-ion battery electrodes [45, 99]. For nanowire electrodes made of Li/Si, the stress effect could amount to a 303% increase in the effective diffusivity, thereby significantly decrease the stress levels [43]. Therefore, $J_K^{H,mech}$ and $J_K^{Li,mech}$ must be captured to correctly evaluate the stress levels and assess resulting failure in Li-alloy electrodes.

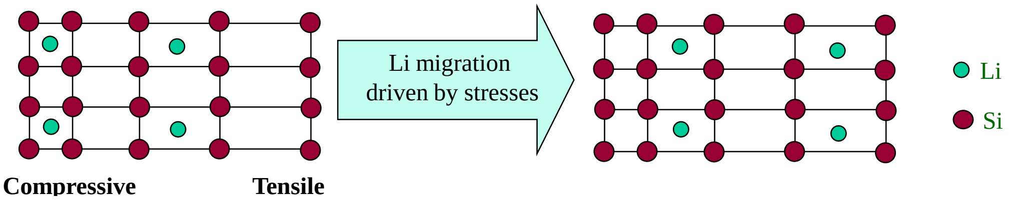

Fig. 3.1 Illustration of lithium migration driven by mechanical stress. Such an effect can be described by considering a stress-induced chemical potential shift.

One of the major numerical challenges here is associated with the gradient of hydrostatic stress (i.e. $\partial\sigma_m / \partial X_J$) that appears in eqn. (3-2) when a finite element (FE) method is used. Since $\partial\sigma_m / \partial X_J \propto \partial\varepsilon_m^e / \partial X_J$, either the strain gradient or the stress gradient itself has to be calculated numerically. Tang et al. [93] used a finite difference method to calculate the diffusion-stress coupling in olivine electrodes and successfully reproduced the phase transformation characteristics observed in experiments. The benefit of using a finite difference scheme is that one automatically captures the 2nd-order deformation gradient by using appropriate discretized gradient operators. The finite element method, however, is more valuable if geometric shapes other than rectangles are involved.

When a linear interpolation is used with a finite element, the information of strain gradient is lost since the diagonal terms of the interpolator's spatial Hessian are always zero. One remedy is to use elements with high-order polynomials as the interpolation functions. Another strategy is to compute the 2^{nd} order deformation gradients by fitting to nodal displacements across several adjacent elements, instead of relying only on the nodal values of one specific element under consideration [100]. These methods fall into the category of irreducible finite element methods.

Bower and Guduru [46] and Gao et al. [43] independently proposed methods that leverage the concept of mixed finite elements [101] to simulate the diffusion/deformation two–way coupling. Instead of using only the deformation and concentration of the diffusion species as nodal variables, the hydrostatic stress σ_m [43] or the Li chemical potential μ^{Li} [46] can also be treated as a redundant degree of freedom, thereby automatically resolve the relevant gradient needed by Fick's law. This chapter covers the mixed finite element framework [18] that we have developed for the diffusion/deformation two-way coupling problem.

3.1. Variational form of the mixed finite element

The mixed FE method was originally proposed to avoid numerical singularity in problems of incompressible solids, for which the hydrostatic stress σ_m cannot be well-defined in terms of the displacement field. As a remedy, the hydrostatic stress can be introduced as a Lagrangian multiplier to enforce the incompressibility, hence the name "mixed" finite element. Similar concepts were later adopted to capture the strain gradient effects in non-local theories of plasticity by treating either the rotation or the full deformation gradient as redundant variables [102, 103]. Mixed FE methods have also been used in soil mechanics, in which transport of incompressible fluid in porous media is mainly driven by pressure gradients [104]. Here, we treat the hydrostatic stress $\sigma_m(\mathbf{X}, t)$ as though it was an independent field variable in order to facilitate the calculation of its gradients. We call σ_m a redundant variable, in contrast to truly independent field variables such as $\mathbf{u}(\mathbf{X},t)=\mathbf{x}-\mathbf{X}$, C^H and C^{Li}. This redundant variable is implicitly constrained by eqn. (2-36), i.e.,

$$3\varepsilon_m^e - \sigma_m / K = 0. \tag{3-3}$$

Here, 2nd order terms of $\boldsymbol{\varepsilon}^e$ are neglected in the derivation of eqn. (3-3). Since $\det(\mathbf{F}) = \det(\mathbf{F}^e)\det(\mathbf{F}^{SF}) = \det(\mathbf{F}^e) J^{SF}$ and $\varepsilon_m^e \approx \left(\det(\mathbf{F}^e) - 1\right)/3$, the constraint condition in Eqn. (3-3) can be restated in the variational form of

$$\int_V \left[\frac{\det(\mathbf{F})}{J^{SF}\left(C^H, C^{Li}\right)} - 1 - \frac{\sigma_m}{K} \right] \delta\sigma_m dV = 0, \tag{3-4}$$

where $\int_V (\bullet) dV$ stands for integration over the current configuration of the body. The same constraint in the Lagrangain domain V_0 is

$$\int_{V_0} \det(\mathbf{F}) \left[\det(\mathbf{F}) / J^{SF} - 1 - \sigma_m / K \right] \delta\sigma_m dV_0 = 0. \tag{3-5}$$

The variational statement of the conservation of momentum [Eqn. (2-5)], on the other hand, takes the standard form

$$\int_{V_0} \sigma_{Ji}^{PK1} \frac{\partial \delta u_i}{\partial X_J} dV_0 = \int_{S_0} T_i \delta u_i dS_0 + \int_{V_0} B_i \cdot \delta u_i dV_0 \ , \tag{3-6}$$

where $\sigma_{Ji}^{PK1} = \det(\mathbf{F}) f_{Jj} \sigma_{ji}$ and

$$\sigma_{ij} = \sigma_m \delta_{ij} + \sigma_{ij}^{dev}. \tag{3-7}$$

Here, σ_m is treated as an independent variable. $\int_{S_0} (\bullet) dS_0$ stands for integration over the surface of the Lagrangian domain. **T** and **B** are the surface traction and body forces in the Lagrangian frame, respectively.

Finally, the conservation of mass [Eqs. (2-4)] requires

$$\begin{aligned} \int_{V_0} \left. \frac{\partial C^S}{\partial t} \right|_{\mathbf{X}} \cdot \delta C^S \, dV_0 &= \int_{V_0} J_K^S \frac{\partial \delta C^S}{\partial X_K} dV_0 \\ &+ \int_{V_0} R_b^S \delta C^S \, dV_0 + \int_{S_0} Q^S \delta C^S \, dS_0, \left(S = Li, H \right), \end{aligned} \tag{3-8}$$

where Q^{Li} and Q^H are the Lagrangian surface influxes. The fluxes J_K^{Li} and J_K^H are given by Eqn. (2-40), with σ_m being treated as an independent variable.

3.2. Discretization

The variational forms in Eqn. (3-4)-(3-8) are discretized using the FE interpolations of

$$\begin{cases} \mathbf{x}\left(\mathbf{X},t\right)=\sum\limits_{a} N_a^{\mathbf{x}}\left(\mathbf{X}\right)\mathbf{x}_a\left(t\right), \\ C^{Li}\left(\mathbf{X},t\right)=\sum\limits_{a} N_a^{C}\left(\mathbf{X}\right)C_a^{Li}\left(t\right), \\ C^{H}\left(\mathbf{X},t\right)=\sum\limits_{a} N_a^{C}\left(\mathbf{X}\right)C_a^{H}\left(t\right), \text{ and} \\ \sigma_m\left(\mathbf{X},t\right)=\sum\limits_{a} N_a^{\sigma_m}\left(\mathbf{X}\right)\sigma_m^a\left(t\right), \end{cases} \tag{3-9}$$

where $N_a^{\mathbf{x}}\left(\mathbf{X}\right)$, $N_a^{C}\left(\mathbf{X}\right)$ and $N_a^{\sigma_m}\left(\mathbf{X}\right)$ are shape functions for the displacement, concentration and hydrostatic stress degrees of freedom (DOF), respectively; $\mathbf{x}_a\left(t\right)$, $C_a^{Li}\left(t\right)$, $C_a^{H}\left(t\right)$ and $\sigma_m^a\left(t\right)$ are the corresponding time-dependent nodal values. Here, 2nd order isoparametric shape functions are used for $N_a^{\mathbf{x}}\left(\mathbf{X}\right)$ and linear isoparametric shape functions are chosen for $N_a^{C}\left(\mathbf{X}\right)$ and $N_a^{\sigma_m}\left(\mathbf{X}\right)$ [cf. Fig. 3.2]. This interpolation scheme gives sufficient accuracy for the $\partial\sigma_m/\partial X_J$ effect in Eqn. (3-2) yet does not introduce too many redundant DOF which may result in singular Jacobian matrices [101].

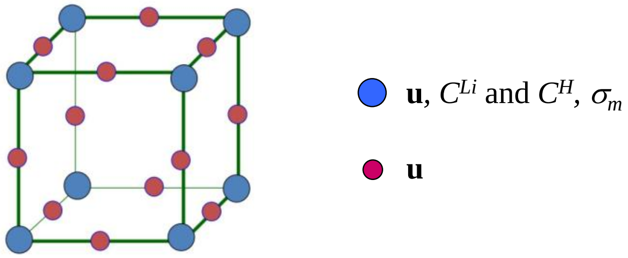

Fig. 3.2 The mixed finite element used to calculate deformation/interdiffusion coupling in alloy-based electrodes. 2nd order isoparametric shape functions are used for displacement and linear isoparametric shape functions are used for concentration and pressure. The corner nodes have displacement, concentration and hydrostatic stress DOF and the edge nodes only have displacement DOF.

Substitution of Eqn. (3-9) into (3-6) leads to

$$\sum_a \left[-\int_{V_0} \sigma_{Ji}^{PK1} \frac{\partial N_a^{\mathbf{x}}}{\partial X_J} dV_0 + \int_{S_0} T_i \cdot N_a^{\mathbf{x}} dS_0 + \int_{V_0} B_i \cdot N_a^{\mathbf{x}} dV_0 \right] \delta u_{ai} = 0. \qquad \text{(3-10)}$$

The nodal force which is work-conjugate to δu_{ai} is, therefore,

$$F_{u_{ai}}\left(t\right) \equiv -\int_{V_0} \sigma_{Ji}^{PK1} \frac{\partial N_a^{\mathbf{x}}}{\partial X_J} dV_0 + \int_{S_0} T_i \cdot N_a^{\mathbf{x}} dS_0 + \int_{V_0} B_i \cdot N_a^{\mathbf{x}} dV_0, \qquad \text{(3-11)}$$

where the stress is given by eqn. (3-7). By the same token, the residual associated with the $\delta C_a^S \left(S = Li, H\right)$ DOF is

$$\begin{aligned} F_{C_a^S}\left(t\right) \equiv & -\sum_b \kappa_{ab} \dot{C}_b^S + \int_{V_0} J_K^S \frac{\partial N_a^C}{\partial X_K} dV_0 \\ & + \int_{V_0} R_b^S N_a^C \, dV_0 + \int_{S_0} Q^S N_a^C \, dS_0, \left(S = Li, H\right), \end{aligned} \qquad \text{(3-12)}$$

where $\kappa_{ab} \equiv \int_{V_0} N_a^C N_b^C dV_0$ is the consistent capacity matrix.

Finally, substitution of eq. (3-9) into the constraint condition in Eqs. (3-5) yields the requirement

$$\sum_a \left\{ \int_{V_0} \det\left(\mathbf{F}\right) \left[\det\left(\mathbf{F}\right) / J^{SF} - 1 - \sigma_m / K \right] N_a^{\sigma_m}\left(\mathbf{X}\right) dV_0 \delta\sigma_m^a \right\} = 0. \qquad \text{(3-13)}$$

The residual associated with the $\delta\sigma_m^a$ DOF is, therefore,

$$F_{\sigma_m^a}(t) \equiv -\int_{V_0} \det(\mathbf{F})\left[\det(\mathbf{F})/J^{SF} - 1 - \sigma_m/K\right] N_a^{\sigma_m} dV_0 \quad . \tag{3-14}$$

Now, the deformation/diffusion coupling problem had been reduced to a set of nonlinear ODEs that must be satisfied for all nodes:

$$F_{u_{ai}}(t) = 0, \quad F_{\sigma_m^a}(t) = 0, \quad F_{C_a^S}(t) = 0. \tag{3-15}$$

To proceed, we need to further discretize the time variable. For increment (t_n, t_{n+1}), we use the unconditionally stable backward Euler integration scheme, i.e.,

$$\begin{aligned} F_{C_a^S}(t_{n+1}) \approx & -\sum_b \kappa_{ab} \frac{C_b^S(t_{n+1}) - C_b^S(t_n)}{\Delta t_{n+1}} + \int_{V_0} J_K^S(t_{n+1}) \frac{\partial N_a^C}{\partial X_K} dV_0 \\ & + \int_{V_0} R_b^S(t_{n+1}) N_a^C dV_0 + \int_{S_0} Q^S(t_{n+1}) N_a^C dS_0, (S = Li, H), \end{aligned} \tag{3-16}$$

where $\Delta t_{n+1} \equiv t_{n+1} - t_n$ is time increment of interval (t_n, t_{n+1}). The diffusion fluxes J_K^S, body source/sink R_b^S and surface influx Q^S should be evaluated at the end of (t_n, t_{n+1}), as indicated by eqn. (3-16). The first two equations in (3-15), on the other hand, can be discretized by simply evaluating Eqs. (3-11) and (3-14) at time t_{n+1}, i.e.,

$$\begin{cases} F_{u_{ai}}(t_{n+1}) = 0, \text{ and} \\ F_{\sigma_m^a}(t_{n+1}) = 0. \end{cases} \tag{3-17}$$

3.3. The Hughes-Winget algorithm and the corrotational frame

If the constitutive law for stresses were of a total strain vs. total stress form, as in the case of elastic and hyperelastic materials, the first equation in (3-15) would be simply a non-linear algebraic equation. The third of Eqn. (3-15), of course, is an ordinary differential equation which requires further discretization in the time domain; this discretization has been achieved by Eqn. (3-16).

Because the stresses-strain relationship is incremental in this study [cf. Eqs. (2-45) and (2-44)], the first equation of (3-15) is an differential equation even when no inertial force (i.e. no kinetic energy) is considered: here, a differential operator $\partial / \partial t$ enters the first equation of (3-15) via the rate of deformation $\mathbf{D}$ of Eqs. (2-45) and (2-44).

Since $F_{u_{ai}}(t) = 0$ is a time-dependent ordinary differential equation when Eqn. (2-44) or (2-45) is substituted into it, it needs to be further discretized in the time domain. There are two challenges in doing this:

1) To compute $\mathbf{D}$ or its time integration during the increment (t_n, t_{n+1}) accurately and efficiently from the nodal coordinates $\mathbf{x}_a(t_n)$ and $\mathbf{x}_a(t_{n+1})$.

2) To compute the spin tensor $\mathbf{W} = \left(\mathbf{L} - \mathbf{L}^T\right)/2$ during the increment (t_n, t_{n+1}) accurately and efficiently from the nodal coordinates $\mathbf{x}_a(t_n)$ and $\mathbf{x}_a(t_{n+1})$, so that stress rate $\dot{\boldsymbol{\sigma}}$ can be computed from the Jaumann objective rate $\overset{\circ}{\boldsymbol{\sigma}}$ and $\mathbf{W}$ by using the relationship

$$\overset{\circ}{\boldsymbol{\sigma}} \equiv \dot{\boldsymbol{\sigma}} - \mathbf{W} \cdot \boldsymbol{\sigma} + \boldsymbol{\sigma} \cdot \mathbf{W} \qquad (3\text{-}18)$$

The above two challenges motivate the usage of Hughes-Winget algorithm [105] in our mixed finite element framework. This algorithm calculates and integrates the rate of deformation $\mathbf{D}$ and the spin tensor $\mathbf{W}$ on appropriate Gaussian integration points by using the following approximations:

1) The time integral of $\mathbf{D}$ during increment $\left(t_n, t_{n+1}\right)$, denoted by $\Delta\boldsymbol{\varepsilon}$ and evaluated on Gaussian integration points, is approximated by the central difference formula as

$$\Delta\boldsymbol{\varepsilon} \equiv \int_{t_n}^{t_{n+1}} \mathbf{D} dt \approx sym\left[\frac{\partial \Delta\mathbf{x}}{\partial\left(\mathbf{x}_t + \Delta\mathbf{x}/2\right)}\right], \tag{3-19}$$

   where $\mathbf{x}_t$ is the Eulerian coordinate of the Gaussian point where $\Delta\boldsymbol{\varepsilon}$ is evaluated. Here, $\mathbf{x}_t = \mathbf{x}\left(t_n\right)$ denotes the value at the beginning of the increment $\left(t_n, t_{n+1}\right)$; $\Delta\mathbf{x} \equiv \mathbf{x}_{t+\Delta t} - \mathbf{x}_t$ is the increment of $\mathbf{x}(t)$ during $\left(t_n, t_{n+1}\right)$; and $\mathbf{x}_{t+\Delta t} = \mathbf{x}\left(t_{n+1}\right)$ is the Eulerian coordinate at the end of the increment. All geometric quantities, namely $\mathbf{x}_t$, $\mathbf{x}_{t+\Delta t}$ and thus $\Delta\boldsymbol{\varepsilon}$, are evaluated on Gaussian points.

   When isoparametric interpolation of Eqn. (3-9) is used, the spatial gradient $\partial/\partial\left(\mathbf{x}_t + \Delta\mathbf{x}/2\right)$ can be evaluated by

$$\frac{\partial}{\partial\left(\mathbf{x}_t + \Delta\mathbf{x}/2\right)} = \frac{\partial\mathbf{g}}{\partial\left(\mathbf{x}_t + \Delta\mathbf{x}/2\right)}\frac{\partial}{\partial\mathbf{g}} = \left(\frac{\partial\left(\mathbf{x}_t + \Delta\mathbf{x}/2\right)}{\partial\mathbf{g}}\right)^{-1}\frac{\partial}{\partial\mathbf{g}}, \tag{3-20}$$

   where $\mathbf{g}$ denotes the isoparametric element coordinates of the master element.

2) The integral of $\mathbf{W}$ during increment $\left(t_n, t_{n+1}\right)$, denoted by $\Delta\mathbf{W}$ and evaluated on Gaussian integration points, is also approximated by central difference formula as

$$\Delta\mathbf{W} \equiv \int_{t_n}^{t_{n+1}} \mathbf{W} dt \approx asym\left[\frac{\partial \Delta\mathbf{x}}{\partial\left(\mathbf{x}_t + \Delta\mathbf{x}/2\right)}\right]. \tag{3-21}$$

Again, the spatial gradient $\partial / \partial\left(\mathbf{x}_t + \Delta\mathbf{x}/2\right)$ can be evaluated by Eqn. (3-20).

The increment of rotation $\Delta\mathbf{R}$ on the Gaussian integration point is given by

$$\Delta\mathbf{R} = \left(\mathbf{I} - \frac{1}{2}\Delta\mathbf{W}\right)^{-1} \cdot \left(\mathbf{I} + \frac{1}{2}\Delta\mathbf{W}\right) \tag{3-22}$$

One advantage of the Hughes-Winget algorithm is the introduction of the so-called corrotational coordinate system on Gaussian points via Eqn. (3-22). A corrotational system, by definition, rotates together with the local material; therefore the material locomotion has no rotational component in the corrotational frame. For a tonsorial quantity **a**, its time rate $\partial\mathbf{a}/\partial t$ observed in the corrotational frame will be equal an objective rate in the global, non-rotating frame. Depending how the local rigid body motion is defined and how the corrotational frame is attached to the material, the corrotational rate can correspond to the Jaumann rate, the Green-Naghdi rate, or some other types of objective rate in the global reference frame. Here, the rotation given by the Hughes-Winget algorithm [Eqn. (3-22)] defines a frame whose corrotational rate approximates the Jaumann rate of Eqn. (3-22). This approximation is widely used in many commercial and academic codes, including in the built-in geometric non-linearity module of commercial software ABAQUS.

Practically, the introduction of corrotational frame via the Hughes-Winget algorithm allows

1) the decomposition of stress increment $\boldsymbol{\sigma}_{t+\Delta t} - \boldsymbol{\sigma}_t$, which is measured in the global non-rotating frame, into two parts:

$$\boldsymbol{\sigma}_{t+\Delta t} - \boldsymbol{\sigma}_t = \left(\Delta\mathbf{R} \cdot \boldsymbol{\sigma}_t \cdot \Delta\mathbf{R}^T - \boldsymbol{\sigma}_t\right) + \Delta\breve{\boldsymbol{\sigma}}\left(\Delta\boldsymbol{\varepsilon}, \Delta C^H, \Delta C^{Li}, \Delta\sigma_m, \Delta t\right), \tag{3-23}$$

the first part being the change of stress tensor due to rigid body rotation of the whole material, and the second part ($\Delta\breve{\boldsymbol{\sigma}}$) being the corrotational change of $\boldsymbol{\sigma}$, measured in the corrotational frame; and

2) the computation of corrotational increment $\Delta\breve{\boldsymbol{\sigma}}$ by using the objective constitutive equations [i.e. Eqs. (2-44) and (2-45)] and by simply equating the corrotational rate and the Jaumann rate.

To compute the corrotational increment $\Delta\breve{\boldsymbol{\sigma}}$ during increment $\left(t_n, t_{n+1}\right)$, one needs to integrate Eqs. (2-44) and (2-45) which reflect the material non-linearity of the mechanical response. This can be achieved by using the return-mapping algorithm, as will be discussed in the next section.

3.4. The return-mapping algorithm for incremental inelastic flow

In a corrotational frame, material does not undergo rigid body rotation, and the material time rate is equal to the objective time rate. This section describes the return-mapping algorithm used in our mixed finite element framework for the integration of Eqs. (2-44) and (2-45). The aim is to calculate $\Delta\breve{\boldsymbol{\sigma}}$, namely the change of $\boldsymbol{\sigma}$ during increment $\left(t_n, t_{n+1}\right)$ measured in the corrotational frame. Because the discussion in this section is exclusively carried out in corrotational frames, we denote $\Delta\breve{\boldsymbol{\sigma}}$ by $\Delta\boldsymbol{\sigma}$ for simplicity of notations; this simplification of notation is used only here in section 3.4.

To integrate Eqs. (2-44) and (2-45), one takes $\Delta\boldsymbol{\varepsilon}$, $\Delta C^H, \Delta C^{Li}, \Delta\sigma_m$, and possibly Δt if the response is viscous and time dependent, as input, and solves for the corrotational stress increment $\Delta\boldsymbol{\sigma}$. In this study, we consider elasto-plastic model without viscous effect (i.e. no rate effect on stresses), and the task of integrating Eqs. (2-44) and (2-45) reduces to finding the following relationship

$$\Delta\boldsymbol{\sigma} = \Delta\boldsymbol{\sigma}\left(\Delta\boldsymbol{\varepsilon}, \Delta C^{H}, \Delta C^{Li}, \Delta\sigma_{m}\right) , \tag{3-24}$$

where $\Delta\boldsymbol{\varepsilon}, \Delta C^{H}, \Delta C^{Li}$ and $\Delta\sigma_{m}$ are inputs provided by the nodal variables via interpolation of Eqn. (3-9) and Hughes-Winget algorithm via Eqn. (3-19). During the finite element analysis, the calculation specified by Eqn. (3-24) is carried out on each Gaussian points of every element.

The history-dependency of incremental plastic models requires yet two other inputs to Eqn. (3-24): the stress state $\boldsymbol{\sigma}_{t} = \boldsymbol{\sigma}(t)$ and the yield threshold $\sigma_{Y}(t)$ at the beginning of the increment (t_{n}, t_{n+1}). These two quantities are not given by the nodal variables of Eqn. (3-9). Instead, they are state variables associated with integration points where calculation of (3-24) is carried out. It should be noted that the plastic models used in this study are perfectly plastic without strain hardening, because of the lack of experimental data on the hardening rate. In numerical computations, however, perfect plastic models give rise to instability and numerical difficulties when an implicit integration scheme is used. We therefore use a very small strain hardening slope to mimic perfectly plastic behavior and to stabilize the numerical computation.

The return-mapping algorithm works by first assuming that the material response in every increment (t_{n}, t_{n+1}) is elastic, and then by checking the validity of this assumption. If the final stress state $\boldsymbol{\sigma}_{t+\Delta t}$ given by Eqn. (2-44) falls out of the yield surface, one rules out the possibility of elastic response and re-calculates $\boldsymbol{\sigma}_{t+\Delta t}$ by using the plastic equation of (2-45).

Specifically, by assuming elastic response, the final stress state $\boldsymbol{\sigma}_{t+\Delta t}$, measured in the corrotational frame, is given by solving $\mathbf{S}_{t+\Delta t}$ from

$$\Delta\boldsymbol{\varepsilon} = \left(\frac{\mathbf{S}_{t+\Delta t}}{2G_{t+\Delta t}} - \frac{\mathbf{S}_t}{2G_t} \right) + \left(\frac{\sigma_{m,t+\Delta t}}{3K_{t+\Delta t}} - \frac{\sigma_{m,t}}{3K_t} \right)\mathbf{I} + \\ \frac{1}{3}\frac{d\ln J^{\boldsymbol{SF}}}{dC^H}\bigg|_{t+\Delta t/2} \left(C^H_{t+\Delta t} - C^H_t \right)\mathbf{I} + \frac{1}{3}\frac{d\ln J^{\boldsymbol{SF}}}{dC^{Li}}\bigg|_{t+\Delta t/2} \left(C^{Li}_{t+\Delta t} - C^{Li}_t \right)\mathbf{I}. \tag{3-25}$$

Here, $\mathbf{S} \equiv \boldsymbol{\sigma}^{dev}$ is the deviatoric part of the Cauchy stress $\boldsymbol{\sigma}$; K and G are the composition-dependent bulk and shear modulus.

The von Mises stress $q_{t+\Delta t}$ associated with $\mathbf{S}_{t+\Delta t}$ is

$$q_{t+\Delta t} \equiv \sqrt{\frac{3}{2}\mathbf{S}_{t+\Delta t} : \mathbf{S}_{t+\Delta t}} \ . \tag{3-26}$$

If $q_{t+\Delta t} < \sigma_Y(t)$, the elastic assumption is correct, and the corrotational stress increment is simply

$$\Delta\boldsymbol{\sigma} = \mathbf{S}_{t+\Delta t} + \sigma_{m,t+\Delta t}\mathbf{I} - \boldsymbol{\sigma}_t \ , \tag{3-27}$$

where $\mathbf{S}_{t+\Delta t}$ is the solution of Eqn. (3-25); if $q_{t+\Delta t} \geq \sigma_Y(t)$, however, the elastic assumption is incorrect and plastic increment should be considered such that [cf. Eqn. (2-45)]

$$\Delta\boldsymbol{\varepsilon} = \left(\frac{\mathbf{S}_{t+\Delta t}}{2G_{t+\Delta t}} - \frac{\mathbf{S}_t}{2G_t} \right) + \left(\frac{\sigma_{m,t+\Delta t}}{3K_{t+\Delta t}} - \frac{\sigma_{m,t}}{3K_t} \right)\mathbf{I} +$$

$$\frac{1}{3}\frac{d\ln J^{SF}}{dC^H}\bigg|_{t+\Delta t/2} \left(C^H_{t+\Delta t} - C^H_t \right)\mathbf{I} + \frac{1}{3}\frac{d\ln J^{SF}}{dC^{Li}}\bigg|_{t+\Delta t/2} \left(C^{Li}_{t+\Delta t} - C^{Li}_t \right)\mathbf{I} \qquad (3\text{-}28)$$

$$+\Delta\mathbf{e}_{pl}.$$

Here, $\Delta\mathbf{e}_{pl} = \dot{\lambda}\mathbf{S}_{t+\Delta t}\Delta t$ is the plastic strain increment during $\left(t_n, t_{n+1}\right)$. By defining the effective plastic strain increment $\Delta\overline{e}_{pl}$ as

$$\Delta\overline{e}_{pl} \equiv \sqrt{\frac{2}{3}\Delta\mathbf{e}_{pl} : \Delta\mathbf{e}_{pl}} \ , \qquad (3\text{-}29)$$

the plastic strain $\Delta\mathbf{e}_{pl}$ increment is given by Eqs. (3-26) and (3-29) to be

$$\Delta\mathbf{e}_{pl} = \frac{3}{2}\frac{\mathbf{S}_{t+\Delta t}}{q_{t+\Delta t}}\Delta\overline{e}_{pl} \qquad (3\text{-}30)$$

In this study, we consider rate-independent plasticity with small but finite strain-hardening for numerical stability, such that

$$\sigma_Y = \sigma_Y\left(\xi, \overline{e}_{pl}\right) \ , \qquad (3\text{-}31)$$

where ξ is the Li composition in Li$_\xi$H; $\overline{e}_{pl}$ is the total effective plastic integrated from

$$\overline{e}_{pl} \equiv \int_0^t \sqrt{\frac{2}{3}\dot{\mathbf{e}}_{pl} : \dot{\mathbf{e}}_{pl}}\,dt \approx \sum_{i=1}^{n} \Delta\overline{e}_{pl}^{\left(t_n, t_{n+1}\right)} \qquad (3\text{-}32)$$

By using Eqs. (3-30), the deviatoric part of Eqn. (3-28) is

$$\Delta \mathbf{e} = \left(\frac{\mathbf{S}_{t+\Delta t}}{2G_{t+\Delta t}} - \frac{\mathbf{S}_t}{2G_t} \right) + \Delta \bar{e}_{pl} \frac{3}{2} \frac{\mathbf{S}_{t+\Delta t}}{q_{t+\Delta t}} \ , \tag{3-33}$$

where $\Delta \mathbf{e} \equiv \Delta \boldsymbol{\varepsilon} - \left(tr\left(\Delta \boldsymbol{\varepsilon}\right) \mathbf{I} \right) / 3$ is the deviatoric part of the total strain increment. Rearrange Eqn. (3-33) gives

$$\Delta \mathbf{e} + \frac{\mathbf{S}_t}{2G_t} = \left(\frac{1}{2G_{t+\Delta t}} + \frac{3\Delta \bar{e}_{pl}}{2q_{t+\Delta t}} \right) \mathbf{S}_{t+\Delta t} \ ; \tag{3-34}$$

and therefore,

$$\left(\Delta \mathbf{e} + \frac{\mathbf{S}_t}{2G_t} \right) : \left(\Delta \mathbf{e} + \frac{\mathbf{S}_t}{2G_t} \right) = \frac{3}{2} \left(\frac{q_{t+\Delta t}}{3G_{t+\Delta t}} + \Delta \bar{e}_{pl} \right)^2 \ . \tag{3-35}$$

On the other hand, consistency condition requires

$$q_{t+\Delta t} = \sigma_Y \left(t_{t+\Delta t} \right) = \sigma_Y \left(\xi_{t+\Delta t}, \bar{e}_{pl}^{t=t_n} + \Delta \bar{e}_{pl} \right) \ , \tag{3-36}$$

where $\bar{e}_{pl}^{t=t_n}$ is the total effective plastic strain at the beginning of the increment.

Equations (3-35) and (3-36) are two scalar equations with two unknowns: $\Delta \bar{e}_{pl}$ and $q_{t+\Delta t}$. These two unknowns can be solved by using the Newton-Raphson method.

Finally, once $\Delta \bar{e}_{pl}$ and $q_{t+\Delta t}$ are solved, the deviatoric stress $\mathbf{S}_{t+\Delta t}$ is given by

$$\mathbf{S}_{t+\Delta t} = \left(\Delta \mathbf{e} + \frac{\mathbf{S}_t}{2G_t} \right) / \left(\frac{1}{2G_{t+\Delta t}} + \frac{3\Delta \bar{e}_{pl}}{2q_{t+\Delta t}} \right) . \tag{3-37}$$

3.5. Implementation as Abaqus UEL

The 3D mixed finite element framework is implemented using the UEL interface of ABAQUS Standard 6.11. Gaussian quadrature is used to integrate the residuals, with 27 integration points for $F_{u_{ai}}$ and 8 integration points for $F_{C_a^S}$ and $F_{\sigma_m^a}$. Since the well-known Newtown iteration method is used by ABAQUS to solve the non-linear equations in (3-16) and (3-17), Jacobians of $F_{u_{ai}}$, $F_{C_a^S}$ and $F_{\sigma_m^a}$ with respect to nodal variables at t_{n+1} are needed. The derivation of these Jacobians is not elaborated here.

4. The deformation-diffusion two-way coupling

We have outlined the theoretical and numerical framework for the deformation-diffusion two-way coupled problem in Chapter 2 and 3. This coupling has two aspects: chemical-to-mechanical (CM) coupling, i.e. the deformation induced by composition change, and the mechanical-to-chemical (MC) coupling, i.e. the lithium migration driven by stress gradient. This chapter addresses on the numerical results and physical implications, with a focus on the effect of mechanical to chemical (MC) coupling on lithium diffusion.

In section 4.1, we will show that the contribution of mechanical-to-chemical (MC) coupling to diffusion driving forces is very significant compared with the contribution of purely chemical driving forces and, there, cannot be neglected. In section 4.2, we will discuss the fundamental difference in terms of of MC coupling between the linear elastic case and the nonlinear plastic case. Zero host diffusivity is assumed in sections 4.1 and 4.2 for simplicity; the effect of small but finite host diffusivity is discussed in section 4.3.

Discussions in this chapter are based on the work published in refs. [43], [44], and [18], with a focus on the Li/Si material.

4.1. The effect of stress-enhanced diffusion

Questions arise when it comes to the relative importance of the stress-free part μ_{SF}^{Li} and the stress-induced shift $-\Omega^{Li(SF)}\sigma_m$ in terms of their contributions to the Li flux [cf. Eqn. (2-38)]. It has been shown in chapter 3 that, to incorporate $J_K^{Li,mech}$ into the diffusion model, the stress gradient $\nabla_{\mathbf{X}}\sigma_m$ is needed, and considerable effort is required to numerically capture $\nabla_{\mathbf{X}}\sigma_m$ in a finite element (FE) framework. If the contribution to flux due to $-\Omega^{Li(SF)}\sigma_m$ is much smaller than that due to μ_{SF}^{Li}, it might be economical and prudent to neglect the stress-induced chemical potential shift and, hence, the mechanical-to-chemical coupling altogether.

In this section, however, we will show that the contribution of mechanical-to-chemical coupling (MC) to diffusion driving forces is very significant compared with the contribution of purely chemical driving forces and, therefore, cannot be neglected. We will also show that the overall effect due to the MC coupling is an enhancement to diffusion, as long as the stress is below the yield threshold. The discussion in this section is based on the work published in [43].

4.1.1. Linear perturbation relative to stress-free state

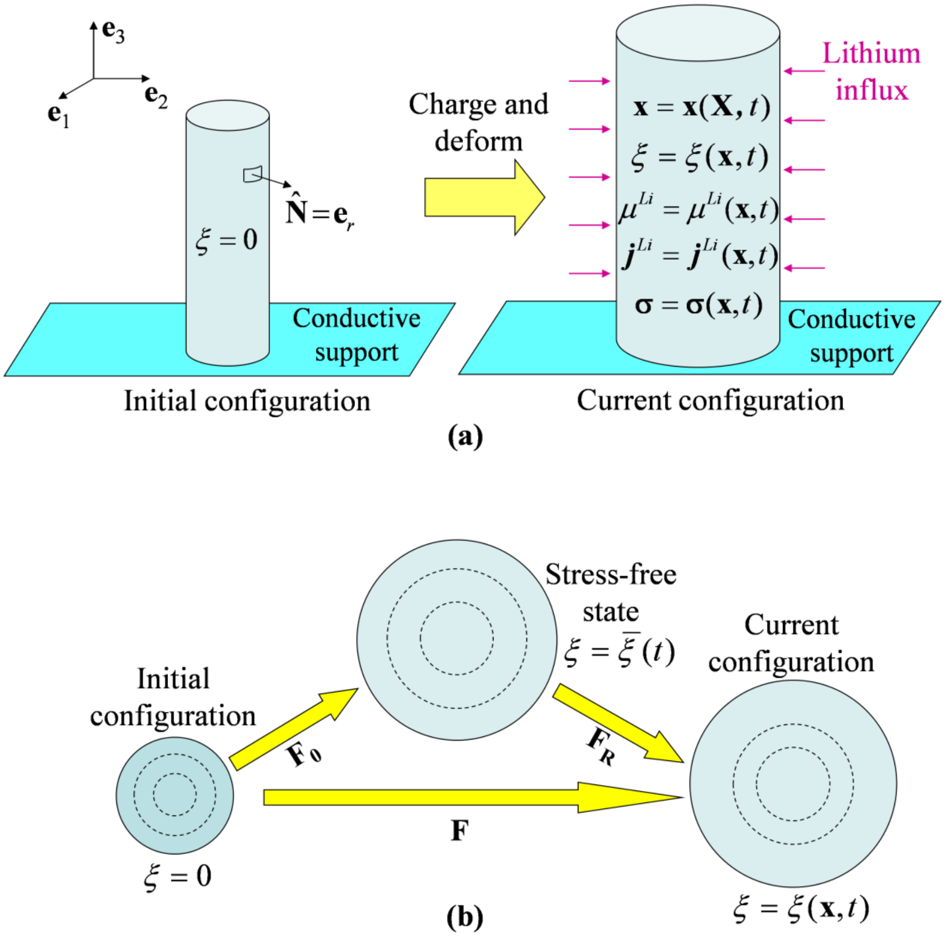

Fig. 4.1 (a) Galvanostatic charging and finite deformation of initially pure Si host nanowire; (b) Imaginary stress-free configuration.

To analyze the large deformation of $Li_{\xi}Si$ during Li insertion, we assume that the host atoms (Si) undergo only convection but negligible diffusion when the problem is treated in a Lagrangian frame fixed on the host. This is the case for carbon in LiC_6, as the carbon atoms form a scaffold through which small Li ions diffuse. It is also a reasonable first order approximation for $Li_{\xi}Si$ because the diffusivity of Si is much smaller than that of Li. The implication of finite host diffusivity will be the topic of section 4.3.

As illustrated in Fig. 4.1 (a), the electrode analyzed is a free-standing cylindrical NW made of pure a-Si (Li$_\xi$Si with $\xi(r,t)\big|_{t=0}=0$) with initial radius ρ_0. The mechanical constraint near the junction between the NW and the conductive support is neglected because the aspect ratio of the NW is assumed to be very large. Under galvanostatic conditions, the Lagrangian surface influx is constant, i.e.,

$$J_s = -\mathbf{e}_r \cdot \boldsymbol{J}^{Li} = \frac{1}{2}\rho_0 C^{Si}\xi_{\max}\frac{1}{T_0}, \tag{4-1}$$

where $\xi_{\max}$ is the charging limit of Li$_\xi$Si, T_0 is the total time required to attain full charge, and $\mathbf{e}_r$ is the base vector in the radial direction in a cylindrical coordinate frame and is equal to the unit surface normal $\hat{\mathbf{N}}$. The volume average lithium concentration in the NW at time t is $\bar{\xi}(t)=\xi_{\max}t/T_0$.

Lithium flux in the updated Lagrangian frame is determined by Fick's law [cf. the reference configuration counterpart of Eqn. (2-29)] as

$$j_k^{Li} = -\frac{D^{Li}}{k_B\theta}c^{Li}\frac{\partial \mu^{Li}}{\partial x_k}, \tag{4-2}$$

where D^{Li} is the lithium diffusion coefficient of in Li$_\xi$Si, k_B is the Boltzmann constant and θ is temperature which is taken to be a constant ($\theta = 300\,\mathrm{K}$). Assuming small $\boldsymbol{\varepsilon}^e$, the chemical potential for lithium [cf. Eqn. (2-38)] can be simplified into

$$\begin{aligned}\mu^{Li} &= \mu_*^{Li} + k_B\theta \ln \gamma^{Li} x^{Li} - \Omega^{Li(SF)}\sigma_m \\ &= \mu_*^{Li} + k_B\theta \ln \gamma^{Li} x^{Li} - \frac{\eta}{C^{Si}}\sigma_m .\end{aligned} \tag{4-3}$$

Here, we have used the linear relation $J^{SF}(\xi) = 1 + \eta\xi$ which is a good description according to findings of Chevrier and Dahn [106]; the expansion coefficient η and the partial atomic volume of Li ($\Omega^{Li(SF)}$) are related via $\Omega^{Li(SF)} = \eta / C^{Si}$.

When the wire radius is at the nanometer scale, bulk stress could be affected by surface energy and surface stress [20, 31]. In particular, for an infinitely long wire the contribution of the surface stress of $\boldsymbol{\sigma}^{surf} = \sigma_\theta^{surf}\mathbf{e}_\theta \otimes \mathbf{e}_\theta + \sigma_z^{surf}\mathbf{e}_z \otimes \mathbf{e}_z$ to the bulk stress is:

$$\boldsymbol{\sigma}^0 = -\frac{\sigma_\theta^{surf}}{\rho}\mathbf{e}_r \otimes \mathbf{e}_r - \frac{\sigma_\theta^{surf}}{\rho}\mathbf{e}_\theta \otimes \mathbf{e}_\theta - \frac{2\sigma_z^{surf}}{\rho}\mathbf{e}_z \otimes \mathbf{e}_z , \tag{4-4}$$

where ρ is the wire radius in the current configuration. Due to its homogeneous nature, $\boldsymbol{\sigma}^0$ does not affect the diffusion flux per Eqs. (4-2) and (4-3).

We base our analysis on the large deformation theory of chapter 2, but linearize the equations by using a perturbation method in order to obtain analytical solutions for short-time (low concentrations) and long-term (high concentrations) responses. To this end, a homogeneously charged state with $\xi = \bar{\xi}$, zero Cauchy stress ($\boldsymbol{\sigma} = \mathbf{0}$) and uniform deformation gradient $\mathbf{F}_0 = \left[J^{SF}(\bar{\xi})\right]^{1/3}\mathbf{I}$ is taken as an imaginary Lagrangian state from which perturbations are made [cf. Fig. 4.1 (b)]. The underlying assumption is that the ξ field in the NW deviates slightly from the averaged, homogeneous, and stress-free state. If the variation of concentration

$\Delta\xi \equiv \xi - \bar{\xi}$ is small across the NW, the relative deformation gradient $\mathbf{F}_\mathrm{R} \equiv \mathbf{F} \cdot \mathbf{F}_0^{-1}$ between the imaginary configuration represented by $\mathbf{F}_0$ and the true current configuration whose deformation gradient is $\mathbf{F}$ should be small. Therefore, $\mathbf{F}$ is regarded as a perturbation around $\mathbf{F}_0$ due to $\Delta\xi$. All field quantities can be conveniently referred to $\mathbf{F}_0$ as a first order approximation to their updated Lagrangian representations relative to the true current configuration. The finite deformation constitutive relation of Eqn. (2-36) can be linearized as

$$\boldsymbol{\varepsilon} = \frac{1+\nu}{E}\boldsymbol{\sigma} - \frac{\nu}{E} tr(\boldsymbol{\sigma})\mathbf{I} + \frac{1}{3}\frac{\eta}{J^{\boldsymbol{SF}}(\bar{\xi})}\Delta\xi\mathbf{I}, \tag{4-5}$$

where $\boldsymbol{\varepsilon} \equiv \left(\mathbf{F}_\mathrm{R}^\mathrm{T} \cdot \mathbf{F}_\mathrm{R} - \mathbf{I}\right)/2$ is the Lagrangian strain relative to the uniformly expanded, stress-free configuration, $E = E(\bar{\xi})$ is the concentration-dependent Young's modulus and $\nu = \nu(\bar{\xi})$ is the Poisson's ratio. In fact, given $\Delta\xi(r,t) = \xi - \bar{\xi}$, the stress profiles follow the classical solution in thermo-elasticity [107], i.e.,

$$\begin{cases} \sigma_z = -\dfrac{1}{3}\dfrac{1}{J^{\boldsymbol{SF}}(\bar{\xi})}\dfrac{dJ^{\boldsymbol{SF}}}{d\xi}\dfrac{E}{1-\nu}\cdot\Delta\xi - \dfrac{2\sigma_z^{surf}}{\rho}, \\ \sigma_\theta = \dfrac{1}{3}\dfrac{1}{J^{\boldsymbol{SF}}(\bar{\xi})}\dfrac{dJ^{\boldsymbol{SF}}}{d\xi}\dfrac{E}{1-\nu}\left(-\Delta\xi + \dfrac{1}{\tilde{r}^2}\displaystyle\int_0^{\tilde{r}}\tilde{r}\Delta\xi d\tilde{r}\right) - \dfrac{\sigma_\theta^{surf}}{\rho}, \text{ and} \\ \sigma_r = -\dfrac{1}{3}\dfrac{1}{J^{\boldsymbol{SF}}(\bar{\xi})}\dfrac{dJ^{\boldsymbol{SF}}}{d\xi}\dfrac{E}{1-\nu}\dfrac{1}{\tilde{r}^2}\displaystyle\int_0^{\tilde{r}}\tilde{r}\Delta\xi d\tilde{r} - \dfrac{\sigma_\theta^{surf}}{\rho}, \end{cases} \tag{4-6}$$

where $\tilde{r} \equiv r/\rho$ is the dimensionless spatial coordinate; $\rho = \rho(t) \approx \left[J^{\boldsymbol{SF}}\left(\bar{\xi}\right)\right]^{1/3} \rho_0$ can be approximated by the radius of the nanowire in the uniformly expanded configuration $\mathbf{F}_0$. The surface stress effect is included in Eq. (4-6).

The cylindrical symmetry of the NW dictates that $\boldsymbol{j}^{Li} = j_r^{Li}\mathbf{e}_r$. Equations (2-3), (4-2), (4-3) and (4-6) combine to give

$$\tilde{j}_r^{Li} = -\left(\frac{\Phi^{Li}\left(\bar{\xi}\right)}{1+\bar{\xi}} + \xi \tilde{D}_{stress}^{Li}\right)\frac{\partial \xi}{\partial \tilde{r}} \approx -\left(\frac{\Phi^{Li}\left(\bar{\xi}\right)}{1+\bar{\xi}} + \bar{\xi} \tilde{D}_{stress}^{Li}\right)\frac{\partial \xi}{\partial \tilde{r}} \;, \tag{4-7}$$

where $\tilde{j}_r^{Li} \equiv \rho J^{SF}\left(\bar{\xi}\right) j_r^{Li} / D^{Li} C^{Si}$ is the dimensionless flux in the updated Lagrangian configuration, $\tilde{D}_{stress}^{Li} \equiv \frac{1}{k_B \theta}\frac{2E\eta^2}{9(1-\nu)}\frac{1}{J^{\boldsymbol{SF}}\left(\bar{\xi}\right)}\frac{1}{C^{Si}}$ is the dimensionless effective diffusivity accounting for the contribution of stress to diffusion, and $\Phi^{Li}\left(\xi\right)$ is the stress-free thermodynamic factor [cf. Eqn. (2-41)]. Φ^{Li} can be determined by the open-circuit potential (OCP) U^{OCP} of a stress-free Li/Si anode vs. lithium metal through

$$\Phi^{Li} = -\left(e/k_B\theta\right)\xi\left(1+\xi\right)dU^{OCP}/d\xi, \tag{4-8}$$

where e is the charge of a single electron. The approximation in Eq. (4-7) is due to the fact that $\Delta\xi = \xi - \bar{\xi}$ is assumed to be small. The accuracy of this approximation is confirmed by separate numerical calculations.

Conservation of mass [Eqn. (2-4)] requires that $\partial c^{Li}/\partial t = -\left(1/r\right)\partial\left(r\, j_r^{Li}\right)/\partial r$. Therefore,

$$\frac{\partial \xi}{\partial t} = \frac{D_{eff}^{Li}}{\rho^2}\frac{1}{\tilde{r}}\frac{\partial}{\partial \tilde{r}}\left(\tilde{r}\frac{\partial \xi}{\partial \tilde{r}}\right), \text{ for } \tilde{r} \le 1, \tag{4-9}$$

where

$$\begin{aligned} D_{eff}^{Li} &\equiv D^{Li}\left[\Phi^{Li}\left(\bar{\xi}\right)/\left(1+\bar{\xi}\right)+\bar{\xi}\,\tilde{D}_{stress}^{Li}\right] \\ &= D^{Li}\frac{\Phi^{Li}}{1+\bar{\xi}}+\frac{D^{Li}}{k_B\theta}\frac{2E\left(\Omega^{Li(SF)}\right)^2}{9\left(1-\nu\right)}\frac{\bar{\xi}C^{Si}}{\det\left(\mathbf{F}^{SF}\right)} \end{aligned} \tag{4-10}$$

is the effective diffusivity. The boundary condition implied in (2-3) and (4-1) is

$$\tilde{j}_r^{Li} = -\frac{1}{2}\frac{\rho^2}{D^{Li}}\frac{\xi_{\max}}{T_0}, \text{ at } \tilde{r} = 1. \tag{4-11}$$

The transient solution to Eq. (4-9) under the condition of Eq. (4-11) is

$$\Delta\xi = \xi - \bar{\xi} = 2\sum_{n=1}^{\infty}\left[\frac{J_0\left(\lambda_n \tilde{r}\right)}{J_0\left(\lambda_n\right)}\int_0^{\tilde{\tau}} e^{-\lambda_n^2\tau}\,\tilde{j}_s\left(\tilde{\tau}-\tau\right)d\tau\right], \tag{4-12}$$

where $\tilde{\tau} = \tilde{\tau}\left(t\right) \equiv \int_0^t D_{eff}^{Li}/\rho^2 dt$ and $\tilde{j}_s \equiv \rho^2\xi_{\max}/2D_{eff}^{Li}T_0$. $J_0\left(\tilde{r}\right)$ is zeroth-order Bessel function of the first kind; λ_n is the n$^{\text{th}}$ root of the first-order Bessel function, i.e. $J_1\left(\lambda_n\right)=0$. Due to the exponential terms of $\exp\left(-\lambda_n^2\tau\right)$, the transient solution would asymptotically approach its long-term behavior when $t \gg t_0$, where $t_0 \equiv \rho_0^2/\lambda_1^2 D^{Li}$ is the characteristic time for diffusion in the

NW. To be specific, it is expected that $\partial\xi/\partial t \approx \partial\bar{\xi}/\partial t = \xi_{\max}/T_0$, which leads to the long-term solution of

$$\xi = \xi_{\max}\frac{t}{T_0} + \frac{1}{4}\frac{\rho^2}{D_{eff}^{Li}}\frac{\xi_{\max}}{T_0}\left(\tilde{r}^2 - \frac{1}{2}\right). \tag{4-13}$$

4.1.2. Results and discussions

Fig. 4.2 shows the short-term concentration and stress profiles for a Li$_\xi$Si NW with an initial diameter of 100 nm at a charging rate of 1C (full charge to $\xi_{\max}$ in 1 hour). Relevant material parameters are $\xi_{\max} = 4.4$ [7], $C^{Si} = 49.3$ atoms/nm^3 (pure amorphous Si with mass density ρ^{Si} =2.30 g/cm^3) [108], $\eta = 0.707$ (from $\eta\xi_{\max} = 3.11$ [12]), and $D^{Li} = 10^{-12}$ cm^{2}s^{-1} [109]. The concentration-dependent elastic properties are $E = E\left(\bar{\xi}\right) = (18.90\bar{\xi} + 90.13)/(1+\bar{\xi})$ GPa and $\nu = \nu\left(\bar{\xi}\right) = (0.24\bar{\xi} + 0.28)/(1+\bar{\xi})$ [77]. $\Phi^{Li} = 1$ is assumed for the dilute regime. To the best of the authors' knowledge, accurate surface stress data for Li$_\xi$Si is not currently available. An estimate through surface energy γ based on Kelly's approximation suggests that $\sigma_\theta^{surf} \approx \sigma_z^{surf} \sim \gamma \sim Ea_0/10$ [31, 110], with a_0 being the equilibrium separation between two atomic planes. A typical value of γ is around 1 J/m^2, which leads to $\sigma_r^0 = \sigma_\theta^0 \sim -\frac{\gamma}{\rho_0} = -20$ MPa and $\sigma_z^0 \sim -\frac{2\gamma}{\rho_0} = -40$ MPa for $\rho_0 = 50$ nm. Since the stress contribution due to surfaces $\boldsymbol{\sigma}^0$ is compressive, the surface effect reduces tensile stresses during cycling. As pointed out by Cheng et al. [32], this reduction in tensile stress may be partly responsible for the enhanced resistance to fracture and decrepitation of nanosized electrodes. To avoid the uncertainty associated with the value for γ and focus on the SED mechanism, only DIS due to concentration inhomogeneity $\boldsymbol{\sigma}^{DIS} \equiv \boldsymbol{\sigma} - \boldsymbol{\sigma}^{0}$ instead of the total stress $\boldsymbol{\sigma}$ is plotted here. Since $\boldsymbol{\sigma}^{0}$ is homogeneous throughout the wire [cf. Eq. (4-4)], the total stress $\boldsymbol{\sigma}$ can be readily obtained by shifting the $\boldsymbol{\sigma}^{DIS}$ curves. What is important here is to realize that $\boldsymbol{\sigma}^{0}$ has no bearing on diffusion.

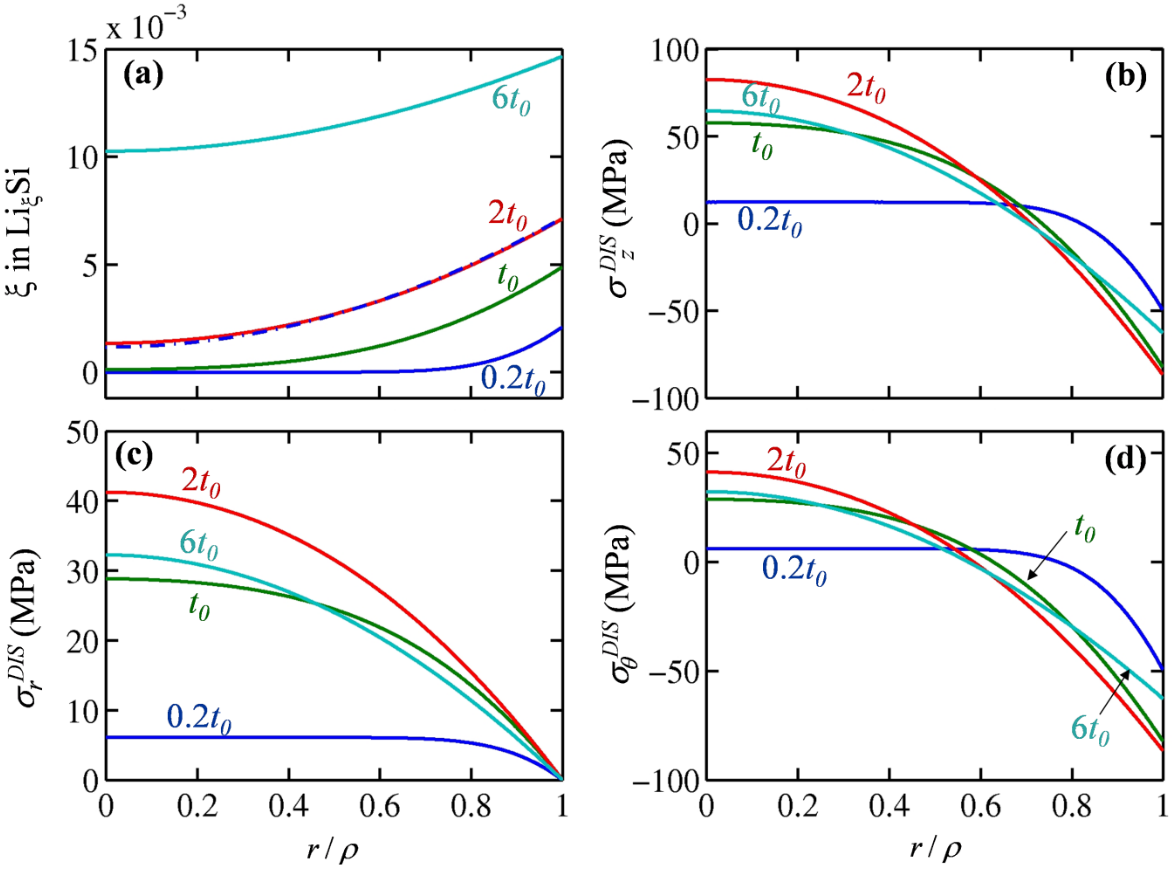

Fig. 4.2 Short-term response of a Li$_{\xi}$Si NW during the initial stages of a galvanostatic charge, (a) evolution of concentration distribution – the short-term solution (solid lines) quickly approaches the long-term solution (dotted line) by $2t_0$, *(b)-(d)* $\boldsymbol{\sigma}^{DIS} = \boldsymbol{\sigma} - \boldsymbol{\sigma}^{0}$ *profiles. The NW diameter is 100 nm and the charging rate is 1C.*

The first observation from Fig. 4.2(a) is that the variation in $\Delta\xi$ across the NW cross section is indeed small ($\left|\Delta\xi\right| \sim 5\times10^{-3}$), validating the assumption made at the beginning. The smallness of $\left|\Delta\xi\right|$ is also confirmed by the mixed-form full-coupling FEM simulation. The short-term profiles for ξ approach quickly the long-term profile [Eq. (4-13)] after $2t_0$, where $t_0 = \rho_0^2/\lambda_1^2 D^{Li} = 1.7\ \mathrm{s}$ is the characteristic time for diffusion for the wire at hand. Initially, $\Delta\xi = \xi - \bar{\xi}$ increases with time, but starts to decrease as the stress effect kicks in via $\bar{\xi}\tilde{D}_{stress}^{Li}$ in D_{eff}^{Li}. Since $\tilde{D}_{stress}^{Li}$ is always positive, the stress effect always increases the effective diffusivity D_{eff}^{Li} and thus enhances diffusion. The enhancement becomes more significant as $\bar{\xi}$ increases. The result is that the stresses first increase and then decrease as $\Delta\xi$ builds up and then decreases. As illustrated in Fig. 4.2(b-d), the stresses are lower at $6t_0$ than at $2t_0$.

Fig. 4.3 shows the evolution of stresses at the NW surface and center, where the stress levels of $\boldsymbol{\sigma}^{DIS}$ are at their corresponding extreme values. Since $\frac{1}{\tilde{r}^2}\int_0^{\tilde{r}} \tilde{r}\Delta\xi d\tilde{r} = 0$ at $\tilde{r} = 1$ (surface) and $\lim_{\tilde{r}\to 0}\frac{1}{\tilde{r}^2}\int_0^{\tilde{r}} \tilde{r}\Delta\xi d\tilde{r} = \Delta\xi/2$ (center), Eq. (4-6) simplifies into

$$\begin{cases} \sigma_\theta^{DIS} = \sigma_z^{DIS} = -\frac{1}{3}\frac{1}{J^{\boldsymbol{SF}}\left(\bar{\xi}\right)}\frac{dJ^{\boldsymbol{SF}}}{d\xi}\frac{E}{1-\nu}\cdot\Delta\xi \text{ and } \sigma_r^{DIS} = 0, \text{at } r \quad \uparrow\rho, \text{ and} \\ \sigma_z^{DIS} = -\frac{1}{3}\frac{1}{J^{\boldsymbol{SF}}\left(\bar{\xi}\right)}\frac{dJ^{\boldsymbol{SF}}}{d\xi}\frac{E}{1-\nu}\cdot\Delta\xi \text{ and } \sigma_\theta^{DIS} = \sigma_r^{DIS} = \frac{\sigma_z^{DIS}}{2}, \text{at } r = 0. \end{cases} \tag{4-14}$$

After a quick initial increase, $\boldsymbol{\sigma}^{DIS}$ at the surface levels off and reaches a maximum at $t \approx 2t_0$ as illustrated in Fig. 4.3(a). The evolution of $\boldsymbol{\sigma}^{DIS}$ at the NW center lags due to the time needed for concentration to propagate from surface to center. The subsequent decrease of the stresses at both the surface and center (and throughout the NW) after the full development of $\Delta\xi$ is due to the effect of SED through the term $\bar{\xi}\tilde{D}^{Li}_{stress}$ in D^{Li}_{eff}. A close look at Eqns. (4-6), (4-12) and (4-14) also reveals that the maximum DIS at the center and surface approximately scale with $\rho_0^2 / D^{Li} T_0$.

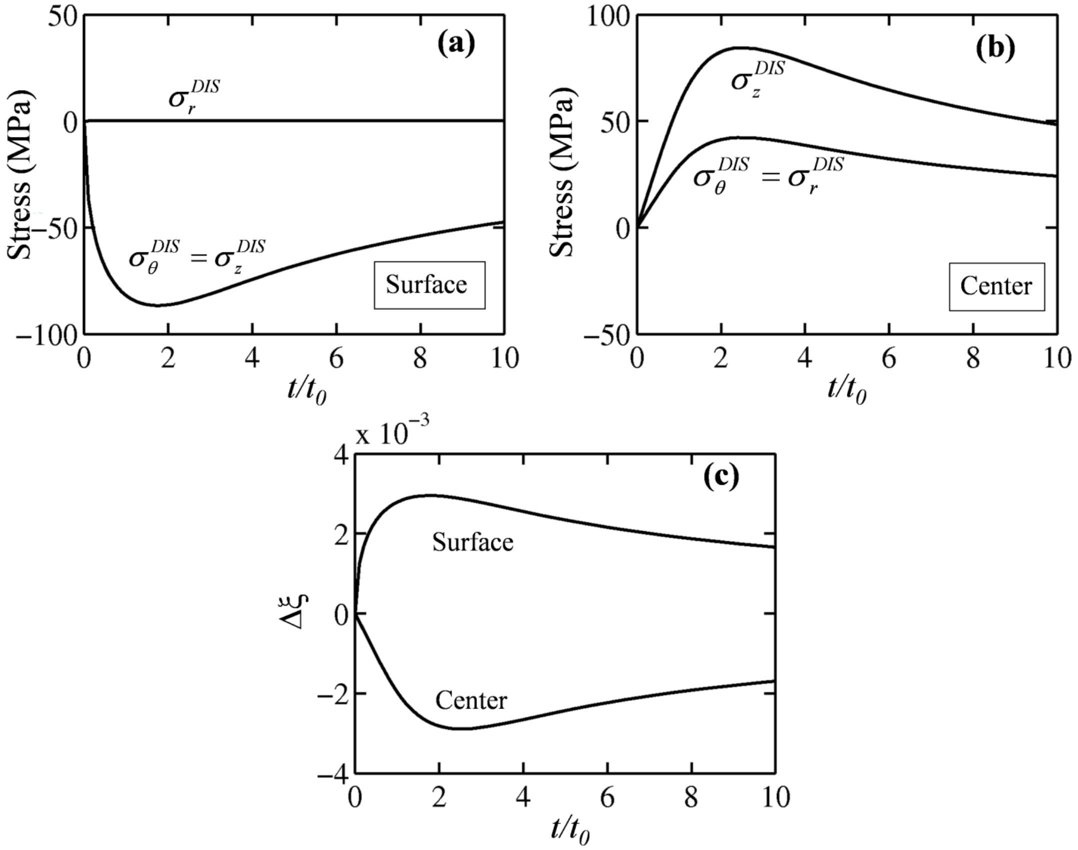

Fig. 4.3 (a) and (b): Stress evolution at the NW surface and center. (c): $\Delta\xi = \xi - \bar{\xi}$ at the NW surface and center. t_0 is the characteristic time for diffusion in the NW. The NW diameter is 100 nm and the charging rate is 1C.

Fig. 4.4 shows the long-term concentration and stress profiles for the same $\mathrm{Li}_\xi\mathrm{Si}$ NW under the same charging rate as in Fig. 4.3 at a state of charge (SOC) of $\xi/\xi_{\max}=0.5$. Ding's experiments [109] suggest that $dU^{OCP}/d\xi\approx-0.1\,\mathrm{eV}$ at $\xi=0.5\xi_{\max}=2.2$, leading to $\Phi^{Li}\left(\bar{\xi}\right)=27.2$. Again, the variation of $\Delta\xi$ across the NW cross section is small, validating the assumption made at the beginning. To reveal the significance of SED at this intermediate SOC, both solutions with and without $\tilde{D}_{stress}^{Li}$ in $D_{eff}^{Li}\equiv D^{Li}\left[\Phi^{Li}\left(\bar{\xi}\right)/\left(1+\bar{\xi}\right)+\bar{\xi}\tilde{D}_{stress}^{Li}\right]$ are shown. Obviously, the SED effect significantly enhances the diffusion process, making ξ much more uniform. This effect amounts to an increase of $\bar{\xi}\tilde{D}_{stress}^{Li}/\left[\Phi^{Li}/\left(1+\bar{\xi}\right)\right]=303\%$ in the effective diffusivity of lithium. The long-term DIS profiles in Fig. 4.4(b) offer insight as well. The radial stress σ_r^{DIS} is tensile throughout the wire. On the other hand, the axial stress σ_z^{DIS} and the hoop stress σ_θ^{DIS} are tensile in the core and compressive near the surface. The hydrostatic part of $\boldsymbol{\sigma}^{DIS}$ is only ~2 MPa in a thin wire with d = 100 nm under a moderate charging rate of 1C. Nevertheless, such a low DIS level contributes significantly to the overall driving force for diffusion as seen in Fig. 4.4(a).

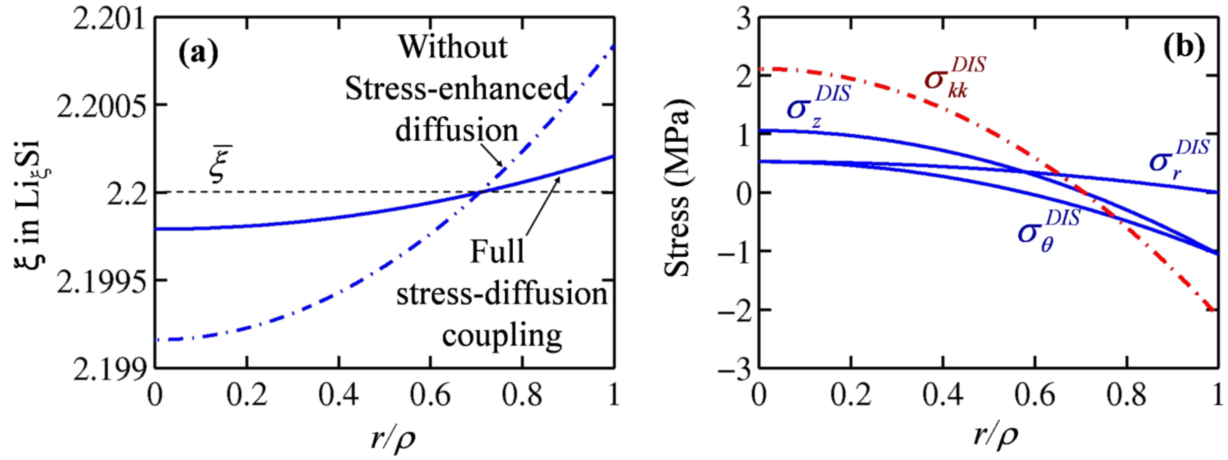

Fig. 4.4 Long-term solution for a Li$_\xi$Si NW when charged to a SOC of $\bar{\xi} = 0.5\xi_{\max} = 2.2$, (a) concentration and (b) stress. The NW diameter is 100 nm and the charging rate is 1C.

Equations (4-13) and (4-6) show that the long-term DIS $\boldsymbol{\sigma}^{DIS} \propto \Delta\xi \propto \rho^2 / D_{eff}^{Li} T_0$. Thus, the long-term stresses also increase quadratically with the wire radius and are inversely related to the charging rate and the diffusivity. These scaling relations are consistent with previous findings of Christenensen et al. [88] for LiC_6 and Zhang et al. [99] for $LiMn_2O_4$. What is different here is the strong modulation of the effective diffusivity by $\bar{\xi}\tilde{D}_{stress}^{Li}$ in the case of Li$_\xi$Si. Zhang et al. discussed the effect of SED of Li in Mn_2O_4 crystalline cathodes and showed that the difference in concentration inhomogeneity $\max(\Delta\xi) = \xi(\rho) - \bar{\xi}$ with and without the SED effect is ~13% [99]; for LiC_6 the difference is ~20% [88]. Here, however, the difference is 303%. The enhancement due to stress in Li$_\xi$Si is much more pronounced for two reasons. First, the partial atomic volume $\Omega^{Li(SF)}$ of lithium in Li$_\xi$Si is 14.3 Å^3, much larger than the partial atomic volume of Li in Mn_2O_4 ($\Omega^{Li(SF)} = 5.8$ Å^3 per Li [99]). The lower amount of open space in the alloy electrodes compared with that in intercalation lattices gives rise to the stronger SED effect seen in Fig. 4.4. Second, Li$_\xi$Si can be charged to a much higher Li concentration limit than cathode lattices and the contribution of stress to effective diffusivity ($\bar{\xi}\tilde{D}^{Li}_{stress}$) is proportional to the average concentration $\bar{\xi}$.

It should be noted that the change of D^{Li} with stress is not considered in this study. Haftbaradaran et al. [19] considered the activation barrier shift ΔE_b for diffusion due to DIS and showed that the stress effect could slow down diffusion through $D^{Li} = D_0^{Li} \exp\left(-\Delta E_b / k_B \theta\right)$. While stress-induced activation barrier change ΔE_b is more important under very high stresses, stress development and diffusion mainly couple through the chemical potential for moderate stresses [111] which is the regime we consider in this section. There might be a transition threshold below which stress enhances diffusion and above which stress hinders diffusion. Following Haftbaradaran et al. [19], we take $\alpha = 0.3$ for $\Delta E_b = -\alpha\Omega\sigma_b$ where σ_b is the bi-axial surface stress. This leads to $\left|\Delta E_b / k_B \theta\right| \approx 1$ only when $\left|\sigma_b\right|$ reaches as high as 1 GPa, otherwise, the factor $\exp\left(-\Delta E_b / k_B \theta\right)$ is negligible. Therefore, if a transition threshold exists, it must be very high, even higher than the yield stress for onset of plasticity [15].

The levels of $\boldsymbol{\sigma}^{DIS}$ at the lower concentrations in Fig. 4.2 and Fig. 4.3 are as much as ~100 times those at the higher concentrations in Fig. 4.4. To understand this significant change in stress levels, note that $\Phi^{Li}\left(\bar{\xi}\right)/\left(1+\bar{\xi}\right) = 8.5$ and $\bar{\xi}\tilde{D}^{Li}_{stress} = 25.8$ at $t = T_0/2$ ($\bar{\xi} = 2.2$) and $\Phi^{Li}\left(\bar{\xi}\right)/\left(1+\bar{\xi}\right) \approx 1$ and $\bar{\xi}\tilde{D}^{Li}_{stress} = 0.14$ at $t = 2t_0$ ($\bar{\xi} = 2.1\times10^{-3}$) for Li$_\xi$Si. Also contributing to this is the fact that the material is softer (as measured by the elastic modulus) at higher lithium concentrations [77]. The thermodynamic factor enhancement, SED and the softening of material lead to lower stress levels at higher Li concentrations. In this process, the SED effect is the dominant factor and the most important. It should be noted that experimentally measured $U^{OCP}\left(\xi\right)$ curves for Li$_\xi$Si are associated with significant hysteresis [70] which makes accurate estimates of the quasi-equilibrium value of $dU^{OCP}/d\xi$ difficult. This lack of accuracy in determining the value of $dU^{OCP}/d\xi$ should not be construed as to obscure the importance of SED in the intermediate composition range. For example, even if $\left|dU^{OCP}/d\xi\right| = 0.15\,\mathrm{eV}$, $\Phi^{Li}\left(\bar{\xi}\right)/\left(1+\bar{\xi}\right) = 12.8$ and $\bar{\xi}\tilde{D}^{Li}_{stress}/\left[\Phi^{Li}/\left(1+\bar{\xi}\right)\right] =$ 202%, a scenario in which SED still dominates.

If the NW radius is large or charging rate is high, the total stress $\boldsymbol{\sigma} = \boldsymbol{\sigma}^{DIS} + \boldsymbol{\sigma}^0$ could be high enough to cause material failure. The fact that the peak DIS levels scale with $\rho_0^2/D^{Li}T_0$ and the initial DIS levels are much higher than the long-term values suggests that lower charging rates should be used to prime a new Si anode or a Si anode after deep discharge in order to avoid mechanical failure during initial charging. The results obtained here also indicate that deep discharging would reduce the cyclability of Li$_\xi$Si anodes because of the higher DIS at low concentrations. The adverse effect is more pronounced if fast recharge is carried out subsequently.

4.1.3. Conclusions

In this section, we analyzed the development of DIS in amorphous Li$_\xi$Si alloy NW-based electrodes by using the finite deformation framework of chapter 2, and by accounting for full two-way diffusion-stress development coupling. Analytical solutions for concentration and stresses are obtained via linearization through a perturbation method. Significant contribution to diffusion by stress at high Li concentrations is shown for $Li_{\xi}Si$ electrodes. The contribution of stress to diffusion is small when Li concentration is low in early stages of a charging process, leading to high DIS levels. A rational charging regimen for Li ion batteries with new amorphous Si anodes should include priming with a charging rate significantly lower than the regular operational charging rate. The analysis also suggests that deep discharging should be avoided, especially when fast recharges are needed subsequently. The long-term DIS levels scale with nanowire radius, charging rate, and stress-modulated Li mobility in Si, reflecting the strong two-way coupling between diffusion and stress development, in contrast to what is the case for most intercalation electrodes. The scaling law suggests that designs that take advantage of the size effect, controlling of charging rate and enhancement of diffusion through alloying are all effective means for enhancing the reliability of $Li_{\xi}Si$ anodes.

The fact that the mechanical-to-chemical coupling, or the effect of SED, is much more pronounced in Li/Si than that in other intercalation materials is attributed to two reasons [43]. First, the partial atomic volume $\Omega^{Li(SF)}$ in Li/Si is much larger than those in $LiMn_2O_4$ and LiC_6 -- according to Eqn. (4-10) the MC contribution to the effective diffusivity (second term) is proportional to the square of $\Omega^{Li(SF)}$. Second, Li/Si can be charged to a much higher Li concentration limit than cathode lattices or carbon -- and the MC contribution to D_{eff}^{Li} is proportional to the average Li concentration $\bar{C}^{Li} = \bar{\xi} C^{Si}$. Therefore, the mechanical-to-chemical coupling in Li/Si has significant implications and cannot be neglected.

4.2. The effect of plasticity on two-way coupling

The analysis in section 4.1, along with the conclusion of strong stress-enhanced diffusion (SED), is based on the assumption that the deformation is elastic. Under this assumption, ∇C^{Li} and $-\nabla\sigma_m$ point to the same direction in a nanowire during lithiation and delithiation, and the effect of $-\nabla\sigma_m$ is an enhancement to the diffusive kinetics.

According to section 2.1.3, however, Li/Si is also capable of deforming plastically. As we will show in this section, the overall effect of MC (mechanical-to-chemical) coupling during plastic deformation is fundamentally different from that described in section 4.1.

To demonstrate this difference, we investigate the effect of external constraints on Li diffusion using the fully coupled, finite deformation framework of chapter 2. It is found that thin-film electrodes on rigid substrates suffer from much slower diffusion rates compared with free-standing films (or nano-flakes in some applications) with the same material properties and geometric dimensions. Of particular interest is the surprising finding that mechanical driving forces tend to retard diffusion in thin-film electrodes when lithiation-induced softening is considered. This is in sharp contrast to the fact that mechanical stresses always enhance diffusion when the deformation is in the elastic regime. The result provides further support for nano-particles as a better alternative to thin films as alloy-based electrode material. The discussion in this section is based on the work published in [44].

4.2.1. Model configurations and simplifying assumptions

We use the rate-form, large-deformation, mixed finite element framework (chapter 3) to analyze the two-way coupling between diffusion and stress development (chapter 2). The issues of focus are

1) how does the mechanical-to-chemical (MC) coupling affect the transport of Li under different mechanical constraints and

2) as an important figure of merit for batteries, how significantly does this difference affect the operational charging rate?

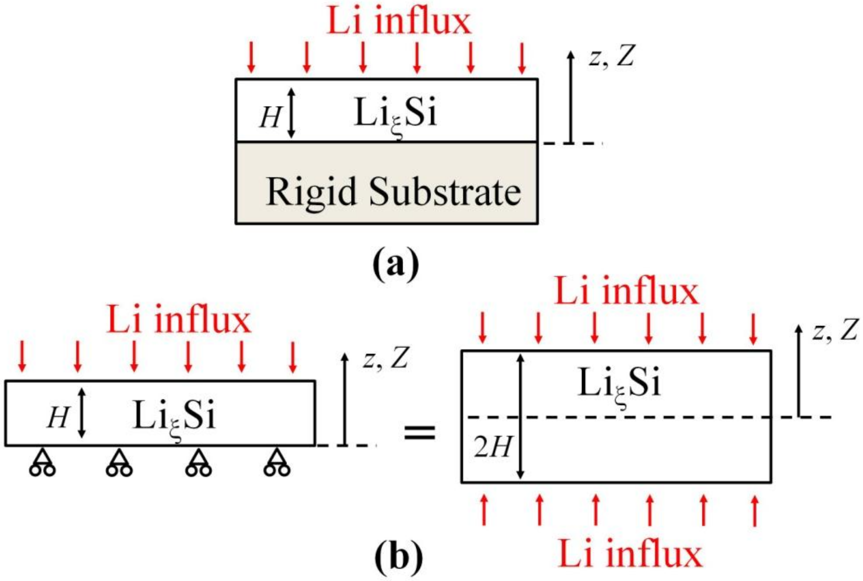

Fig. 4.5 The two configurations used to analyze how mechanical constraints affect Li transport. (a) Thin film with thickness H *perfectly bonded to a rigid substrate. A galvanostatic influx is prescribed on the top surface. (b) a thin film which is constrained only in the* z*-direction at the bottom (due to symmetry) with the same galvanostatic influx at the top face (left). This configuration is equivalent to a film with a thickness of 2*H *under symmetric influxes from both faces (right). The coordinate in the current configuration is denoted as z and the coordinate in the Lagrangian configuration is denoted as* Z*.*

To this end, we consider two simple electrode configurations with essentially the same material properties and geometric setup, but different mechanical constraints. The first configuration [Fig. 4.5 (a)] involves a thin film of $\mathrm{Li}_{\xi}\mathrm{Si}$ (host H=Si) with thickness *H* perfectly bonded to a substrate which has a stiffness much higher than that of the film and, therefore, can be treated as rigid. A constant influx of Li is specified at the top surface so that the electrode is charged under galvanostatic conditions. This surface influx is measured in the reference configuration as

$$J_{Surf}^{Li} = -J_{Z}^{Li}\left(Z = H\right) = \frac{H\xi_{\max}C^{Si}}{T_0}, \qquad (4\text{-}15)$$

where T_0 is the nominal time for achieving full charge. Here, we take $T_0 = 4$ hours (1/4 C charging).

The second configuration [Fig. 4.5 (b)] has the same thickness and influx, but the bottom surface is only constrained in the *z*-direction and is free to move in the other directions. This is equivalent to a film with a thickness of 2*H* and the same influx on both faces. Understandably, the two configurations will develop very different stresses due to the different constraints. Our goal is to analyze how $C^{Li}\left(Z,t\right)$ is distributed (Z denotes the Lagrangian coordinate) with two-way deformation-diffusion coupling under different mechanical constraints.

The material behavior is assumed to follow the constitutive laws delineated in chapter 2. To simplify the problem, $\mu_{SF}^{Li} = \mu_{SF}^{Li}\left(\xi\right)$ is not fitted from experimental OCP data (as we have done in section 4.1); instead, we adopt the ideal-solution form of μ_{SF}^{Li} originally proposed by Larche and Cahn [97] and subsequently used by Purkayastha and McMeeking [96] and Yang et al. [98] in the form of

$$\mu_{SF}^{Li} = \mu_*^{Li} + k\theta \ln \frac{\xi}{\xi_{\max} - \xi}, \tag{4-16}$$

where $\xi_{\max}$ is the maximum charging limit of the electrode material and the constant μ_*^{Li} is a reference chemical potential. The composition-dependent diffusivity $D^{Li} = D^{Li}\left(\xi\right)$, on the other hand, is taken to be [96, 98]

$$D^{Li} = D_0^{Li}\left(1 - \xi / \xi_{\max}\right) = D_0^{Li}\left(1 - C^{Li} / C_{\max}^{Li}\right). \tag{4-17}$$

Combining Eqs. (2-40), (4-16), and (4-17) leads to the lithium flux of

$$\begin{aligned} J_K^{Li} &= J_K^{Li,chem} + J_K^{Li,mech}, \text{ with} \\ J_K^{Li,chem} &= -D_0^{Li} f_{Ki} f_{Ji} \frac{\partial C^{Li}}{\partial X_J} \quad \text{and} \\ J_K^{Li,mech} &= \frac{D_0^{Li}\left(1 - C^{Li} / C_{\max}^{Li}\right)}{k_B \theta} f_{Ki} f_{Ji} C^{Li} \frac{\partial\left[\Omega^{Li(SF)} \sigma_m\right]}{\partial X_J}. \end{aligned} \tag{4-18}$$

In the above relations, $J_K^{Li,chem}$ and $J_K^{Li,mech}$ are contributions due to chemical interaction and mechanical driving force, respectively. According to Purkayastha and McMeeking [96], the main advantage of Eqs. (4-16) and (4-17) is that it correctly captures the fact that the stress-gradient-driven diffusion flux $J_K^{Li,mech}$ [cf. eqn. (4-18)] vanishes at the charging limits of $\xi = 0$ and $\xi = \xi_{\max}$.

The material properties used in this section are $\Omega^{\mathrm{Li\,(SF)}} = 14.3$ $\mathrm{\AA}^3$ [12, 43], $D_0^{Li} = 10^{-12}$ cm^{2}s^{-1}, $\xi_{\max} = 3.75$ and $C^{Si} = C_0^{Si} = 49.3$ atoms/nm^3. The temperature is taken to be 300 K. A calculation is first carried out with a composition-independent Young's modulus value of $E = 80$ GPa, Poisson's ratio value of $\nu = 0.22$ and yield stress value of $\sigma_Y = 1.75$ GPa. The corresponding bulk modulus K and shear modulus G are 47.62 GPa and 32.79 GPa, respectively. This calculation is used as the baseline case to study the effect of lithiation-induced softening on Li diffusion. The second calculation involves composition-dependent bulk modulus $K = (12.46\xi + 65.44)/(1+\xi)$ GPa, shear modulus of $G = (7.63\xi + 35.51)/(1+\xi)$ GPa [77], and yield stress of $\sigma_Y = \left(1.75 + 0.167\xi\right)/\left(1+\xi\right)$ GPa, allowing comparison with the baseline case to be made. The variation of yield stress with concentration represents a simple interpolation between $\sigma_Y = 1.75$ GPa at $\xi = 0$ and $\sigma_Y = 0.5$ GPa at $\xi = \xi_{\max}$ [15, 56] using the rule of mixture.

4.2.2. Stress-enhanced diffusion during elastic deformation (configuration b)

Fig. 4.6 shows the profiles of normalized lithium concentration ξ and the stresses in a film with a thickness of H=500 nm and constraint only in the z-direction at the bottom [configuration Fig. 4.5 (b)]. When $J_K^{Li,mech}$ is neglected, the concentration builds up in the early stages of charging [Fig. 4.6 (a)], accompanied by increases in the in-plane stresses [Fig. 4.6 (c)]. As stresses increase, the surface and center of the film reach the yield threshold and begin to flow plastically, leading to plateaus in the stress profiles at $t = 0.0125T_0 \sim 0.1T_0$. The time scale for this transient buildup of concentration is $\tau^{Li} \sim H^2/4D_0^{Li} \sim 6\times10^2$ s. Beyond τ^{Li}, the long-term profile of ξ continues to evolve, albeit slowly; however this evolution is no longer due to transient effects. In Fig. 4.6 (d), the concentration profiles that account for the effects of $J_K^{Li,mech}$ show similar behavior in early stages as those Fig. 4.6 (a), but reflect more uniform distribution of Li as time progresses. Also, the stress levels are much lower [Fig. 4.6 (f)] compared with the case without the effect of $J_K^{Li,mech}$ [Fig. 4.6 (c)]. In fact, the reduction in stresses is so significant that the yield threshold is never reached in Fig. 4.6 (f), as a result the deformation is fully within the elastic regime throughout the charging process. A simple analysis shows that when $J_K^{Li,mech}$ is considered, the diffusion is no-longer governed by D_0^{Li} itself. Instead, J_Z^{Li} is governed by an effective diffusivity $D^{Li,eff}$ such that (cf. section 4.1.1)

$$\left.\begin{aligned} & J_Z^{Li} = -D^{Li,eff} f_{Ki} f_{Ji} \frac{\partial C^{Li}}{\partial Z}, \text{ with} \\ & D^{Li,eff} \equiv D_0^{Li} + D^{Li,mech} \text{ and} \\ & D^{Li,mech} = \frac{C^{Li}\left(1 - C^{Li} / C_{\max}^{Li}\right)}{k_B \theta} \frac{\left(\Omega^{G(SF)}\right)^2}{J^{SF}} \frac{2E}{9(1-\nu)} D_0^{Li}. \end{aligned}\right\} \tag{4-19}$$

The form of Eqn. (4-19) is slightly different from Eqn. (4-10) mainly because of the different assumptions on $D^{Li} = D^{Li}(\xi)$ and $\mu_{SF}^{Li} = \mu_{SF}^{Li}(\xi)$ made here and made in section 4.1. Eqn. (4-19) is valid as long as the deformation is fully elastic. Here, the second term (i.e. $D^{Li,mech}$) in the expression of $D^{Li,eff}$ is always positive. It is due to the mechanical driving force for diffusion and is ~20 times larger than D_0^{Li} at $\xi / \xi_{\max} = 0.5$. This effect leads to much faster lithium transport due to the fact that stresses always try to “squeeze” Li from compressed regions into tensile regions, hence the name stress-enhanced diffusion (SED). It should be noted that classical theories of diffusion suggest an asymptotic shape of concentration profile which remains unchanged once $t \gg \tau^{Li}$. Here, however, the long-term shapes of the concentration and stress profiles continue to evolve even for $t \gg \tau^{Li}$. Two mechanisms are responsible. The first is associated with the fact that $D^{Li,eff} = D^{Li,eff}\left(C^{Li}\right)$ is concentration-dependent [cf. eqn. (4-19)]. Since $D^{Li,mech} \propto C^{Li}\left(1 - C^{Li}/C_{\max}^{Li}\right)$, SED is less pronounced when ξ is close 0 or $\xi_{\max}$. Therefore the concentration profiles are steeper at the end of charging process ($t = 0.952T_0$) than at $t = 0.1T_0$ in Fig. 4.6 (e). By the same token, the stresses are also higher at the end than at $t = 0.1T_0$. This first mechanism is relevant only for the situation when $J_K^{Li,mech}$ is considered. The second mechanism, which is relevant with or without $J_K^{Li,mech}$, is associated with the geometric non-linearity under finite deformations [Eqn. (4-27)]. This mechanism will be discussed later.

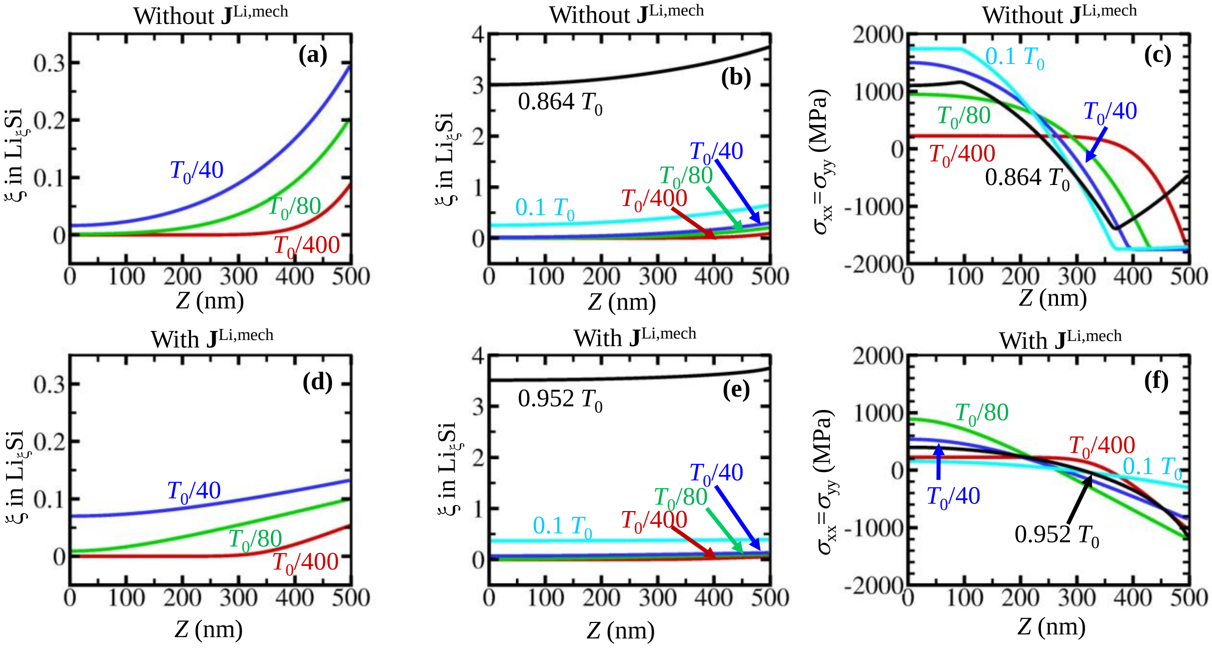

Fig. 4.6 Normalized Li concentration (a,b,d,e) and stress (c,f) profiles in a film with a thickness of H=500 nm and constraint only in the z-direction at the bottom [configuration in Fig. 4.5 (b)]. (a-c) normalized concentration and

stress profiles when the mechanical driving force for diffusion is not considered. (d-f) normalized concentration and stress profiles when the mechanical driving force for diffusion is considered. For clarity, (a) and (d) show, with a finer vertical axis scale, the three early-stage profiles in (b) and (e), respectively.

When $J_K^{Li,mech}$ is neglected, the Li concentration reaches its fully-charged limit of $\xi_{\max}$ on the surface at $t = 0.864 T_0$, rendering further galvanostatic charging practically impossible. In experiments, the charging condition is usually switched to potential-static at this point so that $\xi = \xi_{\max}$ is maintained on the surface while ξ in the interior further increases. This charging regimen is not considered in the simulations here. Instead, the simulations are stopped once the surface concentration ξ reaches $\xi_{\max}$ and the average Li concentration $\bar{\xi}_{end}$ in the electrode at that point is used for comparison. This average value is directly related to the actual change time t_{end} via $\bar{\xi}_{end} = \xi_{\max} \left(t_{end} / T_0 \right)$. Since the actual charging time t_{end} is always smaller than the nominal charging time T_0, $\bar{\xi}_{end}$ is always smaller than $\xi_{\max}$. Obviously, $\bar{\xi}_{end}$ depends on the charging rate which is controlled by J_{Surf}^{Li}. Higher charging rates lead to lower $\bar{\xi}_{end}$. To achieve the same $\bar{\xi}_{end}$ through slower Li transport, lower operational charging rate must be used. Calculations show that, for the material conditions analyzed under the nominal changing rate of $T_0 = 4$ h, $\bar{\xi}_{end} = 0.952 \xi_{\max}$ when $J_K^{Li,mech}$ is considered and, in contrast, $\bar{\xi}_{end} = 0.864 \xi_{\max}$ when $J_K^{Li,mech}$ is neglected. Clearly, the SED effect (stress contribution to diffusion) not only lowers stresses but also increases allowable operational charging rate through enhanced Li transport (and, therefore, more uniform Li distribution). This effect will be further analyzed later in the context of different mechanical constraints.

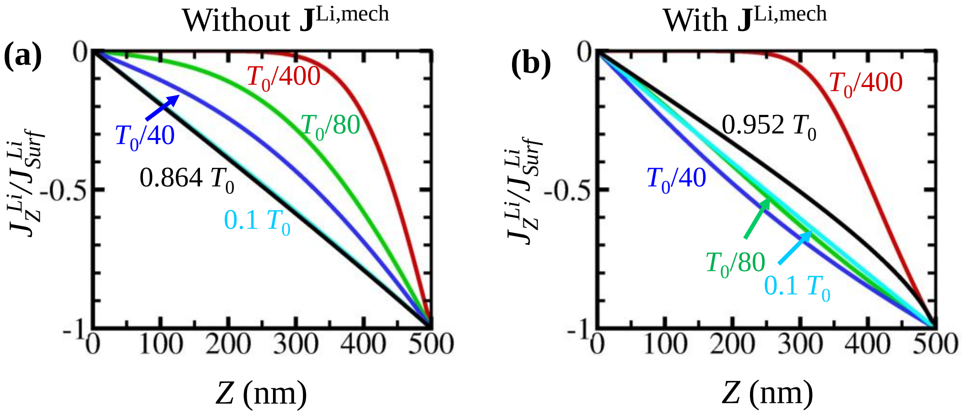

Fig. 4.7 Lagrangian lithium flux normalized by surface influx with (a) mechanical driving force not considered and (b) mechanical driving force considered. Z denotes Lagrangian coordinate. The film is constrained only in the z-direction at the bottom and lithiation-induced softening is not considered.

A look at the distribution of lithium fluxes also provides insights. Fig. 4.7 shows the Lagrangian lithium fluxes as normalized by the surface influx [Eq. (4-15)]. Only J_Z^{Li} is plotted because $J_X^{Li} = J_Y^{Li} = 0$ due to symmetry. For both the situations with and without the effect of $\mathbf{J}^{Li,mech}$, $J_Z^{Li} = -J_{Surf}^{Li}$ at the surface (Z=500 nm) and $J_Z^{Li} = 0$ at the center (Z=0 nm). Since the problem is 1-D here, the conservation of mass [Eqn. (2-4)] requires

$$J_Z^{Li}(Z) = J_Z^{Li}(Z=0) - \int_0^Z \frac{\partial C^{Li}}{\partial t} dZ = -C^{Si} \int_0^Z \frac{\partial \xi}{\partial t} dZ. \tag{4-20}$$

The normalized concentration $\xi \equiv C^{Li}/C^{Si}$ can be decomposed into two parts: the average Li-concentration part

$$\bar{\xi} \equiv \frac{1}{H} \int_0^H \xi dZ \tag{4-21}$$

and the inhomogeneity part

$$\Delta\xi \equiv \xi - \overline{\xi}. \tag{4-22}$$

By Eqs. (4-21), (4-20) and (4-15),

$$\overline{\xi} = \frac{t}{T_0}\xi_{\max}. \tag{4-23}$$

Therefore, Eqs. (4-20)-(4-23) require

$$J_Z^{Li}(Z) = -\frac{Z}{H}J_{Surf}^{Li} - C^{Si}\int_0^Z \frac{\partial\Delta\xi}{\partial t}dZ. \tag{4-24}$$

Since $\int_0^0 (\partial\Delta\xi/\partial t)dZ = \int_0^H (\partial\Delta\xi/\partial t)dZ = 0$, Eqn. (4-24) has a Taylor-expansion in the form of

$$J_Z^{Li}(Z,t) = -\frac{Z}{H}J_{Surf}^{Li} - \frac{Z}{H}\sum_{n=1}^{\infty}\left(1-\frac{Z}{H}\right)^n J_Z^{Li(n)}(t) \tag{4-25}$$

where the coefficients $J_Z^{Li(n)}(t)$ are directly related to the time rate $\partial\Delta\xi/\partial t$ of the concentration inhomogeneity.

For the case in which $\mathbf{J}^{Li,mech}$ is not considered [Fig. 4.7 (a)], $\partial\Delta\xi/\partial t = 0$ once the transient build-up of ξ has completed ($t > \tau^{Li}$). Consequently, $J_Z^{Li(n)}(t) = 0$ except for the initial transient stages, explaining why the $J_Z^{Li}\left(Z\right)$ profiles in Fig. 4.7 (a) are linear for $t = 0.1T_0$ and $0.864T_0$. For the case in which $\mathbf{J}^{Li,mech}$ is considered, the effective diffusivity $D^{Li,eff}$ [eqn. (4-19)] changes slowly even after the initial transient development finishes. This long-term modulation of $D^{Li,eff}$ leads to non-zero $\partial\Delta\xi / \partial t$ and hence non-zero $J_Z^{Li(n)}\left(t\right)$. As a result, the $J_Z^{Li}\left(Z\right)$ profiles at $t = 0.1T_0$ and $t = 0.952T_0$ deviate from the $J_Z^{Li} = -\left(Z/H\right)J_{Surf}^{Li}$ line, as seen in Fig. 4.7(b). Such a deviation is nevertheless fairly small and a first-order approximation of

$$J_Z^{Li} \approx -\frac{Z}{H} J_{Surf}^{Li} \tag{4-26}$$

can lead to some interesting observations. Specifically, when the thin film is constrained only in the *z*-direction [Fig. 4.5(b)], the deformation gradient is approximately (in the elastic regime $\mathbf{F}^p = \mathbf{I}$)

$$\mathbf{F} \approx \mathbf{F}^p\mathbf{F}^{SF} = \left(J^{SF}\right)^{1/3}\begin{pmatrix} 1 & 0 & 0 \\ 0 & 1 & 0 \\ 0 & 0 & 1 \end{pmatrix}. \tag{4-27}$$

Under this deformation, the concentration gradient $\partial\xi / \partial Z$ can be determined from Eqs. (4-18), (4-19) and (4-26) to be

$$\frac{\partial C^{Li}}{\partial Z} = C^{Si}\frac{\partial\xi}{\partial Z} \approx \frac{\left(J^{SF}\right)^{2/3}}{D^{Li,eff}}\frac{Z}{H} J_{Surf}^{Li}. \tag{4-28}$$

By the same token, $\partial\xi / \partial Z$ without the effect of $\mathbf{J}^{Li,mech}$ is governed by

$$\frac{\partial C^{Li}}{\partial Z} = C^{Si}\frac{\partial \xi}{\partial Z} \approx \frac{\left(J^{SF}\right)^{2/3}}{D_0^{Li}}\frac{Z}{H}J_{Surf}^{Li} . \tag{4-29}$$

Equations (4-28) and (4-29) show that the shapes of the long-term ξ profiles are approximately quadratic as long as the transient build-up stages have finished, regardless of whether $\mathbf{J}^{Li,mech}$ is considered or not. Moreover, when $\mathbf{J}^{Li,mech}$ is not accounted for, the diffusion is controlled by a constant diffusivity D_0^{Li}. Because J^{SF} is larger at higher ξ, the concentration inhomogeneity $\Delta\xi$ increases with *t* according to Eqn. (4-29). This is why the Li concentration profile is steeper at $t = 0.863T_0$ than at $t = 0.1T_0$ in Fig. 4.6(b). Such a long-term evolution of ξ profile [Fig. 4.6(b)] is fundamentally different from that seen in Fig. 4.6(e): although the geometric effect is also present in Fig. 4.6(e), the evolution of ξ profile in Fig. 4.6(e) is instead mainly due to the slow change of $D^{Li,eff}$.

The finite dimensional change [Eqn. (4-27)] is also responsible for the observation that the stresses at $t = 0.864T_0$ are lower than those at $0.1T_0$ in Fig. 4.6(c). The analysis in section 4.1 showed that, under fully elastic conditions, stresses scale with the current dimensions according to

$$\boldsymbol{\sigma} \propto \Delta\xi / J^{SF}. \tag{4-30}$$

On the other hand, eqn. (4-29) indicates that $\Delta\xi \propto \left(J^{SF}\right)^{2/3} / D_0^{Li}$. Therefore,

$$\boldsymbol{\sigma} \propto \left(J^{SF}\right)^{-1/3} / D_0^{Li} \tag{4-31}$$

When $\mathbf{J}^{Li,mech}$ is not considered, the diffusivity D_0^{Li} is constant and Eqn. (4-31) indicates that stresses are lower when J^{SF} is higher. This explains why the stresses at $t = 0.864T_0$ are lower than those at $0.1T_0$, as seen in Fig. 4.6(c). This geometric effect on long-term stresses is so significant that the plastic regions in Fig. 4.6(c) are unloaded back to the elastic regime as charging proceeds and the associated residue plastic strain leads to the positive slopes of $\sigma_{xx} = \sigma_{yy}$ at the center and surface at $t = 0.864T_0$.

It should be noted that the approximation embodied in Eqn. (4-27) is, strictly speaking, valid only when the deformation is elastic throughout the charging history, while the deformation in Fig. 4.6(c) does involve plasticity. Nevertheless, the above analysis qualitatively explains the long-term evolution of concentration and stress profiles in Fig. 4.6(c) because most of the charging history is in the elastic regime. It will be shown later that when the material undergoes full-scale yielding, Eqn. (4-27) must be revised, and the associated finite deformation would result in very different concentration profiles, with or without $\mathbf{J}^{Li,mech}$.

4.2.3. Neutralization of SED due to plastic flow (configuration a)

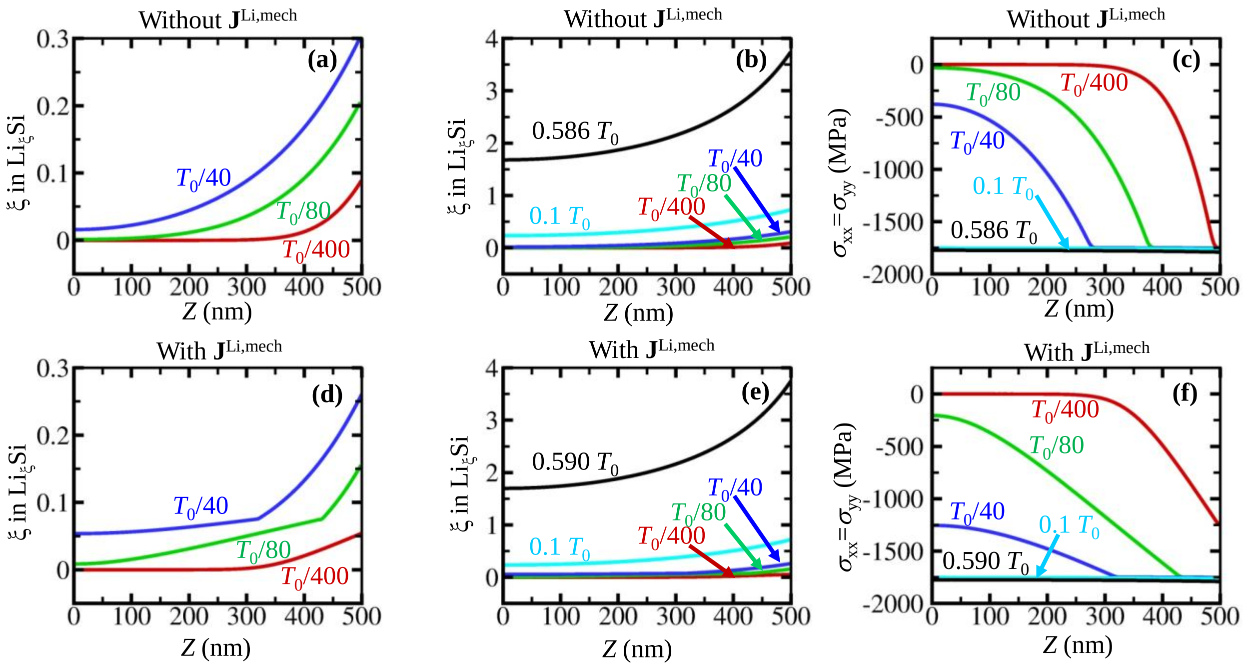

Fig. 4.8 Normalized Li concentration (a,b,d,e) and stress (c,f) profiles in a film with a thickness of H=500 nm and fully constrained at the bottom [configuration in Fig. 4.5(a)]. Here, lithiation-induced softening is not considered. (a-c) normalized concentration and stress profiles without mechanical driving force for diffusion. (d-f) normalized concentration and stress profiles with mechanical driving force for diffusion. For clarity, (a) and (d) show, with a finer vertical axis scale, the three early-stage profiles in (b) and (e), respectively.

The diffusion characteristics are drastically different when the thin film is fully constrained at the bottom, as shown in Fig. 4.8. First and foremost, due to the strong mechanical constraint, the film quickly reaches full-scale yielding regardless of if two-way coupling is accounted for [see Fig. 4.8 (c) and (f)]. More importantly, diffusive transport is much slower compared with that seen in Fig. 4.6. Specifically, $\bar{\xi}_{end} = 0.568\xi_{\max}$ without $J_K^{Li,mech}$ and $\bar{\xi}_{end} = 0.590\xi_{\max}$ with $J_K^{Li,mech}$. This occurs because of two reasons. First, when the material undergoes full-scale yielding, stress gradient essentially vanishes (specifically, $\nabla\sigma_m = 0$). Since $\left|\mathbf{J}^{Li,mech}\right| \propto \left|\nabla\sigma_m\right|$, the absence of stress gradient removes the SED effect. Indeed, the fact that $\bar{\xi}_{end}$ is approximately the same with and without $J_K^{Li,mech}$ is a direct result of the loss of SED. A look at Fig. 4.8(d) reveals sudden changes in the slope of ξ profiles at the boundary between the elastic and plastic zones. The steeper slope in the plastic zone (surface side) indicates that the effective diffusivity in the yielded region is much lower than that in the elastic region. As the charging proceeds, the boundary between the two zones moves from the surface towards the interior. Once the boundary reaches the bottom, the whole electrode is plastic with low effective diffusivity. The second reason for the slower Li transport is different finite dimensional change. When the film is fully constrained by the substrate, deformation occurs only in the *z*-direction (normal to the film plane), and the deformation gradient is approximately

$$\mathbf{F} \approx \mathbf{F}^{p}\mathbf{F}^{SF} = \begin{pmatrix} 1 & 0 & 0 \\ 0 & 1 & 0 \\ 0 & 0 & J^{SF} \end{pmatrix}. \tag{4-32}$$

On one hand, this deformation gradient is very different from that for the configuration in Fig. 4.5(b) [cf. eqn. (4-27)]. On the other hand, the arguments on J_Z^{Li} drawn by Eqs. (4-20)-(4-25) are still valid. Indeed, Fig. 4.9 (a) and (b) show similar J_Z^{Li} profiles as those in Fig. 4.7, at least to a first order of approximation. Although sharp kinks in J_Z^{Li} are seen in Fig. 4.9(b) for $t = T_0/80$ and $t = T_0/40$, the long-term profiles of J_Z^{Li} are fairly close to the 1st order approximation of $J_Z^{Li} \approx -\frac{Z}{H} J_{Surf}^{Li}$. For reasons similar to those in Eqs. (4-27)-(4-29), the long-term Li concentration profiles are now governed by

$$\frac{\partial C^{Li}}{\partial Z} = C^{Si} \frac{\partial \xi}{\partial Z} \approx \frac{\left(J^{SF}\right)^2}{D_0^{Li}} \frac{Z}{H} J_{Surf}^{Li} . \tag{4-33}$$

Here, because SED is lost when the film is under full scale yielding (i.e. $D^{Li,eff} = D_0^{Li}$), Eqn. (4-33) is valid for both the situations with and without $\mathbf{J}^{Li,mech}$. A comparison of Eqs. (4-33) and (4-29) indicates that the long-term $\Delta\xi$ for Fig. 4.8 (b) and (e) should be $\sim \left(J^{SF}\right)^{4/3}$ times larger than $\Delta\xi$ in Fig. 4.6(b). Simply speaking, because the current-configuration film thickness in the fully-constrained case is $\left(J^{SF}\right)^{2/3}$ times larger than that in the partially-constrained case, Li must now traverse a longer distance, giving another reason for why the diffusion is less efficient and $\bar{\xi}_{end}$ is smaller in Fig. 4.8(b) and (e) than in Fig. 4.6(b). As discussed previously, the lower $\bar{\xi}_{end}$ in Fig. 4.8(b) and (e) compared to the $\bar{\xi}_{end}$ in Fig. 4.6(b) indicates that fully-constrained thin-film electrodes must be charged with a lower operational rate than their partially-constrained counterparts, if the same final state of charge $\bar{\xi}_{end}$ is required.

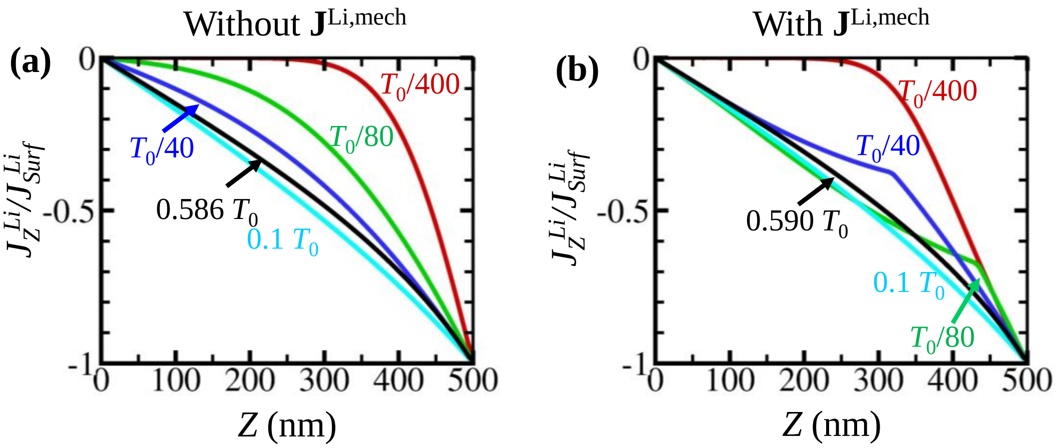

Fig. 4.9 Lagrangian lithium flux normalized by the surface influx when (a) mechanical driving force is not considered; (b) mechanical driving force is considered. Z denotes Lagrangian coordinate. The film is fully constrained at the bottom and lithiation-induced softening is not considered.

4.2.4. Stress-retarded diffusion due to lithiation-induced softening (configuration a)

It is important to note that diffusion in the fully-constrained film is slowed further when lithiation-induced softening is accounted for. To illustrate this effect, we first note that when $J_K^{Li,mech}$ is not considered [Fig. 4.10(a-b)], the concentration profiles are essentially the same as those in Fig. 4.8(a-b), although the stresses [Fig. 4.10(c)] are significantly different from those in Fig. 4.8(c). When the film undergoes full-scale yielding, the deformation gradients with and without lithiation-induced softening are comparable [both can be approximated by Eqn. (4-32)]. Therefore, in the absence of $J_K^{Li,mech}$, the two cases are governed by the same diffusion equations over approximately the same deformed configurations, hence, have roughly the same concentration profile. Indeed, $\bar{\xi}_{end}$ in Fig. 4.10(b) is approximately the same as that in Fig. 4.8(b), and J_Z^{Li} in Fig. 4.11(a) is approximately the same as that in Fig. 4.9(a). However, when $J_K^{Li,mech}$ is considered, $\bar{\xi}_{end}^{Li}$ in Fig. 4.10(e) is ~19% smaller than that in Fig. 4.8(e) and all the concentration profiles in Fig. 4.10(e) are significantly steeper than those in Fig. 4.8(e). The reason lies in the fact that when composition-induced softening is considered, σ_{xx}, σ_{yy}, and hence σ_m are all smaller at the surface than at the center. Since $J_K^{Li,mech}$ always points towards the same direction as the gradient of σ_m, it contributes a driving force which tends to "squeeze" lithium upward toward the surface. Because such a driving force does not exist in the absence of lithiation-induced softening, diffusion is more efficient in Fig. 4.8 than in Fig. 4.10. Again, the 1st order approximation of Lagrangian flux profile is $J_Z^{Li} \approx -\frac{Z}{H} J_{Surf}^{Li}$ [cf. Eqns. (4-20)-(4-25) and Fig. 4.11], i.e. the long-term profiles of J_Z^{Li} in Fig. 4.11 are not significantly different from those in Fig. 4.9, at least to a first order approximation. The less efficient diffusive transport therefore leads to steeper ξ profiles and hence lower $\overline{\xi}_{end}$ in Fig. 4.10 than in Fig. 4.8.

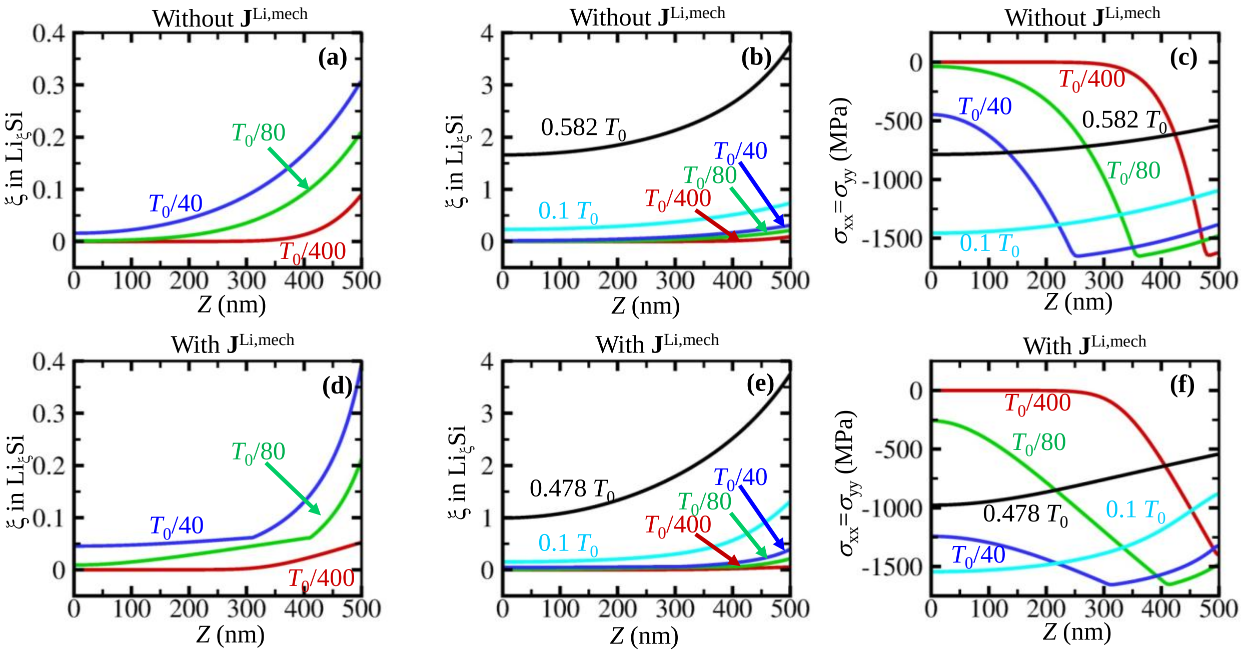

Fig. 4.10 Normalized Li concentration (a,b,d,e) and stress (c,f) profiles in a film with a thickness of H=500 nm and constrained at the bottom [configuration in Fig. 4.5(a)]. Lithiation-induced softening is considered. (a-c) normalized concentration and stress profiles when the mechanical driving force for diffusion is not considered. (d-f) normalized concentration and stress profiles when the mechanical driving force for diffusion is considered. For clarity, (a) and (d) show, with a finer vertical axis scale, the three early-stage profiles in (b) and (e), respectively.

The retardation of diffusion due two-way coupling is in striking contrast to that seen in the elastic regime [Fig. 4.6(d-e)], in which stress effects always enhances diffusion. Indeed, the validity of Eqn. (4-19) is strictly based on the premise that the deformation is elastic throughout the charging history. Our results indicate that whether the mechanical driving force assists or retards Li diffusion does not have a universal answer, and Li-transport is very sensitive to the externally applied mechanical constraints. This strong dependence of Li diffusion on mechanical constraints may help explain why Li diffusivities reported for different electrode configurations differ by several orders of magnitude, from 10^{-14} to 10^{-8} cm^{2}s^{-1} [79, 109, 112-114], because it is the effective diffusivity $D^{Li,eff}$ instead of the tracer diffusivity D_0^{Li} that can be experimentally measured. Specifically, Ruffo et al. measured $D^{Li,eff}$ for free-standing Si NWs to be 2×10^{-10} cm^2/s [113] while Soni et al. found that the upper bound for Li diffusivity in fully-constrained Si thin film is 10^{-11} cm^2/s [115]. Using the ideal-solution assumption [Eqn. (4-16) and (4-19)], we estimate that the effective diffusivity $D^{Li,eff}$ during elastic deformation is ~20 times higher than D_0^{Li} for an intermediate state of charging of $\bar{\xi} = \xi_{\max}/2$. Such a $D^{Li,eff}$ is appropriate for free-standing Si NWs which is not subject to strong mechanical constraints. For Si thin films, in contrast, stresses retard instead of enhance diffusion, leading to an effective diffusivity $D^{Li,eff}$ that is on the order of or even lower than D_0^{Li}. The model in this section is therefore consistent with the experimental findings by Ruffo et al. [113] and Soni et al. [115], in the sense that the $D^{Li,eff}$ may vary by one order of magnitude under different mechanical constraints. Admittedly, the ideal-solution assumption [Eqn. (4-16)] in this section entails a rather rough estimation of $\mu_{SF}^{Li}\left(C^{Li}\right)$. An accurate evaluation of $D^{Li,eff}/D_0^{Li}$ requires more realistic data on $\mu_{SF}^{Li}\left(C^{Li}\right)$ (which can be obtained once more accurate quasi-static OCP data is available). Such an evaluation is not the focus of this section. Nevertheless, the main result, i.e., the strong dependence of diffusion on mechanical constraints, is not obscured by this uncertainty associated with $\mu_{SF}^{Li}\left(C^{Li}\right)$. At least, the analysis here indicates that the mechanical constraint is a very important factor to consider when interpreting experimentally measured diffusivities. While many other factors (such as deposition conditions for the amorphous Si) may affect the measured Li diffusivity, the analysis here indicates even the mechanical constraint alone can lead to variance in $D^{Li,eff}$ by one order of magnitude.

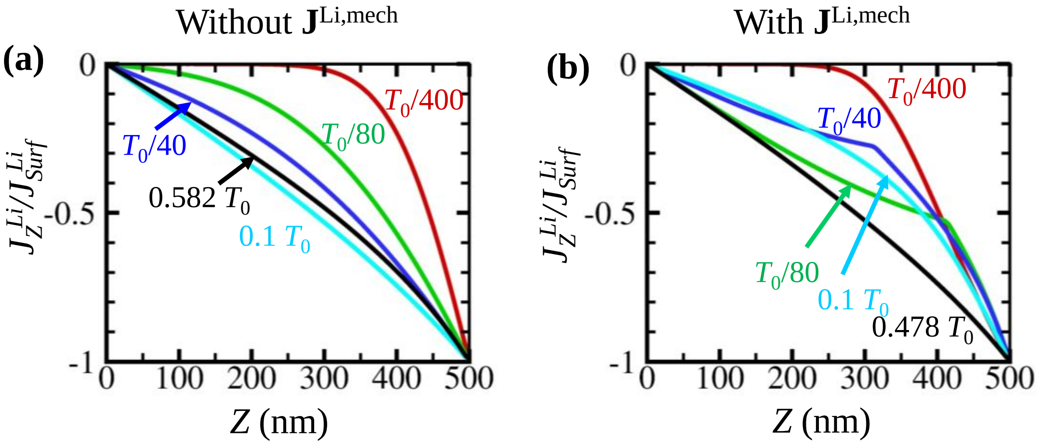

Fig. 4.11 Lagrangian lithium flux normalized by the surface influx when (a) mechanical driving force is not considered; (b) mechanical driving force is considered. Z denotes Lagrangian coordinate. The film is fully constrained at the bottom and lithiation-induced softening is considered.

4.2.5. Conclusions

The finding that lithium diffusion is very sensitive to external constraint can have profound practical implications. The design of battery electrodes involves tradeoffs among capacity, cyclability and operational charging rate. The main advantage of alloy-based electrodes, especially Li/Si, is their much higher capacity compared with carbon-based electrodes. In terms of cyclability, it has been suggested that plastic flow can be beneficial for Li/Si electrodes because it relaxes stresses and thus reduces the chance of electrode failure. Our results here, however, indicate that there is another mechanism at work. On one hand, plasticity may help avoid electrode fracture – a mechanism that can be utilized by adopting measures that promote inelastic flow through the tailoring of material properties and changing charging regimen. On the other hand, plasticity may inhibit Li transport, especially under tight mechanical constraint. Under any scenario, designs with less mechanical constraint on the electrodes are desirable because mechanical constraints diminishes stress-enhanced diffusion (SED) and magnifies the deleterious effect of plasticity and concentration-induced softening on Li transport. Because of these reasons, even in terms of operational charging rate alone, Li/Si nano-particles (e.g. nanospheres, nanoflakes, nanowires and nanotubes) are superior to Li/Si thin films or bulk materials. The results in this section provide further support for nano-particles as building blocks for next-generation alloy-based electrodes.

It should be noted that discussions in this section mainly concern electrodes with highly simplified geometries of slabs or films, in order to highlight the role of external constraints and the enhancement and retardation of diffusion by stresses [cf. Fig. 4.5]. For more complex electrode geometries with curved boundaries, stress profiles during plastic deformation will be more complex, but the conclusion that plastic flow reduces or neutralizes the effect of stress-enhanced diffusion most likely will still apply. The question is how to find the electrode geometry such that, for the same electrode material properties, the benefit of stress-enhanced diffusion can be maximized and the lithium transport can be tuned to be the fastest. Since the electrode will be subject to cyclic loading conditions, the design should not only consider the effect of plastic flow itself, but also the effect of the residual stresses which may be present after the plastic deformation stops. By the same token, residue stresses that arise due to the sharp phase boundaries during the first “priming” lithiation cycle [cf. section 2.1.1] could also play an important role. To design an electrode geometry such that the diffusion efficiency is maximized is not the focus of this study, but is nevertheless considered highly relevant and interesting by the author for future research.

4.3. Stress relaxation through interdiffusion

In section 4.1 and 4.2, we investigated the effect of diffusion-deformation two-way coupling on the lithium transport and the stress buildup by assuming zero host diffusivity. Many other studies based on this immobile-host assumption have been carried out to investigate the buildup and mitigation of stresses in Li-ion battery electrodes and the associated effects on the electrochemistry [19, 20, 22, 88, 96, 99, 116-119]. Tang et al. [94] showed that the elastic strain energy can significantly affect the electrochemistry in the cathode material of $LiFePO_4$. Bower et al. [16] developed a comprehensive framework and used it to analyze the time-dependent plasticity in thin-film Li/Si electrodes. Deshpande et al. [31] considered the effect of surface stresses and concluded that surface effect can reduce the tensile stresses in nano-sized electrodes, thereby improving electrode cyclability. Zhao et al. [33, 45] considered plastic deformation and showed that inelastic flow can significantly alleviate the stresses in Li/Si. The mechanisms for stress reduction considered in these analyses include stress-enhanced diffusion of Li, surface-effect-induced compressive stresses and plasticity.

One of the stress reduction mechanisms in Li-Si that have not been analyzed is the migration of Si (host) atoms which can be significant especially at high Li concentrations when the bonds between Si atoms are weakened or broken. Indeed, DFT calculations by Kim et al. [78] show that the bonding environment of silicon atoms changes significantly as lithium concentration increases, indicating that the diffusive migration of silicon may become non-negligible. Recently, Johari et al. [79] calculated the diffusivity of both Li and Si (D^{Li} and D^{Si}) in crystalline and amorphous Si (c-Si and a-Si) electrodes using ab initio molecular dynamics. They found that $D^{Li} = 1.67\times10^{-10} \sim 4.88\times10^{-9}$ $\mathrm{cm^2s^{-1}}$ and $D^{Si} = 1.97\times10^{-14} \sim 5.74\times10^{-13}$ $\mathrm{cm^2s^{-1}}$ for c-Si and

$D^{Li} = 1.25 \times 10^{-9} \sim 3.69 \times 10^{-8}$ cm^{2}s^{-1} and $D^{Si} = 1.53 \times 10^{-11} \sim 5.13 \times 10^{-10}$ cm^{2}s^{-1} for a-Si. The associated diffusivity ratio in a-Si falls into the range of $D^{Si} / D^{Li} = 0.8 \times 10^{-2} \sim 1.39 \times 10^{-2}$. It should be noted that the study by Johari et al. was conducted on Li/Si systems with the composition of $Li_{1.0}Si$. For higher Li contents, the diffusivity ratio D^{Si} / D^{Li} could be even higher since more Si-Si covalent bonds are broken. In Li/Ge, another promising alloy-based electrode material, host diffusion could be even more significant since the Ge-Ge covalent bond is much weaker than the Si-Si bond (the melting temperatures of crystalline Si and Ge are 1687 K and 1211.40 K, respectively).

In this section, we analyze the implication of a small but non-zero D^{Si} in amorphous Li/Si electrodes (host H=Si and guest G=Li). One focus of the analysis is the relative importance of the mechanical driving force [eqn. (3-2)] and the chemical driving force [eqn. (3-1)] for host atom migration. The analysis also focuses on the direction of the diffusive migration of host (Si) atoms and the dependence of the direction on the relative strengths of the chemical and mechanical driving forces. A parametric study is carried out over a range of values of host diffusivity and the thermodynamic factor which measures the tendency for the Li and Si atoms to chemically mix. In particular, the analysis allows the effect of Si diffusion on stress evolution to be quantified. The calculations also focus on the time scales associated with the diffusive migration of guest and host, and how these time scales affect the evolution and distributions of stresses and concentrations, especially at charge times beyond the characteristic time scale for host migration. The results will show quantitatively that the diffusion of Si is a significant mechanism for stress relief in Li/Si, in addition to SED and inelastic deformation. Of particular interest is the finding that the steady-state distributions of stresses at times much longer than the characteristic time for Si diffusion depends on neither the thermodynamic factor nor the diffusivity of Si.

Section 4.3 is based on the interdiffusion theory of chapter 2, the mixed finite element framework of chapter 3, and the numerical results published in ref [18].

4.3.1. Migration of host atoms in Li/Si nanowire electrodes

We consider a cylindrical Li/Si nanowire [inset of Fig. 4.12(a)] with radius $\rho_0 = 250\,\text{nm}$ when fully discharged. This fully-discharged state is taken to be the Lagrangian reference state. The NW is charged from its outer cylindrical surface at a constant Lagrangian lithium influx Q^{Li} [cf. Eqn. (3-8)]. Under galvanostatic conditions,

$$Q^{Li} = \frac{1}{2}\rho_0 C_0^{Si} \xi_{\max} \frac{1}{T_0}, \qquad (4\text{-}34)$$

where $\xi_{\max}$ is the maximum charging limit for lithium per silicon, C_0^{Si}=49.3 atoms/nm^3 is the silicon concentration in fully discharged state (the density of pure amorphous Si is 2.30 g/cm^3) [108], and T_0 is the nominal time required to attain full charge. In this section, we take $\xi_{\max} = 4.4$ and T_0 =1 hour (i.e. at 1C charging rate). End effects are neglected because the aspect ratio of the NW is assumed to be very large. Numerically, this is achieved by forcing the top and bottom surfaces to remain flat using the multi-point constraint (MPC) functionality in ABAQUS.

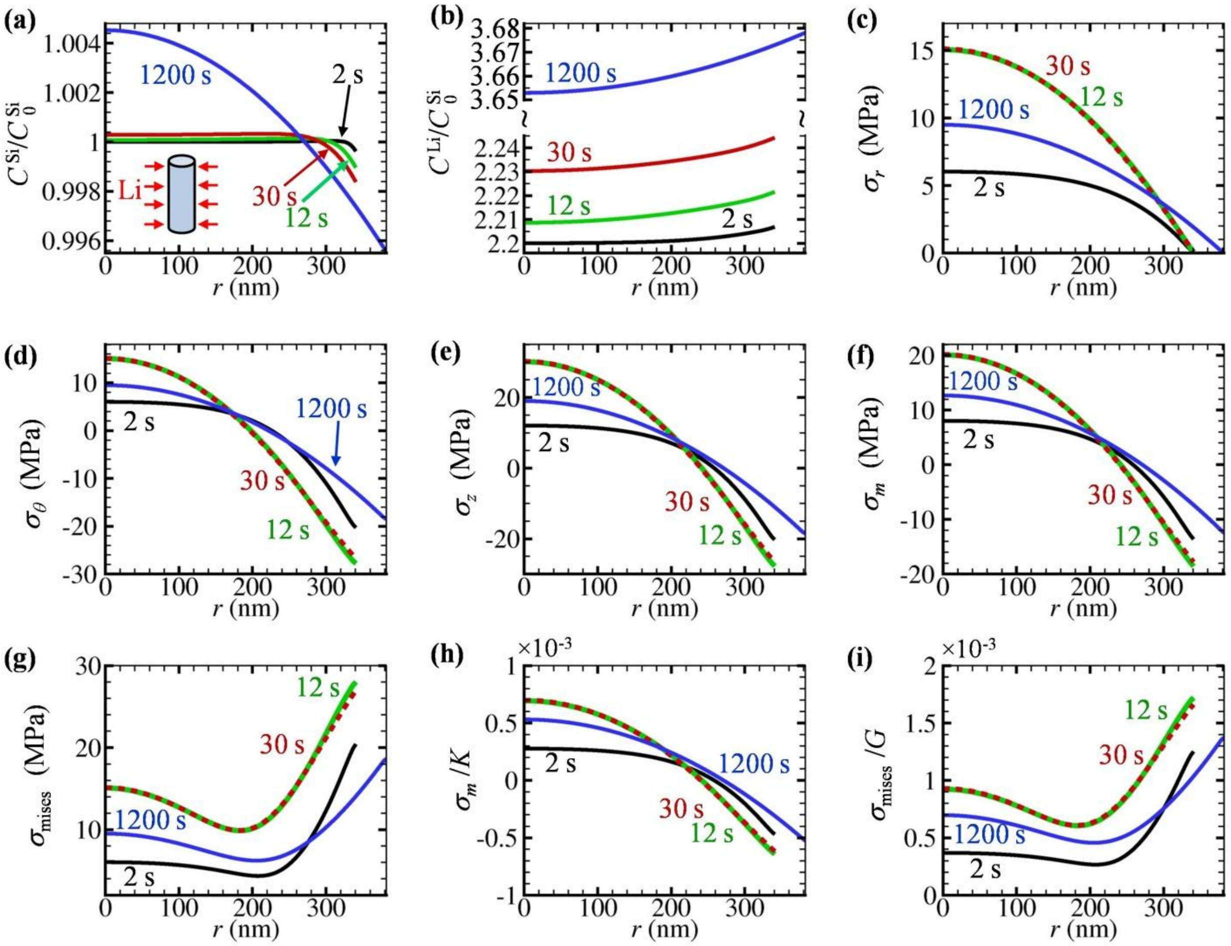

Fig. 4.12. Concentration and stress profiles for a Li/Si NW with radius $\rho_0 = 250\,\mathrm{nm}$ *, thermodynamic factor* $\Phi = 10$ *and diffusivity ratio* $D^{Si}/D^{Li} = 0.02$*. Results at different stages up to the fully charged state are shown. The charging rate is 1C and the initial composition is* $Li_{2.2}Si$*. (a) normalized Lagrangian silicon concentration profiles at different stages of charging, the normalization is relative to* C_0^{Si}*. The radial coordinate r is measured in the current configuration. The inset shows the NW charged under galvanostatic conditions at a constant surface influx* Q^{Li}*. The z-axis of the cylindrical coordinate system is along the NW axis. (b) profiles of normalized Lagrangian Li concentration, the normalization is relative to* C_0^{Si}*. (c-g) profiles of radial, hoop and azimuthal stress components and the hydrostatic and von Mises invariants. (h-i) hydrostatic and von Mises stresses, normalized by the composition-dependent elastic modulus.*

A linear composition-expansion curve ($\xi = x^{Li} / x^{Si}$ vs. J^{SF} curve under fixed C^{Si}) with constant partial atomic volumes $\Omega^{\mathrm{Si\,(SF)}} = 1/C_0^{Si}$ =20.3 $\mathrm{\AA}^3$ and $\Omega^{\mathrm{Li\,(SF)}} = 14.3$ $\mathrm{\AA}^3$ [12, 43] is used. Recent calculations by Huang and Zhu indicates that the $\xi \sim J^{SF}$ relationship could be non-linear [71]. Here, a linear $\xi \sim J^{SF}$ relation is used in order to simplify the formulation and interpretation of numerical results and to focus on the implications of non-zero host diffusivity. The concentration-dependent elastic properties are $K = K\left(\xi\right) = (12.46\xi + 65.44)/(1+\xi)$ GPa and $G = G\left(\xi\right) = (7.63\xi + 35.51)/(1+\xi)$ GPa [77]. Reported D^{Li} values in Li/Si typically range from 10^{-14} to 10^{-8} $\mathrm{cm^2s^{-1}}$ [79, 109, 112-114]. In this section we take $D^{Li} = 10^{-12}$ $\mathrm{cm^2s^{-1}}$. Although the predicted stress levels depend on the value of D^{Li} according to the scaling law of $\boldsymbol{\sigma} \propto 1/D^{Li}$ [88], the key issue in this study, i.e., the effect of host diffusion, is not controlled by D^{Li} itself but by the diffusivity ratio D^{Si} / D^{Li} . This host-to-guest diffusivity ratio in amorphous Si electrodes at room-temperature is found by Johari et al. [79] to be $D^{Si} / D^{Li} = 0.8\times10^{-2} \sim 1.39\times10^{-2}$ for $Li_{1.0}Si$. Since silicon-silicon bonding is much weaker in high-x^{Li} states [78], D^{Si} could be even larger at higher x^{Li} . Indeed, at very low x^{Li} , D^{Si} approaches the silicon self-diffusivity which is negligible compared to D^{Li} . We therefore start our simulation at the half charged state of $Li_{2.2}Si$ in order to more realistically capture the effect of Si migration. Specifically, at $t = 0$ the NW is assumed to be a homogeneously half-charged alloy with $C_{t=0}^{Si} = C_0^{Si}$ and $C_{t=0}^{Li} / C_{t=0}^{Si} = 2.2$. It should be noted that the Lagrangian reference state (upon which C^{Li} and C^{Si} are measured) here is taken to be the fully discharged configuration instead of the half-charged configuration at $t = 0$. A parametric study is carried out by systematically varying the D^{Si}/D^{Li} ratio from 0.005 to 0.05 while keeping $D^{Li}=10^{-12}$ cm^{2}s^{-1} constant.

It should be noted that the diffusivities (D^{Li} and D^{Si}) might depend on the local stress state. Haftbaradaran et al. [19] considered the activation barrier shift ΔE_b for lithium diffusion due to stresses [120] and showed that the stress effect could slow down lithium diffusion through $D^{Li}=D_0^{Li}\exp\left(-\Delta E_b/k_B\theta\right)$. While stress-induced activation barrier change ΔE_b is more important under very high stresses, stress development and diffusion mainly couple through the chemical potential for moderate stresses [111]. For Li diffusion in silicon, it has been shown that $\left|\Delta E_b/k_B\theta\right|\approx 1$ only when $\left|\sigma_b\right|$ reaches as high as 1 GPa, otherwise, the factor $\exp\left(-\Delta E_b/k_B\theta\right)$ is negligible [43]. For simplicity, the effect of the factor $\exp\left(-\Delta E_b/k_B\theta\right)$ is not considered. This approximation should be valid at least for the stress levels considered in this section.

Fig. 4.12 (a) and (b) show the profiles of the normalized Lagrangian concentrations $C^{Si}\left(r,t\right)/C_0^{Si}$ and $C^{Li}\left(r,t\right)/C_0^{Si}$ for a NW with $\rho_0=250\,\text{nm}$, $\Phi=10$ and $D^{Si}/D^{Li}=0.02$. The Li concentration $C^{Li}\left(r,t\right)$ quickly (in less than ~12 s) reaches a profile corresponding to the long-term solution obtained in section 4.1, i.e., for most of the charging process (times beyond ~12 s), the distribution of $C^{Li}\left(r,t\right)$ effectively increases uniformly over the entire wire radius, with the shape of the profiles largely unchanged. This observation is consistent with the stress profiles in Fig. 4.12 (c-g) which show that the stress distributions for 12 s and 30 s essentially match. It should be pointed out that, strictly speaking, the shape of $C^{Li}\left(r,t\right)$ profiles does evolve even after 12 s, and the stresses at 1200 s is lower than those at 12 s and 30 s. However, this slow modulation of $C^{Li}\left(r,t\right)$ is due to composition-induced material softening (dependence of K and G on Li/Si composition), change of NW size, and Si migration, but not due to the transience of the Li diffusion process. The characteristic time τ^{Li} for reaching the steady-state gradient of $C^{Li}\left(r,t\right)$ is very short compared with the overall charging time and can be estimated to be $\tau^{Li} \approx \rho^2 / \lambda_1^2 D_{eff}^{Li}$ according to the analytical solution for the case of $D^{Si} = 0$ (cf. section 4.1 and ref. [43]). Here, $\rho \approx \left[J^{SF}\left(C_{t=0}^{Si}, C_{t=0}^{Li}\right)\right]^{1/3} \rho_0$ is approximately the NW radius during the initial stage of charging, $\lambda_1 = 3.8317$ is the first root of the first-order Bessel function, and

$$D_{eff}^{Li} = D^{Li}\left[\frac{\Phi}{1+C_{t=0}^{Li}/C_{t=0}^{Si}} + \frac{1}{k_B\theta}\frac{2E\left(\Omega^{Li(SF)}\right)^2}{9\left(1-\nu\right)}\frac{C_{t=0}^{Li}}{J^{SF}\left(C_{t=0}^{Si}, C_{t=0}^{Li}\right)}\right] \qquad (4\text{-}35)$$

is the effective diffusivity of Li. In the above relation, E and ν are the Young's modulus and Poisson ratio, respectively. For $\Phi = 10$, $D^{Si} = 0$ and $D^{Li} = 10^{-12}$ cm^{2}s^{-1} , $\tau^{Li} \approx 2.7$ s; hence long-term profiles with a steady-state shape can be expected for $C^{Li}\left(r,t\right)$ when $t > 2\tau^{Li} \approx 5.4$ s [43], consistent with what is seen in Fig. 4.12.

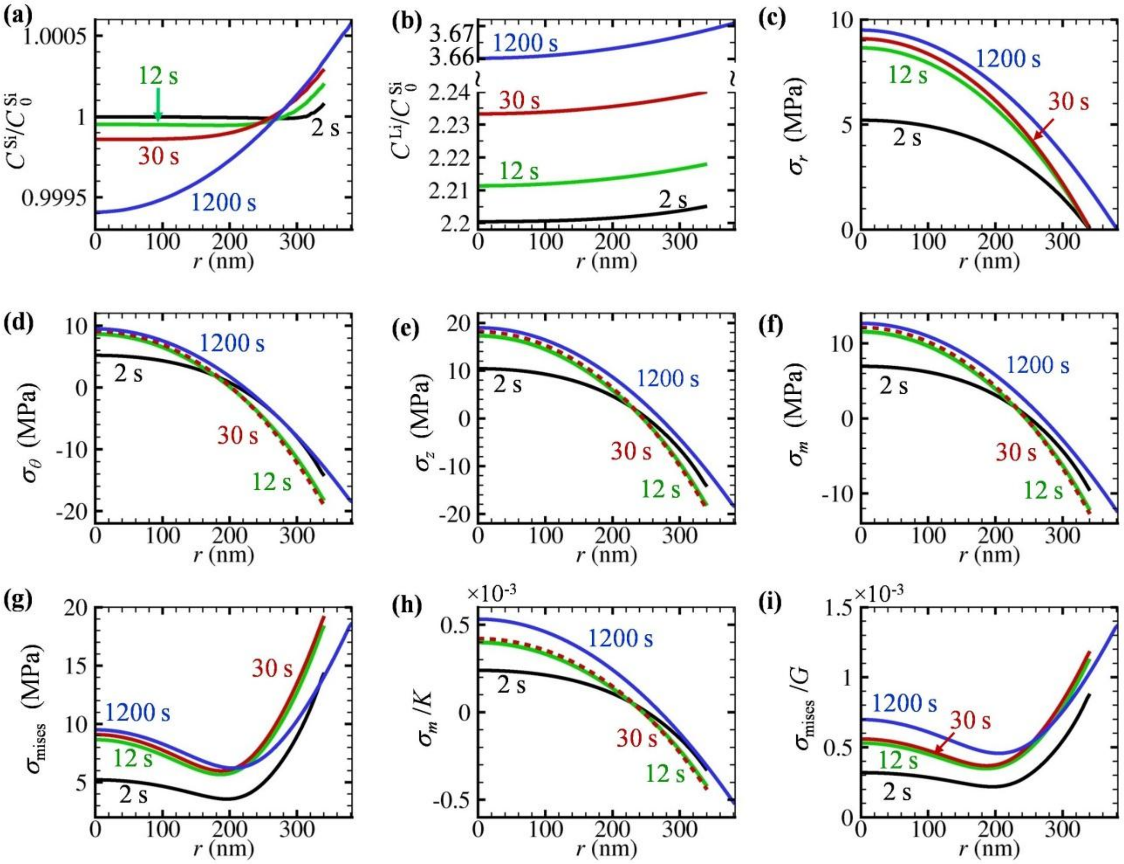

Fig. 4.13. Concentration and stress profiles for a NW with radius $\rho_0 = 250\,\mathrm{nm}$, thermodynamic factor $\Phi = 90$ and diffusivity ratio $D^{Si}/D^{Li} = 0.02$. The NW radius, rate of charge (1C) and an initial composition ($Li_{2.2}Si$) are the same as those in Fig. 4.12.. (a) and (b) normalized Lagrangian concentration profiles of silicon and lithium, respectively. (c-g) profiles of radial, hoop, azimuthal, hydrostatic and von Mises stresses. (h-i) hydrostatic and von Mises stresses, normalized by the composition-dependent elastic bulk and shear modulus.

The transient evolution of $C^{Si}(r,t)$ [Fig. 4.12(a)], on the other hand, is much slower than the transient evolution of $C^{Li}(r,t)$. As the charge progresses, C^{Si} at the NW surface decreases from the initial value and C^{Si} at the center increases from the initial value. This indicates that Si atoms slowly migrate from the surface towards the center. Like C^{Li}, C^{Si} also evolves towards a long-term steady-state profile, except that the time required by this transient evolution is longer than that for C^{Li} (~ 12 s), as confirmed by the $D^{Si}/D^{Li} = 0.02$ curve in Fig. 4.15(a). The shape of the steady C^{Si} profile is shown by the curve for $t = 1200$ s in Fig. 4.12(a). During the initial charging stage ($t < 12$ s), the stresses increase and the development is similar to that for the case with $D^{Si} = 0$ [43]. After the initial stage ($t > 12$ s), the stresses slowly decrease. As seen in Fig. 4.12(c-g), all three stress components (radial σ_r, hoop σ_θ and longitudinal σ_z) and the two stress invariants (hydrostatic stress σ_m and the Mises equivalent stress σ_{mises}) are lower at $t = 1200$ s than at $t = 12$ s. One reason for the decrease in stresses is composition-change-induced softening of Li/Si alloy. Specifically, the lower elastic modulus (*K* and *G*) values at higher x^{Li} levels cause the stresses to be lower. Nonetheless, this trend remains even if the stresses are normalized by the composition-dependent bulk and shear modulus, as σ_m / K and σ_{mises} / G are still significantly lower at $t = 1200$ s than at $t = 12$ s [Fig. 4.12(h) and (i)]. This decrease of σ_m / K and σ_{mises} / G is caused by the diffusive migration of the host (Si) atoms. Since Si migrates from the surface to the center, J^{SF} increases at the center and decreases at the surface relative to the case with $D^{Si} = 0$, leading to lower levels of $\boldsymbol{\varepsilon}^e$ and, consequently, the relaxation of the stresses.

To analyze the effect of the thermodynamic factor Φ, the results of a case with $\Phi = 90$ and $D^{Si}/D^{Li} = 0.02$ are shown in Fig. 4.13. The NW diameter, charging rate and diffusivities are the same as those in Fig. 4.12. The profiles of C^{Li} [Fig. 4.13(b)] and the stress components [Fig. 4.13(c-i)] are qualitatively similar to those for the $\Phi = 10$ case in Fig. 4.12 for $t < 30$ s, primarily because Si diffusion is too slow to have a significant influence during the initial stage, although the magnitudes of these quantities are understandably different as the effective diffusivities are dependent on Φ. The profiles of C^{Si}, however, are distinctively different. In Fig. 4.13, C^{Si} increases at the surface and decreases at the center; indicating Si migration is from the center to the surface. This is directly opposite to what is seen in Fig. 4.12. The opposite directions of Si migration lead to significant differences in the stress distributions in the NW. Specifically, at the higher thermodynamic factor value of $\Phi = 90$ (higher tendency to chemically mix between the two species), the stresses at $t = 1200$ s are higher than the stresses at $t = 12$ s and $t = 30$ s [Fig. 4.13(c-g)]. In contrast, at the lower thermodynamic factor value of $\Phi = 10$, the stresses at $t = 1200$ s are lower than the stresses at $t = 12$ s and $t = 30$ s. The same observations are made for the normalized stresses σ_m / K and σ_{mises} / G [Fig. 4.13(h-i)] as well.

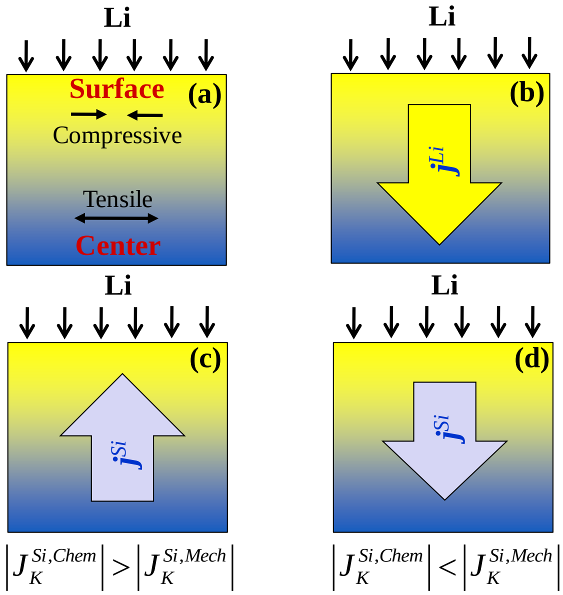

Fig. 4.14. The competition between the effects of chemical mixing and mechanical stress on the diffusive migration of host (Si) in Li/Si. (a) When lithium is inserted from the surface, compressive stresses develop near the surface and tensile stresses develop at the center. (b) Lithium diffuses from surface to center. (c) When the chemical effect dominates, the flow of the host (Si) is from the center to the surface of the NW. (d) When the mechanical effect dominates, the flow of the host (Si) is from the surface to the center. Realistic scenarios for Li/Si almost certainly entail (d).

The migration of Si is different between the $\Phi = 10$ and $\Phi = 90$ cases due to the competition between the chemical contribution [Eqn. (3-1)] and the mechanical contribution [Eqn. (3-2)] to the diffusive flux of silicon. The chemical contribution $\mathbf{J}^{Si,chem} \propto -\partial x^{Si} / \partial \mathbf{X}$ drives Si flow from high x^{Si} regions (center) towards low x^{Si} regions (surface), causing the composition field to homogenize. The mechanical contribution $\mathbf{J}^{Si,mech}$, on the other hand, is proportional to $\partial \sigma_m / \partial \mathbf{X}$ and, therefore, drives Si flow from compressive regions (surface) towards the stretched regions (center). The magnitude of $\mathbf{J}^{Si,chem}$ is proportional to Φ while the magnitude of $\mathbf{J}^{Si,mech}$ is controlled by $\Omega^{\mathrm{Si\,(SF)}}$. For $\Phi = 90$, $\left|\mathbf{J}^{Si,chem}\right| > \left|\mathbf{J}^{Si,mech}\right|$ and $\mathbf{J}^{Si} = \mathbf{J}^{Si,chem} + \mathbf{J}^{Si,mech}$ points towards the surface. For $\Phi = 10$, $\left|\mathbf{J}^{Si,chem}\right| < \left|\mathbf{J}^{Si,mech}\right|$ and $\mathbf{J}^{Si}$ points towards the center. This competition between the chemical effect and the mechanical effect is illustrated in Fig. 4.14. Here, the value of Φ can be estimated from the open-circuit potential $U^{OCP} = U^{OCP}\left(x^{Li}\right)$ data via [43]

$$\Phi = -\left(e / k_B \theta\right) x^{Li} dU^{OCP} / dx^{Li}. \qquad (4\text{-}36)$$

It should be noted that, however, experimentally measured $U^{OCP}\left(x^{Li}\right)$ curves for Li/Si are associated with significant hysteresis [70] which makes accurate estimate of the quasi-equilibrium value of dU^{OCP} / dx^{Li} difficult. Using the experimental OCP data of Chandrasekaran et al. [89] and eqn. (4-36), we estimate that $1 \le \Phi \le 40$ for $2.2 < C^{Li} / C^{Si} < 4.4$ (the composition range studied in this section). Therefore, the scenario in Fig. 4.13 and Fig. 4.14(c) reflects the outcome for an unrealistically high value of Φ for Li/Si; instead, the diffusive migration of silicon always leads to stress relaxation in Li/Si and causes Si to migrate along the direction of σ_m gradient [Fig. 4.12(a)].

4.3.2. Effect of D^{Si}/D^{Li} and Φ on stress relaxation

Fig. 4.15 shows how the diffusivity ratio D^{Si}/D^{Li} affects the evolution of the stresses and silicon concentration when the thermodynamic factor is kept at $\Phi = 10$. The NW configuration is the same as that in Fig. 4.12 and Fig. 4.13, with a diameter of 250 nm when fully discharged. The charging rate is 1C under galvanostatic conditions. The normalized silicon concentration C^{Si}/C_0^{Si}, normalized hydrostatic stress σ_m/K and normalized von Mises stress σ_{mises}/G are plotted against time at the NW surface and center (denoted as s and c, respectively). For all D^{Si}/D^{Li} ratios from 0.005 to 0.05, the migration of Si is from the surface to the center, as a result of the dominant effect of $\mathbf{J}^{Si,mech}$ [Fig. 4.15(a), Eqn. (2-42)].

At the very low diffusivity ratio of $D^{Si}/D^{Li} = 10^{-8}$, the migration of silicon is essentially negligible. Under this condition, σ_m/K and σ_{mises}/G only change slightly after the initial stress buildup. The analytical solution for $D^{Si} = 0$ during the so-called long-term response period after the initial transient buildup has been given in section 4.1 as [cf. Eqn. (4-6)]

$$\begin{cases} \sigma_z = -\dfrac{1}{3}\dfrac{1}{J^{SF}}\dfrac{\Omega^{Li(SF)}}{\Omega^{Si(SF)}}\dfrac{E}{1-\nu}\cdot\Delta\xi, \\ \sigma_\theta = \dfrac{1}{3}\dfrac{1}{J^{SF}}\dfrac{\Omega^{Li(SF)}}{\Omega^{Si(SF)}}\dfrac{E}{1-\nu}\left(-\Delta\xi + \dfrac{1}{\tilde{r}^2}\displaystyle\int_0^{\tilde{r}}\tilde{r}\Delta\xi d\tilde{r}\right), \text{and} \\ \sigma_r = -\dfrac{1}{3}\dfrac{1}{J^{SF}}\dfrac{\Omega^{Li(SF)}}{\Omega^{Si(SF)}}\dfrac{E}{1-\nu}\dfrac{1}{\tilde{r}^2}\displaystyle\int_0^{\tilde{r}}\tilde{r}\Delta\xi d\tilde{r}, \end{cases} \tag{4-37}$$

where $\Delta\xi(r,t) \equiv \xi - \bar{\xi}$ can be regarded as the composition inhomogeneity, $\xi \equiv C^{Li} / C_0^{Si}$, $\bar{\xi}(t) = \xi_{\max}(t / T_0)$ is a measure for the average composition over the NW radius and $\tilde{r} \equiv r / \left\{ \left[J^{SF} \left(C_0^{Si}, C^{Li} \right) \right]^{1/3} \rho_0 \right\}$ is the nondimensionalized radius. Obviously, the long-term stresses for $D^{Si} = 0$ depend on two factors. The first factor is NW size. As J^{SF} increases due to Li insertion, the stresses may decrease even when $\Delta\xi$ does not change. The second factor is the effective Li diffusivity D_{eff}^{Li}, which depends on the elastic modulus [Eqn. (4-35)]. As Li concentration increases, the Li/Si alloy softens, leading to lower D_{eff}^{Li} and causing the composition inhomogeneity $\Delta\xi$ to change accordingly.

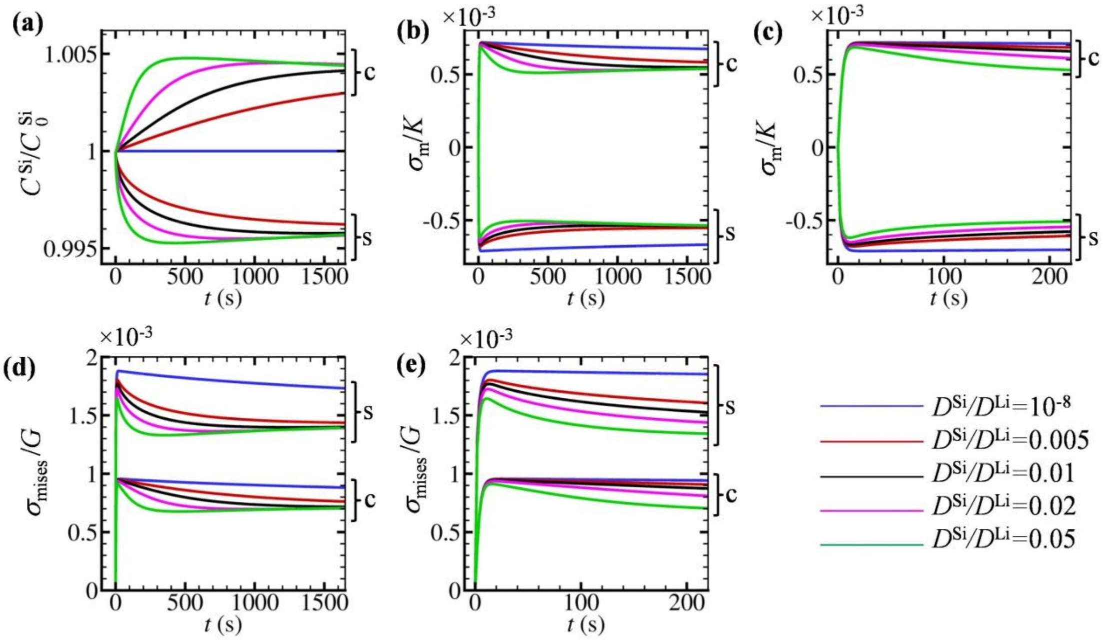

Fig. 4.15. Evolution of silicon concentration and stress invariants at the NW center (denoted by c) and surface (denoted by s). The NW configuration, charging rate, and thermodynamic factor Φ are the same as those in Fig. 4.12.

The only difference is in D^{Si}/D^{Li} *which is varied here. (a) Lagrangian silicon concentration normalized by* C_0^{Si}*. (b) hydrostatic stress normalized by bulk modulus K; (c) details of (b) in the first 200 s. (d) von Mises stress normalized by shear modulus G. (e) details of (d) in the first 200 s.*

Using the numerical solution for $D^{Si}/D^{Li}=10^{-8}$ or the analytical solution for $D^{Si}=0$ as the reference, we can quantify the effects of Si migration on stress relaxation. The normalized stress invariants σ_m/K and σ_{mises}/G (note that K and G are concentration-dependent and, therefore, decrease with time) first increase during the ramp up of the C^{Li} profile and then decrease as the effect of Si diffusion kicks in. The stresses at the center follow similar trends as the stresses near the surface but lag behind the stresses at the surface because the gradient of the hydrostatic stress $\left|\partial\sigma_m/\partial\mathbf{X}\right|$ [hence $\left|\mathbf{J}^{Si,mech}\right|$ according to Eqn. (3-2)] is higher near the surface than at the center. Note that for $D^{Si}\approx 0$, long-term σ_m/K and σ_{mises}/G change only slightly after $t=12$ s. In contract, the stresses decrease significantly more rapidly at the higher values of D^{Si}. Specifically, for $D^{Si}/D^{Li}=0.02$, the values of σ_m/K and σ_{mises}/G at the surface at $t=1200$ s are both ~20% lower than the corresponding values for $D^{Si}\approx 0$, as well as their corresponding peak values at $t\approx 12$ s. The reductions clearly show that modest mobility of the host atoms (low D^{Si} value of $2\times10^{-14}\,\text{cm}^2\text{s}^{-1}$ or $D^{Si}/D^{Li}=0.02$) can cause stress reductions on the order of ~20% relative to the case without Si mobility. It should be noted that the stress levels here are significantly lower than the yield stress of Li/Si of 1.0~1.75 GPa [15]. The stress relaxation due to host migration is separate from and in addition to the effects of stress-enhanced diffusion of Li [43] and plasticity [45]. Obviously, it can play an important role at high Li concentration levels even when stresses are below the yield threshold of the material.

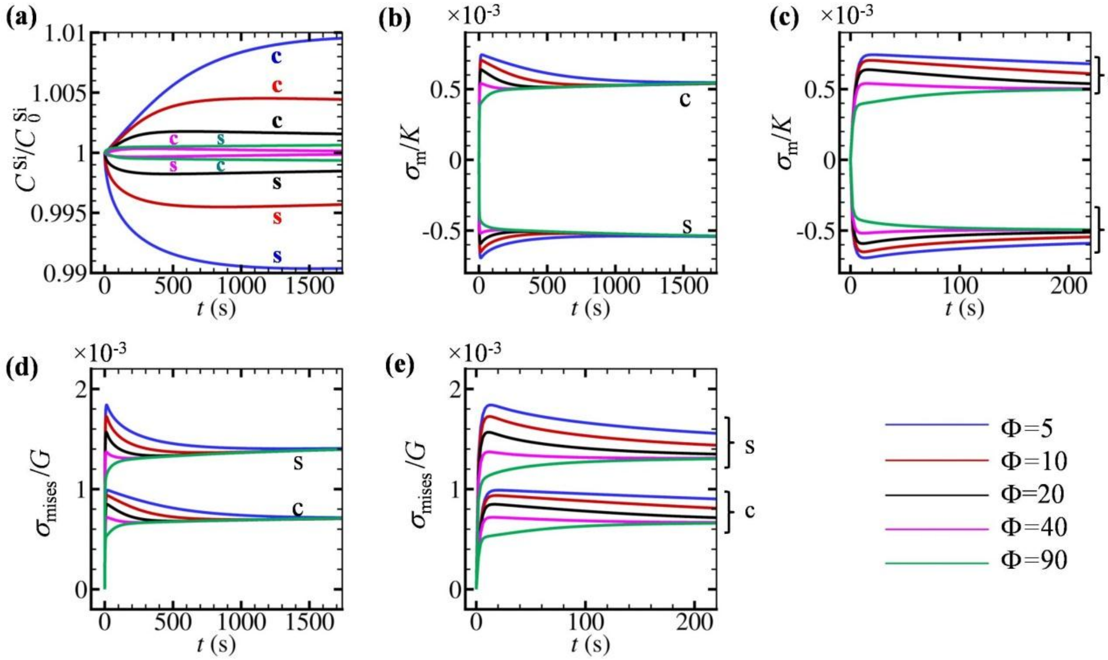

Fig. 4.16. Evolution of silicon concentration and stress invariants at the NW center (denoted as c) and surface (denoted as s) at different values of Φ *between 5 and 90. The diffusivity ratio is kept at* $D^{Si}/D^{Li}=0.02$. *All other parameters are the same as those in Fig. 4.12. (a) Lagrangian silicon concentration* C^{Si} *normalized by* C_0^{Si}. *(b) Hydrostatic stress* σ_m *normalized by bulk modulus K; (c) Details of (b) in the first 200 s. (d) von Mises stress* σ_{mises} *normalized by shear modulus G. (e) Details of (d) in the first 200 s.*

It is important to note that, for all the D^{Si}/D^{Li} values analyzed, $C_{surface}^{Si}/C_0^{Si}$ at the surface converges to the same steady-state surface value of ~0.996 and C_{center}^{Si}/C_0^{Si} at the center converges to the same steady state value of ~1.004. The relaxation (or characteristic) time τ^{Si} for silicon redistribution can be estimated using the time for $\left(C_{center}^{Si}-\bar{C}^{Si}\right)/C_0^{Si}$ to reach half of its steady-state value, here $\bar{C}^{Si}=C_0^{Si}$ is the average silicon concentration in the NW. According to Fig. 4.15 (a), $\tau^{Si}\approx 210$ s for $D^{Si}=2\times10^{-14}$ cm^{2}s^{-1} ($D^{Si}/D^{Li}=0.02$). The convergences of

$C^{Si}_{surface}/C^{Si}_{0}$ and $C^{Si}_{center}/C^{Si}_{0}$ are not by chance. They indicate that Si migration always tends to lead to a steady state which is the same regardless of the value of D^{Si}, as long as $D^{Si}>0$. This steady state is reflected not only in C^{Si}/C^{Si}_{0}, but also in the stresses. Specifically, σ_m/K converges to the same level of $\sigma_m^{t>>\tau^{Si}}/K$ at the center and the same level of $-\sigma_m^{t>>\tau^{Si}}/K$ at the surface [Fig. 4.15(b)] at $t>>\tau^{Si}$(e.g., $t/\tau^{Si}>3$). Fig. 4.15 shows that $\sigma_m^{t>>\tau^{Si}}/K=0.00054$ for $\Phi=10$. A similar convergence of σ_{mises}/G at long times is seen in Fig. 4.15(d). It is important to note that the steady state values of $C^{Si}_{t>>\tau^{Si}}/C^{Si}_{0}$ for the surface and the center do evolve slightly as *t* further increases. This modulation of the steady state values of $C^{Si}_{t>>\tau^{Si}}/C^{Si}_{0}$ at the surface and the center is because of the softening of the elastic modulus as x^{Li} increases, which lowers the mechanical driving force for silicon migration [Eqn. (3-2)]. As seen in Fig. 4.15(b) and (d), the normalized stresses σ_m/K and σ_{mises}/G decrease accordingly after the transient development of the C^{Si} profile. Parametric study shows that the characteristic time τ^{Si} for achieving the steady state $C^{Si}_{t>>\tau^{Si}}/C^{Si}_{0}$ distribution decreases as D^{Si}/D^{Li} increases. This is understandable because $\tau^{Si}\propto 1/D^{Si}$. It should be noted that, however, τ^{Si} cannot be simply estimated as $\rho^2/\lambda_1^2 D^{Si}$ using the tracer diffusivity D^{Si}, because such an estimation does not reflect the fact that Si diffusion is affected by the migration of Li through the stress driving forces and the Li-Si chemical interactions. Indeed, $\rho^2/\lambda_1^2 D^{Si}\sim 2\times 10^3$ s for $D^{Si}=2\times 10^{-14}\,\text{cm}^2\text{s}^{-1}$ if the diffusion of Si occurs independently by itself without the presence of Li and without SED. Rather, it is the effective diffusivity D^{Si}_{eff} of Si, that determines τ^{Si}. Although a closed-form solution for D^{Si}_{eff} may not be easily obtained [in contrast, D^{Li}_{eff} which is analytically quantified in Eqn. (4-35)], the numerical results here indicate that $D_{eff}^{Si} >> D^{Si}$ due to the strong coupling between stress and interdiffusion, at least for the case of $\Phi = 10$.

Fig. 4.16 illustrates the effect of Φ at a constant diffusivity ratio of D^{Si} / D^{Li} =0.02. Again, the NW radius is 250 nm at the fully discharged state and the charging rate is 1C. The most important observation is that the direction of Si migration changes as Φ changes. Specifically, Si migrates from the surface to the center for $5 < \Phi < 40$ and from the center to the surface for $\Phi = 90$ [see Fig. 4.16(a)]. The reversal occurs at a critical value Φ_{cr} , when $\mathbf{J}^{Si,mech}$ and $\mathbf{J}^{Si,chem}$ happen to cancel each other out. It should be noted that $\left|\mathbf{J}^{Si,mech}\right|$ depends on the magnitude of the elastic modulus, which decreases as lithium concentration increases. Therefore, the critical value Φ_{cr} is not a constant. A typical value is found to be approximately $\Phi_{cr} = 50$. When Φ is close to $\Phi_{cr} = 50$, silicon migration is insignificant since $\mathbf{J}^{Si,mech} + \mathbf{J}^{Si,chem}$ is very small, although it may not be exactly zero.

When $\Phi < \Phi_{cr}$, stresses first increase and then decrease gradually after reaching respective peaks [Fig. 4.16(b-e)]. When $\Phi > \Phi_{cr}$, on the other hand, Si migrates in the opposite direction and stresses increase monotonically after the initial fast buildup. For $5 < \Phi < 40$, C^{Si} / C_0^{Si} evolves towards a Φ-dependent value of $C_{t>>\tau^{Si}}^{Si} / C_0^{Si}$. The difference between the center and surface values of $C_{t>>\tau^{Si}}^{Si} / C_0^{Si}$ is larger when Φ is smaller. The peak values of stresses are higher at lower Φ, i.e., the stress relaxation due to Si migration is more significant when the thermodynamic factor is lower (or the host and guest are less likely to chemically mix).

Interestingly, although stresses evolve significantly differently for $\Phi > \Phi_{cr}$ and $\Phi < \Phi_{cr}$, they all converge to the same values [Fig. 4.16(b) and (d)] at sufficiently long times. The similar convergence behavior has also been seen in Fig. 4.15(b) and (d). A comparison between Fig. 4.16(b) and (d) with Fig. 4.15(b) and (d) reveals that the long-term stress limits are quite universal, regardless of the values of Φ and D^{Si} / D^{Li}.

An analysis provides useful insight. As the distribution of C^{Si} approaches the steady-state, the silicon flux vanishes, i.e.,

$$\mathbf{J}^{Si} \approx 0 \text{, at } t >> \tau^{Si} . \tag{4-38}$$

Equations (2-42) and (4-38) lead to

$$\Phi \nabla_{\mathrm{X}} x^{Si}_{t>>\tau^{Si}} - \frac{x^{Si}_{t>>\tau^{Si}} \Omega^{Si(SF)}}{k_B \theta} \nabla_{\mathrm{X}} \sigma_m^{t>>\tau^{Si}} \approx 0 \text{, at } t >> \tau^{Si} . \tag{4-39}$$

This equation is independent of D^{Si} as it concerns the steady state solution of x^{Si} for $t >> \tau^{Si}$. Equation (4-39) shows that x^{Si}, hence C^{Si}, for $t >> \tau^{Si}$ does depend on the value of Φ, providing a direct proof for what is seen in Fig. 4.16(a). On the other hand, since the spatial gradient $\nabla C^{Li}\left(r, t\right)$ remains approximately a constant (the C^{Li} profile “shifts” upward without changing its shape) at $t >> \tau^{Li}$ [43],

$$\nabla_{\mathrm{X}} \mathbf{J}^{Li} = -\frac{\partial C^{Li}}{\partial t} = -\frac{\xi_{\max} C_0^{Si}}{T_0} = \text{constant, at } t >> \tau^{Li} , \tag{4-40}$$

where $\xi_{\max} C_0^{Si}$ is the Li concentration at the fully charged state and T_0 is the total galvanostatic charging time to attain full charge. If high-order terms are neglected, equations (4-40) and (2-42) lead to

$$D^{Li} \nabla_{\mathrm{X}} \cdot \left[-\Phi \nabla_{\mathrm{X}} x^{Li} + \frac{\Omega^{Li(SF)}}{k_B \theta} x^{Li} \nabla_{\mathrm{X}} \sigma_m \right] = \text{constant}, \text{ at } t >> \tau^{Li}. \qquad (4\text{-}41)$$

Equations (4-39) and (4-41) and the fact that $\tau^{Si} > \tau^{Li}$ combine to give

$$D^{Li} \nabla_{\mathrm{X}} \cdot \left[-\Phi \nabla_{\mathrm{X}} \left(x^{Li} + x^{Si} \right) + \left(\frac{\Omega^{Li(SF)} x^{Li}}{k_B \theta} + \frac{\Omega^{Si(SF)} x^{Si}}{k_B \theta} \right) \nabla_{\mathrm{X}} \sigma_m \right] = \text{const}, \text{ at } t >> \tau^{Si}. \qquad (4\text{-}42)$$

Since $\nabla_{\mathrm{X}} \left(x^{Li} + x^{Si} \right) = 0$, the above leads to a Φ–independent equation for σ_m in the form of

$$D^{Li} \nabla_{\mathrm{X}} \cdot \left[\left(\frac{\Omega^{Li(SF)} x^{Li}}{k_B \theta} + \frac{\Omega^{Si(SF)} x^{Si}}{k_B \theta} \right) \nabla_{\mathrm{X}} \sigma_m \right] = \text{constant}, \text{ at } t >> \tau^{Si}. \qquad (4\text{-}43)$$

Equations (4-39) and (4-43) indicate that the steady-state hydrostatic stress depends on neither D^{Si} / D^{Li} nor Φ. By extension via eqns. (2-31), (2-34) and (2-36), all stress components at the steady-state are independent of D^{Si} / D^{Li} and Φ, as long as stressing is entirely due to concentration inhomogeneity and no external mechanical load is applied, as is the case of the free-standing NW analyzed here. It is important to note that the peak values of the stresses do depend on Φ, as Fig. 4.16 shows. Also, the relaxation time needed for the solutions to converge to the steady-state depends on D^{Si}/D^{Li}. Again, for $\Phi = 10$ and $D^{Si}/D^{Li} = 0.02$ the stress reduction from the level without Si migration can amount to 20%. Even for the small diffusivity ratio of $D^{Si}/D^{Li} = 0.005$, the host-diffusion-induced stress relaxation is non-negligible[Fig. 4.15 (b) and (d)]. Therefore, account should be taken for host migration in the analyses of Li/Si electrodes.

4.3.3. Conclusions

This section focuses on the effects of host migration on the relaxation of stress and changes in the concentrations of both the host and guest species. It is found that diffusion of the host atoms can have a significant impact on stress, primarily because of the chemical interactions between the species and the effect of stress gradient on interdiffusion. In particular, under conditions of pure elastic deformation the diffusion of Si atoms can cause stress reductions up to 20% with the modest diffusivity ratio of $D^{Si}/D^{Li} = 1/50$ ($D^{Li} = 100$ nm^2/s and $D^{Si} = 2$ nm^2/s). For amorphous Li/Si alloys, the mechanical driving force dominates the chemical driving force, resulting in the migration of Si in the direction of the gradient of the hydrostatic stress $\nabla\sigma_m$ or from the surface to the center of cylindrical electrodes. The analysis has also shown what the behavior would be for alloys with (perhaps unrealistically) high thermodynamic factors. The results indicate that the effect of interdiffusion on stress relaxation can be important even when the stress levels are below the yield threshold of the material.

The migrations of the host and guest introduce two time scales. The time scale for host migration is much longer than the time scale for guest migration, allowing the distribution of guest concentration to reach its own steady state which is slowly modulated by other factors, especially the migration of the host. The time scale for host migration determines the rate at which the ultimate steady state of host concentration and all other field quantities are attained. The distribution of Si concentration is determined by the thermodynamic factor which measures the tendency for the host and guest to chemically mix, but the steady-state stress distribution depends on neither D^{Si} / D^{Li} nor the thermodynamic factor.

Finite diffusivity values of host atoms may have further implications besides the relaxation of stresses. For example, in Li/Si and Li/Ge nano-electrodes, cycling-induced formation of nano-pores indicates that the host material has been irreversibly moved away from the voided regions [5, 80]. If reversible expansion and elastic deformation were the only mechanisms for material deformation, the nano-pores would not form because the host network must revert back to its original configuration upon unloading. Two mechanisms have been proposed to account for the irreversible migration of host atoms. The first is inelastic flow (a form of continuous convection) driven by deviatoric stresses during which material flows in the normal direction of the nucleated pore, leading to void enlargement [5]. The second mechanism is vacancy aggregation during selective dealloying, which involves diffusive migration of host atoms and allows nucleated voids to coalesce and grow [80]. Either or both mechanisms might be relevant, their relative significance depends on the specific material system. With minor adaptation, the continuum framework developed here can be used to delineate the influences of these mechanisms on void development under various conditions.

5. Coupled mechano-diffusional driving forces for fracture

The fact that lithiated Li/Si deforms plastically (section 2.1.3) indicates that elastic-plastic fracture mechanics, instead of linear elastic fracture mechanics (LEFM), should be used to characterize failure. What complicates the problem is the fact that the distribution of Li, which gives rise to stresses, is in turn affected by the stress state [16, 93, 95]. When a crack is mechanically loaded, Li ions would accumulate in front of the crack tip, in a fashion similar to that seen hydrogen embrittlement problems [49, 53]. This accumulation of Li ions at the crack tip can have profound implications on the driving forces for fracture.

Many models have been proposed to characterize the fracture behavior in Li-ion battery electrodes (see the review in section 1.2). Recently, Ryu et al. [53] proposed a framework for calculating the energy release rate J for cracks in Si nanowire electrodes and used the framework to study the size dependence of fracture. This theory relies on an "effective diffusivity" D_{eff} into which the effect of stress on diffusion is lumped. Such an effective diffusivity is only applicable to linear elastic problems. Specifically, when a material deforms plastically diffusion is no longer governed by D_{eff} and the overall diffusion kinetics depends on the nature of mechanical constraints as well as other factors [44]. Even in the elastic regime, calculations based on D_{eff} can only capture stress-induced enhancement to diffusion [43] in regions far from the crack tip but cannot capture the trapping of Li ions at the crack tip [49]. To correctly account for the underlying processes responsible for fracture by including Li trapping and plasticity, a fully-coupled theory is needed to assess the energy release rate.

In this chapter, a fully-coupled theory is developed and used to analyze the coupled mechano-diffusional driving forces for fracture in electrode materials. The analyses take advantage of a mixed finite element framework [18, 46]. We first formulate a *J*-integral for coupled mechanical deformation and mass diffusion processes as a measure for the driving forces for crack growth. By treating the crack tip as a separate thermodynamic system, the formulation entails detailed account of balances of mass and energy and evolution of entropy. All relevant energy forms that may contribute to fracture are explicitly tracked. It is found that the standard form of *J*-integral for energy release rate is no longer path-independent when coupled mechano-diffusion driving forces are present. Instead, an area integral similar to those in hygrothermal [121] and dynamic [122-124] problems must be included. A numerical scheme for implementing this path-independent formulation through finite element simulations is also given.

The numerical study based on the framework is carried out in a progressive manner, with increasing complexity in each step. In section 5.4, we first consider the linear elastic case with concentration-independent properties, so that the near-tip stress fields and the energy release rate can be compared with those given by purely mechanical LEFM. It is found that stress-induced lithium redistribution significantly affects energy release, but has no effect on in-plane stress fields and hence the stress intensity factor K_{I}. The implication of such a dichotomy is discussed by drawing an analogy to the difference between plane-strain and plane-stress situations in LEFM.

The next step in the analyses (section 5.5.1) assumes a finite yield stress so that the material can deform plastically. This scenario involves elasto-plastic deformation with concentration-independent elastic properties and yield stress. The calculation focuses on a surface crack in a thin-film electrode. Depending on whether the electrode yields globally, two regimes of response can be identified. Before global yielding, the energy release rate is governed by an effective crack length which is analogous to that proposed by Irwin. After the global yielding threshold, however, it is found that plastic deformation significantly reduces the energy release rate and softer materials generally have much lower energy release rate levels.

Finally in section 5.5.2, the effect of lithiation-induced-softening on fracture tendency is added. The calculations consider deformation/diffusion coupling, plastic flow, and lithiation-induced material softening through decreases in the elastic modulus and yield stress as Li concentration increases. The analyses lead to a design map for the configuration and operation of thin-film Li-Si electrodes.

This chapter is based on the research published in ref. [39].

5.1. Theoretical framework

We consider the energy release rate for fracture in a solid electrode with full diffusion-deformation coupling. The material, which is composed of two chemical species: host (denoted as *H*) and guest (lithium), is assumed to be highly conductive so that the whole electrode is at the same electric potential. The electrode is assumed to be fully amorphized from the beginning so that phase separation due to crystalline/amorphous transition does not need to be considered. During charge/discharge, lithium atoms diffuse, while the host atoms are assumed to undergo convection but not diffusion for simplicity [18].

The diffusion-deformation coupling is governed by the constitutive laws outlined in chapter 2 and comprises of two interdependent aspects. The first aspect, the effect of diffusion-induced stress (DIS), arises due to a $\dot{C}^{Li}$-dependent term in the constitutive relationship between $\mathbf{D}$ and $\overset{\circ}{\boldsymbol{\sigma}}$ [cf. Eqs. (2-44) and (2-45)]. The second aspect, the effect of mechanical driving forces on diffusion, is embodied by a stress-driven term $\mathbf{J}^{Li,mech}$ in the total Lagrangian flux $\mathbf{J}^{Li}$ of lithium [cf. Eq. (2-40)]. These two aspects, together with the conservation laws of mass [Eq. (2-4)] and momentum [Eq. (2-5)], govern the material response in a solid electrode during charge and discharge.

Following the simplifying assumptions in 4.2.1, we adopt the ideal-solution chemical potential of

$$\mu_{SF}^{Li} = \mu_{*}^{Li} + k\theta \ln \frac{\xi}{\xi_{\max} - \xi}, \tag{5-1}$$

and the composition-dependent diffusivity $D^{Li} = D^{Li}\left(\xi\right)$ in the form of

$$D^{Li} = D_0^{Li}\left(1 - \xi / \xi_{\max}\right) = D_0^{Li}\left(1 - C^{Li} / C_{\max}^{Li}\right). \tag{5-2}$$

Combining Eqs. (2-40), (5-1), and (5-2) leads to the lithium flux of

$$
\begin{aligned}
&J_K^{Li} = J_K^{Li,chem} + J_K^{Li,mech}, \text{ with} \\
&J_K^{Li,chem} = -D_0^{Li} f_{Ki} f_{Ji} \frac{\partial C^{Li}}{\partial X_J} \quad \text{and} \\
&J_K^{Li,mech} = \frac{D_0^{Li}\left(1 - C^{Li} / C_{\max}^{Li}\right)}{k_B \theta} f_{Ki} f_{Ji} C^{Li} \frac{\partial\left[\Omega^{Li(SF)} \sigma_m\right]}{\partial X_J},
\end{aligned}
\tag{5-3}
$$

where $J_K^{Li,chem}$ and $J_K^{Li,mech}$ are contributions due to chemical interaction and mechanical driving force, respectively. Again, according to Purkayastha and McMeeking [96], the main advantage of Eqs. (5-1) and (5-2) is that it correctly captures the fact that the stress-gradient-driven diffusion flux $J_K^{Li,mech}$ [cf. Eqn. (5-3)] vanishes at the charging limits of $\xi = 0$ and $\xi = \xi_{\max}$.

The consideration of the energy release rate (*J*) for fracture is based on an account of the balance of mechanical work in a cracked body [123]. For electrodes whose response is affected by diffusion-deformation coupling, care must be taken because mechanical energy is no longer the only energy source at work. Specifically, chemical energy which drives the mixing between Li and host may also constitute a significant contribution to the overall energy balance. Such coupled driving forces for fracture in electrode materials are similar to those in hygro-thermal systems. Chen [121] proposed a generalized contour integral method to evaluate the latter. The method, however, is path-dependent and requires infinitesimal contours near the crack tip for accurate evaluation.

In this section, we use non-equilibrium thermodynamics to develop a path-independent *J*-integral for the coupled mechano-diffusional driving forces for fracture in electrode materials that undergo large elasto-plastic deformations. The analysis treats the crack tip as a separate thermodynamic system, thereby allowing a systematic account of the balance of mass and energy and the production of entropy.

5.1.1. Energy balance and entropy production

The analysis of energy release rate under full diffusion-deformation coupling is based on accounts of energy and entropy. For any material point in the continuum body, the first law of thermodynamics [125] requires that

$$\dot{e} = \nabla_{\mathbf{X}} \cdot \left(\boldsymbol{\sigma}^{PK1} \cdot \mathbf{v} - \mathbf{J}^{q} - u^{Li} \mathbf{J}^{Li} \right), \tag{5-4}$$

where e is the internal energy per unit reference volume, $\mathbf{v} = d\mathbf{x}/dt\big|_{\mathbf{X}}$ is particle velocity, $\boldsymbol{\sigma}^{PK1} = \det\left(\mathbf{F}\right)\mathbf{F}^{-1} \cdot \boldsymbol{\sigma}$ is the first Piola-Kirchhoff stress, and $u^{Li} \equiv \left(\partial e / \partial C^{Li}\right)_T$ is the partial atomic energy of Li. $\mathbf{J}^{q}$ and $\mathbf{J}^{Li}$ are the heat flux and Li atom flux, respectively; both measured in the reference configuration. In writing Eq. (5-4), we have assumed that there is no external volumetric heat source. Under this condition, the 2nd law of thermodynamics can be stated as [125]

$$\begin{cases} \Sigma = \dot{\eta} + \nabla_{\mathbf{X}} \cdot \mathbf{J}^{\eta} \geq 0, \text{ where} \\ \mathbf{J}^{\eta} = \dfrac{\mathbf{J}^{q}}{\theta} + \dfrac{\left(u^{Li} - \mu^{Li}\right)\mathbf{J}^{Li}}{\theta}. \end{cases} \tag{5-5}$$

Here, η and $\mathbf{J}^{\eta}$ are the Lagrangian density and flux of entropy, respectively; θ is temperature; and Σ is the rate of entropy production per unit reference volume. In this study, isothermal conditions are assumed to prevail [i.e., $\theta = \theta\left(\mathbf{X}, t\right) = \text{constant}$], therefore

$$\Sigma = \dot{\eta} + \frac{1}{\theta} \nabla_{\mathbf{X}} \cdot \left[\mathbf{J}^{q} + \left(u^{Li} - \mu^{Li} \right) \mathbf{J}^{Li} \right] \geq 0. \tag{5-6}$$

The entropy production rate Σ phenomenologically characterizes the irreversible nature of the processes in the continuum. For materials that deform plastically, Σ can be identified as the sum of Σ^{P} (which is due to plastic flow) and Σ^{NP} (which is due to dissipation mechanisms other than plastic deformation, e.g. diffusion), i.e.,

$$\left. \begin{aligned} &\Sigma = \Sigma^{P} + \Sigma^{NP}, \\ &\Sigma^{P} = \frac{\det\left(\mathbf{F}\right)}{\theta} \boldsymbol{\sigma} : \mathbf{D}^{P} \geq 0, \text{ and} \\ &\Sigma^{NP} \geq 0. \end{aligned} \right\} \tag{5-7}$$

5.1.2. The crack tip subsystem

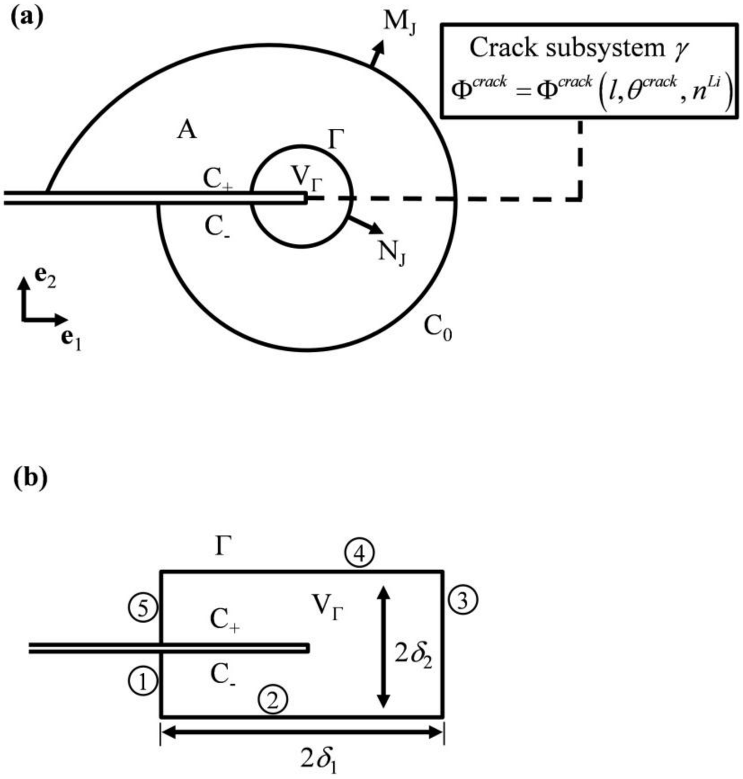

Fig. 5.1 Energy balance at the crack tip, reckoned in the Lagrangian configuration. (a) Domain A is enclosed by Γ *and* $C = C_- + C_0 + C_+$. N_J *and* M_J *are unit vectors normal to* Γ *and* C_0, *respectively.* V_Γ *is the domain enclosed by* Γ, C_- *and* C_+. *The infinitesimal region* V_Γ *exchanges energy and entropy with the crack subsystem which is characterized by its free energy* Φ^{crack}. *(b) A special type of contour* Γ *with rectangular shape.*

Following Moran and Shih [126, 127] and Freund [128], we consider a 2-D body in the $(\mathbf{e}_1, \mathbf{e}_2)$ plane with a crack extending along the $\mathbf{e}_1$ direction, as illustrated in Fig. 5.1(a). At time *t*, the crack has length $l = l(t)$ in the Lagrangian configuration. The crack tip, which propagates at speed $\dot{l}$ in the reference configuration, can be isolated using a small Lagrangian contour Γ which translates along with the crack tip. The nominal out-of-plane thickness (i.e., nominal thickness along $\mathbf{e}_3$) of the 2-D body, also measured in the reference configuration, is denoted as d^{crack}.

Consider a larger contour C_0 which is fixed with respect to the material. There is no singularity in domain A bounded by Γ, C_0 and the two crack surfaces C_- and C_+. In the crack-tip domain V_Γ bounded by Γ, C_- and C_+, however, singularity exists. We treat this singular point in V_Γ as a stand-alone thermodynamic subsystem γ which can exchange mass, energy and entropy with the surrounding continuum body. The Helmholtz free energy of this subsystem per unit out-of-plane thickness d^{crack} is assumed to take the form of

$$\Phi^{crack} = \Phi^{crack}\left(l, \theta^{crack}, n^{Li}\right), \tag{5-8}$$

where θ^{crack} is the temperature and n^{Li} is the amount of Li per unit d^{crack}. It turns out that Eq. (5-8) completely characterizes the thermodynamic properties of the crack subsystem. Specifically, the surface energy per unit crack area (γ), the entropy per unit out-of-plane thickness (S^{crack}), the chemical potential for Li $\left(\mu^{Li,crack}\right)$ and the internal energy per unit out-of-plane thickness $\left(U^{crack}\right)$ can all be uniquely determined via Φ^{crack} as

$$\begin{cases} \gamma = \dfrac{1}{2}\dfrac{\partial \Phi_{crack}}{\partial l} \\ S^{crack} = -\dfrac{\partial \Phi_{crack}}{\partial \theta}, \\ \mu^{Li,crack} = \dfrac{\partial \Phi^{crack}}{\partial n^{Li,crack}}, \text{ and} \\ U^{crack} = \Phi^{crack} + S^{crack}\theta^{crack}, \end{cases} \tag{5-9}$$

respectively. Since isothermal conditions are assumed, temperature is uniform in the continuum domain and the crack subsystem γ is in thermal equilibrium with its surrounding material in V_Γ, i.e.

$$\theta^{crack} = \theta\left(\mathbf{X},t\right) = \text{const.} \tag{5-10}$$

Under this assumption, the incremental form of Eq. (5-8) can be simplified with the help of Eq. (5-9) into

$$\dot{\Phi}^{crack} = 2\gamma\dot{l} + \mu^{Li,crack}\dot{n}^{Li,crack}. \tag{5-11}$$

5.1.3. Energy release rate

Without loss of generality, we assume that γ can exchange mass, energy and entropy with the continuum body (domain A) only through V_Γ. In other words, we neglect any direct mass, energy and entropy exchange between γ and A (one possible mechanism for such direct exchange is surface adsorption on C_- and C_+). Under this assumption, the balances of mass, energy and entropy for the combined system of γ and V_Γ (denoted as $\gamma+\mathrm{V}_\Gamma$) require that

$$\begin{cases} \text{mass:} \quad \dot{n}^{G,crack} + \dfrac{d}{dt}\displaystyle\int_{\mathrm{V}_\Gamma} C^{Li} dA_0 = -\int_\Gamma J_J^{Li} N_J d\Gamma_0 + \int_\Gamma C^{Li}\dot{l}\delta_{1J} N_J d\Gamma_0, \\ \text{energy:} \quad \dot{U}^{crack} + \dfrac{d}{dt}\displaystyle\int_{\mathrm{V}_\Gamma} e dA_0 = \int_\Gamma \left[\sigma_{Ji}^{PK1} v_i - J_J^q - u^{Li} J_J^{Li} + e\dot{l}\delta_{1J}\right] N_J d\Gamma_0, \\ \text{entropy:} \quad \dot{S}^{crack} + \dfrac{d}{dt}\displaystyle\int_{\mathrm{V}_\Gamma} \eta dA_0 = \Sigma^{crack} + \int_{\mathrm{V}_\Gamma} \Sigma dA_0 - \int_\Gamma \left(\dfrac{J_J^q + \left(u^{Li} - \mu^{Li}\right) J_J^{Li}}{\theta} + \eta\dot{l}\delta_{1J} \right) N_J d\Gamma_0. \end{cases} \tag{5-12}$$

Here, $\int_{\mathrm{V}_\Gamma}(\bullet)\,dA_0$ stands for area integral over the 2D Lagrangian domain V_Γ, while $\int_\Gamma(\bullet)\,d\Gamma_0$ stands for path integral along the 2D contour Γ. The area element dA_0 and line segment $d\Gamma_0$ are both measured in the reference configuration. $\Sigma^{crack} \geq 0$ is the entropy production rate (per unit d^{crack}), which can be due to dissipation inside γ or dissipation associated with interactions between γ and V_Γ. In the derivation of Eq. (5-12), use has been made of the Reynold transport theorem on the local forms of Eqs. (2-4), (5-4) and (5-5).

Combining the last two equations of Eq. (5-12) with Eq. (5-9) under isothermal conditions gives

$$\begin{aligned}&\dot{\Phi} + \frac{d}{dt}\int_{\mathrm{V}_\Gamma} \phi\, dA_0 = \\ &\int_\Gamma \sigma^{PK1}_{Ji} v_i N_J\, d\Gamma_0 + \int_\Gamma \phi \dot{l} \delta_{1J} N_J\, d\Gamma_0 - \int_\Gamma \mu^{Li} \mathbf{J}^{Li} \cdot \mathbf{N}\, d\Gamma_0 - \theta\left[\Sigma^{crack} + \int_{\mathrm{V}_\Gamma} \Sigma\, dA_0\right],\end{aligned} \tag{5-13}$$

where $\phi = \varepsilon - \eta\theta$ is the Helmholtz free energy of the continuum per unit reference volume. Again, $\Sigma^{crack} \geq 0$ and $\Sigma \geq 0$ here, according to the 2nd law of thermodynamics.

Equation (5-13) embodies the balance that accounts for the transfer and dissipation of Helmholtz free energy around the crack tip. The significance of its terms can be explained as follows. The left hand side, $\dot{\Phi} + (d/dt)\int_{\mathrm{V}_\Gamma} \phi\, dA_0$, is the time rate of the total Helmholtz free energy in the combined system $\gamma + \mathrm{V}_\Gamma$. This system comprises of everything enclosed by the moving boundary Γ, including the singularity point. The four terms on the right hand side are, respectively, the rates of the mechanical work done by domain A to $\gamma + \mathrm{V}_\Gamma$ (1st term), the free energy swept into $\gamma + \mathrm{V}_\Gamma$ by the moving boundary Γ (2nd term), the free energy conveyed into $\gamma + \mathrm{V}_\Gamma$ by mass flux (3rd term), and the loss of available free energy in $\gamma + \mathrm{V}_\Gamma$ due to irreversible dissipation (4th term). Here, the shape of Γ is arbitrary and, except Eq. (5-8), no specific assumptions on material constitutive behavior are made in the derivation of Eq. (5-13).

Note that Eq. (5-13) accounts for different dissipation mechanisms in the continuum, including inelastic flow [e.g., Σ^P in Eq. (5-7)] and mass transport [which can be lumped into Σ^{NP} in Eq. (5-7)]. The only requirement is that the 2nd law of thermodynamics is satisfied such that $\Sigma^{crack} \geq 0$ and $\Sigma \geq 0$. Now, consider the specific constitutive response described in Chapter 2, in the limit that Γ shrinks to the crack tip. For the form of ϕ given by Eqs. (2-32), (2-35), (2-38) and (4-16), the singularity satisfies the condition

$$\lim_{\Gamma \to 0}\left(\frac{d}{dt}\int_{\mathrm{V}_\Gamma} \phi \, dA_0\right) = 0. \tag{5-14}$$

This is true as long as $\alpha < 1$ for the asymptotic behavior of $\sigma_{ij} \sim 1/r^{\alpha}$ when $r \to 0$, where r is the radial distance measured from the crack tip. On the other hand, chemical potential μ^{Li} of Eq. (2-38) and (5-1) [and even the $\mu_{SF}^{Li} = \mu_{SF}^{Li}(\xi)$ fitted from OCP data] ensures that $0 \leq \xi \leq \xi_{\max}$ even when $\sigma_m \sim 1/r^n$ goes to infinity as $r \to 0$. The fact that ξ (and hence C^{Li}) is continuous and bounded leads to

$$\begin{cases} \lim\limits_{\Gamma \to 0}\left(\dfrac{d}{dt}\displaystyle\int_{\mathrm{V}_\Gamma} C^{Li} \, dA_0\right) = 0, \text{ and} \\ \lim\limits_{\Gamma \to 0}\left(\displaystyle\int_{\Gamma} C^{Li} \dot{l} \delta_{1J} N_J \, d\Gamma_0\right) = 0. \end{cases} \tag{5-15}$$

Mass conservation near the crack tip [cf. Eq. (5-12)] when $\Gamma \to 0$, therefore, takes the form

$$\dot{n}^{Li,crack} = -\lim_{\Gamma \to 0} \int_{\Gamma} J_J^{Li} N_J \, d\Gamma_0, \tag{5-16}$$

i.e., Li atoms that transport into $\gamma + \mathrm{V}_\Gamma$ through Γ are predominantly stored in the crack tip subsystem γ if $\Gamma \to 0$.

Generally speaking, lithium chemical potential μ^{Li} in V_Γ is position-dependent and not necessarily equal to $\mu^{Li,crack}$ in the γ subsystem. When $\mu^{Li} \neq \mu^{Li,crack}$, the transport of Li into γ (at the rate of $\dot{n}^{Li,crack}$) is dissipative and can be characterized by an positive-definite dissipation rate of $\lim_{\Gamma \to 0} \left[\dot{n}^{Li,crack} \left(\mu^{Li} - \mu^{Li,crack} \right) \right]$. For simplicity, such an dissipation mechanism is not considered in this study, i.e., it is assumed that γ is in chemical equilibrium with its immediate surroundings such that

$$\mu^{Li,crack} = \lim_{\Gamma \to 0} \mu^{Li}. \tag{5-17}$$

This assumption [Eq. (5-17)] and Eq. (5-16) immediately lead to

$$\lim_{\Gamma \to 0} \int_{\Gamma} \mu^{Li} \mathbf{J}^{Li} \cdot \mathbf{N} \, d\Gamma_0 = -\mu^{Li,crack} \dot{n}^{Li,crack}. \tag{5-18}$$

Combining Eqs. (5-13), (5-14), (5-18) and (5-11), therefore, yields

$$\lim_{\Gamma \to 0} \int_{\Gamma} \left[\sigma_{Ji}^{PK1} v_i + \phi \dot{l} \delta_{1J} \right] N_J \, d\Gamma_0 = 2\gamma \dot{l} + \theta \left[\Sigma^{crack} + \lim_{\Gamma \to 0} \int_{\mathrm{V}_\Gamma} \Sigma \, dA_0 \right]. \tag{5-19}$$

The left hand side of Eq. (5-19) is the time rate at which energy is imparted into the crack tip region during crack growth. Under the conditions of local steady state, $v_i \sim -\dot{l}\left(\partial u_i / \partial X_1\right)$. The driving force for crack growth, namely energy provided per unit new crack area created, is therefore given by

$$J \equiv \lim_{\Gamma\to 0}\frac{\int_\Gamma\left[\sigma_{Ji}^{PK1}v_i+\phi\dot{l}\delta_{1J}\right]N_J d\Gamma_0}{\dot{l}} = \lim_{\Gamma\to 0}\int_\Gamma\left[\phi\delta_{1J}-\sigma_{Ji}^{PK1}\frac{\partial u_i}{\partial X_1}\right]N_J d\Gamma_0. \qquad (5\text{-}20)$$

The right hand side of Eq. (5-19), on the other hand, comprises two parts. The first part $2\gamma\dot{l}$ corresponds to the increase of free energy in the subsystem γ, while the second part $\theta\left[\Sigma^{crack}+\lim_{\Gamma\to 0}\int_{V_\Gamma}\Sigma dA_0\right]$ characterizes the free energy loss due to dissipation. As for any irreversible processes, this dissipation is generally history-dependent, in the sense that the combined resistance

$$J_{CR} \equiv 2\gamma + \lim_{\Gamma\to 0}\frac{\theta\left[\Sigma^{crack}+\lim_{\Gamma\to 0}\int_{V_\Gamma}\Sigma dA_0\right]}{\dot{l}} \qquad (5\text{-}21)$$

depends on the history of crack growth even for the same thermodynamic state $\left(l,\theta^{crack},n^{Li}\right)$ of the crack tip subsystem γ. For simplicity, the standard assumption of fracture mechanics that $J_{CR}=J_{CR}\left(l\right)$ is used here, with the understanding that J_{CR} may also depend on the state of charge (i.e., Li concentration) in the electrode. Under this assumption, the critical condition for isothermal quasi-static crack growth accounting for deformation-diffusion coupling can be stated as

$$J = J_{CR} \geq 2\gamma. \tag{5-22}$$

Equation (5-22) is the Griffith condition for fracture growth when diffusion-deformation two-way coupling is present. It should be noted that as a fracture mechanics criterion, the Griffith condition generally does not apply to fatigue crack growth and the failure of secondary battery electrodes can occur under static or cyclic loads (charge-discharge). However, for an electrode to last, it has to survive the first few cycles of loading during which fracture is governed by Eq. (5-22). As will be shown in the numerical analysis in sections 5.4 and 5.5, even this requirement alone puts significant constraints on the design of battery electrodes. We, therefore, use Eq. (5-22) as the criterion for battery failure in this study, and leave the discussion of cyclic fatigue to future studies. It should be also noted that even for situations in which fatigue is important, analyses such as the Paris-law generally require the calculation of fracture driving force (in the form of K_I or J). The fully-coupled theory in this study can, therefore, also be regarded as an essential part of future models for cyclic failure in battery electrodes.

5.1.4. Path-independent integral for energy release rate

The specific form of Eq. (5-20) is general but inconvenient for the numerical evaluation of energy release rate because the integral

$$J^{*}(\Gamma) \equiv \int_{\Gamma} \left[\phi \delta_{1J} - \sigma_{Ji}^{PK1} \frac{\partial u_i}{\partial X_1} \right] N_J \, d\Gamma_0 \tag{5-23}$$

is path-dependent for coupled diffusion/deformation problems. Indeed, for any continuum domain Ω bound by $\partial\Omega$,

$$J^*\left(\partial\Omega\right) = -\int_{\partial\Omega} w^P \delta_{1J} N_J d\Gamma_0 + \int_\Omega \mu^{Li} \frac{\partial C^{Li}}{\partial X_1} dA_0 , \tag{5-24}$$

where the plastic potential w^P is defined as

$$\begin{cases} w^P \equiv \int_0^t \det\left(\mathbf{F}\right)\boldsymbol{\sigma} : \mathbf{D}^P dt \approx \int_0^t \left(V^{SF}\right)^2 \sigma_{JK}^{PK2} \dot{E}_{JK}^P dt, \text{ where} \\ E_{JK}^P \equiv \frac{1}{2}\left(F_{jJ}^P F_{jK}^P - \delta_{JK}\right). \end{cases} \tag{5-25}$$

Here, $\boldsymbol{\sigma}^{PK2} = \det\left(\mathbf{F}\right)\mathbf{F}^{-1} \cdot \boldsymbol{\sigma} \cdot \mathbf{F}^{-\mathrm{T}}$ is the 2nd Piola-Kirchhoff stress, and $\mathbf{E}^P$ is the Lagrangian strain of plastic deformation. $V^{SF} = \left(J^{SF}\right)^{1/3}$ is isotropic stretch associated with $J^{SF} = \det\left(\mathbf{F}^{SF}\right)$ [cf. Eqn. (2-34)].

To prove Eqn. (5-24), we first note that balance of momentum [Eq. (2-5)] requires that

$$\frac{\partial \sigma_{Ji}^{PK1}}{\partial X_J} = 0. \tag{5-26}$$

Therefore, invoking the divergence theorem on Eq. (5-23) leads to

$$J^*\left(\partial\Omega\right) = \int_\Omega \left[\frac{\partial \phi}{\partial X_1} - \sigma_{Ji}^{PK} \frac{\partial F_{iJ}}{\partial X_1} \right] dA_0. \tag{5-27}$$

The Lee decomposition [Eq. (2-1)] indicates that

$$\frac{\partial F_{iJ}}{\partial X_1} = \frac{\partial F^e_{il}}{\partial X_1} V^{SF} F^P_{lJ} + F^e_{il} V^{SF} \frac{\partial F^P_{lJ}}{\partial X_1} + F_{iJ} \frac{\partial \ln V^{SF}}{\partial X_1}. \tag{5-28}$$

For free energy of the form $\phi = \phi(\mathbf{F}^e, C^{Li}, \theta)$, the 1st Piola-Kirchoff stress and Li chemical potential are, respectively [cf. Eqn. (2-9), (2-13), and (2-14)],

$$\left\{ \begin{aligned} &\sigma^{PK1}_{Kj} = \left.\frac{\partial \phi}{\partial F_{jK}}\right|_{\mathbf{F}^P, C^{Li}, \theta} = \left.\frac{\partial \phi}{\partial F^e_{jk}}\right|_{C^{Li}, \theta} f^P_{Kk} \left(V^{SF}\right)^{-1}, \text{ and} \\ &\mu^{Li} = \left.\frac{\partial \phi}{\partial C^{Li}}\right|_{\mathbf{F}^P, \mathbf{F}, \theta} = \left.\frac{\partial \phi}{\partial C^{Li}}\right|_{\mathbf{F}^e, \theta} - \left.\frac{\partial \phi}{\partial F^e_{ij}}\right|_{C^{Li}, \theta} F^e_{ij} \left.\frac{\partial \ln V^{SF}}{\partial C^{Li}}\right|_{\theta} \\ &\qquad = \left.\frac{\partial \phi}{\partial C^{Li}}\right|_{\mathbf{F}^e, \theta} - F_{jK} \sigma^{PK1}_{Kj} \frac{\partial \ln V^{SF}}{\partial C^{Li}}; \end{aligned} \right. \tag{5-29}$$

where $\mathbf{f}^P = \left(\mathbf{F}^P\right)^{-1}$. Therefore, under isothermal conditions,

$$\begin{aligned} \frac{\partial \phi}{\partial X_1} &= \left.\frac{\partial \phi}{\partial F^e_{ij}}\right|_{C^{Li}} \frac{\partial F_{ij}}{\partial X_1} + \left.\frac{\partial \phi}{\partial C^{Li}}\right|_{\mathbf{F}^e} \frac{\partial C^{Li}}{\partial X_1} \\ &= V^{SF} F^P_{jK} \sigma^{PK1}_{Ki} \frac{\partial F^e_{ij}}{\partial X_1} + \left(\mu^{Li} + F_{jK} \sigma^{PK1}_{Kj} \frac{\partial \ln V^{SF}}{\partial C^{Li}} \right) \frac{\partial C^{Li}}{\partial X_1}. \\ &= V^{SF} F^P_{jK} \sigma^{PK1}_{Ki} \frac{\partial F^e_{ij}}{\partial X_1} + \mu^{Li} \frac{\partial C^{Li}}{\partial X_1} + F_{jK} \sigma^{PK1}_{Kj} \frac{\partial \ln V^{SF}}{\partial X_1} \end{aligned} \tag{5-30}$$

In the derivation of Eq. (5-30), it is assumed that V^{SF} is uniquely determined by current Li concentration [Eq. (2-34)].

Combining Eq. (5-28) and Eq. (5-30) leads to

$$\frac{\partial \phi}{\partial X_1} - \sigma_{Ji}^{PK} \frac{\partial F_{iJ}}{\partial X_1} = \mu^{Li} \frac{\partial C^{Li}}{\partial X_1} - \sigma_{Ji}^{PK1} F_{il}^{e} V^{SF} \frac{\partial F_{lJ}^{P}}{\partial X_1} . \tag{5-31}$$

With the assumption that elastic strains are small (i.e., $F_{ij}^{e} F_{il}^{e} \approx \delta_{jl}$), the second term on the right hand side of Eq. (5-31) can be easily transformed into

$$\sigma_{Ji}^{PK1} F_{il}^{e} V^{SF} \frac{\partial F_{lJ}^{P}}{\partial X_1} \approx \left(V^{SF}\right)^2 \sigma_{JK}^{PK2} \frac{\partial E_{JK}^{P}}{\partial X_1} , \tag{5-32}$$

where $E_{JK}^{P} \equiv \frac{1}{2}\left(F_{jJ}^{P} F_{jK}^{P} - \delta_{JK}\right)$ is the plastic strain. By Eqs. (5-27), (5-31) and (5-32), one obtains

$$J^{*}\left(\partial \Omega\right) = \int_{\Omega} \mu^{Li} \frac{\partial C^{Li}}{\partial X_1} dA_0 - \int_{\Omega} \left(V^{SF}\right)^2 \sigma_{JK}^{PK2} \frac{\partial E_{JK}^{P}}{\partial X_1} dA_0 . \tag{5-33}$$

To proceed further, consider the plastic potential of Eqn. (5-25), and adopt the standard approximation such that

$$\frac{\partial w^{P}}{\partial X_1} \approx \left(V^{SF}\right)^2 \sigma_{JK}^{PK2} \frac{\partial E_{JK}^{P}}{\partial X_1} . \tag{5-34}$$

Substitution of Eq. (5-34) into Eq. (5-33) and the divergence theorem lead to

$$J^{*}\left(\partial \Omega\right) = \int_{\Omega} \mu^{Li} \frac{\partial C^{Li}}{\partial X_1} dA_0 - \int_{\partial \Omega} w^{P} \delta_{1J} N_J d\Gamma_0 , \tag{5-35}$$

and we have proved Eqn. (5-24). The validity of Eq. (5-35) [namely Eqn. (5-24)] mostly depends on how significant the error associated with approximation (5-34) is. The path independency of Eq. (5-40) is therefore less reliable when approximation (5-34) breaks down. Indeed, for cracks in elasto-plastic materials, contours that are very close to the crack tip should not be used [39, 129].

Subtracting Eq. (5-24) from Eq. (5-23) leads to the path-independent integral form of

$$\begin{aligned} J(\Gamma) \equiv & \int_{\Gamma} \left[\phi\delta_{1J} - \sigma_{Ji}^{PK1} \left(\partial u_i / \partial X_1 \right) \right] N_J d\Gamma_0 \\ & - \left(\int_{V_\Gamma} \mu^{Li} \frac{\partial C^{Li}}{\partial X_1} dA_0 - \int_{\Gamma} w^P \delta_{1J} N_J d\Gamma_0 \right). \end{aligned} \tag{5-36}$$

The integral $J(\Gamma)$ is path-independent, in the sense that $J(\partial\Omega)=0$ for the boundary $\partial\Omega$ of any continuum domain Ω. On the other hand, contour Γ in Eq. (5-20) can be of arbitrary shape as long as its size is infinitesimal. To establish a link between Eqns. (5-36) and (5-20), consider the special type of Γ shown in Fig. 5.1 (b). As pointed out by Freund [128], if the rectangular contour is shrunk onto the crack tip by first letting $\delta_2 \to 0$ and then $\delta_1 \to 0$, one has

$$J = \lim_{\delta_1 \to 0} \lim_{\delta_2 \to 0} \int_{\Gamma} \left[\phi\delta_{1J} - \sigma_{Ji}^{PK1} \frac{\partial u_i}{\partial X_1} \right] N_J d\Gamma_0 \ . \tag{5-37}$$

Such rectangular contours are especially convenient because horizontal segments 2 and 4 do not contribute to the integral $\int_{1-2-3-4-5} \dot{w}^P \delta_{1J} N_J d\Gamma_0$ [cf. Fig. 5.1 (b)]. Even if w^P is singular at the crack tip, the plasticity term in Eq. (5-36) still vanishes as long as appropriate limiting process is considered, i.e.

$$\lim_{\delta_1\to 0}\lim_{\delta_2\to 0}\int_{\Gamma} w^P \delta_{1J} N_J \, d\Gamma_0 = 0. \tag{5-38}$$

On the other hand, for domain V_Γ bound by Γ [cf. Fig. 5.1(b)], $\int_{\mathrm{V}_\Gamma} \mu^{Li}\left(\partial C^{Li} / \partial X_1\right) dA_0$ can be evaluated and goes to 0 when $\delta_2 \to 0$ and $\delta_1 \to 0$, i.e.,

$$\lim_{\delta_1\to 0}\lim_{\delta_2\to 0}\int_{\mathrm{V}_\Gamma} \mu^{Li}\left(\partial C^{Li} / \partial X_1\right) dA_0 = 0. \tag{5-39}$$

Combining Eqs. (5-37)-(5-39), therefore, leads to the path-independent *J*-integral for coupled mechano-diffusional driving forces in the form of

$$J = J\left(\Gamma\right) = \int_{\Gamma}\left[\left(\phi + w^P\right)\delta_{1J} - \sigma_{Ji}^{PK1}\frac{\partial u_i}{\partial X_1}\right] N_J \, d\Gamma_0 - \int_{\mathrm{V}_\Gamma} \mu^{Li}\frac{\partial C^{Li}}{\partial X_1} dA_0, \tag{5-40}$$

where Γ is arbitrary.

5.2. Implementation of *J* by using the energy domain integral method

We will use Eqs (5-40) to evaluate energy release rates from numerical results given by finite element simulations. The main advantage of this path-independent form lies in the fact that Γ can be far away from the crack tip region where the numerical evaluation of ϕ, w^P, $\partial u_i / \partial X_1$ and σ_{Ji}^{PK1} is usually more challenging. In this section, we propose a finite element implementation by leveraging the energy domain integral method originally proposed by Shih et al. [130].

Eq. (5-40) is the path-independent form of the energy release rate used in this study for the numerical evaluation of *J*. With Eqs. (2-32), (2-35), (2-38), and some algebra, Eq. (5-40) can be recast into

$$
\begin{aligned}
J = J\left(\Gamma\right) = {} & \int_{\Gamma}\left[\left(w + w^{P}\right)\delta_{1J} - \sigma_{Ji}^{PK1}\left(\partial u_i / \partial X_1\right)\right] N_J \, d\Gamma_0 \\
& - \int_{V_\Gamma}\left(\left.\frac{\partial w}{\partial C^{Li}}\right|_{\mathbf{F}^e,\theta} - \det\left(\mathbf{F}^e\right)\Omega^{Li(SF)}\sigma_m\right)\frac{\partial C^{Li}}{\partial X_1}\, dA_0,
\end{aligned}
\tag{5-41}
$$

where w is the elastic strain energy given by Eq. (2-35). Eqn. (5-41) consists of a contour integral over a finite path and an area integral over a finite domain.

Based on Eq. (5-41),we adopt the method originally proposed by Shih et al. [130] in order to facilitate the computation of $J\left(\Gamma\right)$. For arbitrary contours Γ and C_0 (cf. Fig. 5.1), consider a sufficiently smooth field of $q^* = q^*\left(\mathbf{X}\right)$ such that $q^* = 1$ on Γ and $q^* = 0$ on C_0. Here, Γ is not necessarily infinitesimal. For traction-free crack surfaces C_- and C_+ , the path-independent expression of energy release rate [Eq. (5-41)] can be rewritten as

$$
\begin{aligned}
J = J\left(\Gamma\right) = {} & \int_{C_- + C_0 + C_+ - \Gamma}\left[-\left(w + w^{P}\right)\delta_{1J} + \sigma_{Ji}^{PK1}\left(\partial u_i / \partial X_1\right)\right] q^* N_J \, d\Gamma_0 \\
& - \int_{V_\Gamma}\left(\left.\frac{\partial w}{\partial C^{Li}}\right|_{\mathbf{F}^e,\theta} - \det\left(\mathbf{F}^e\right)\Omega^{Li(SF)}\sigma_m\right)\frac{\partial C^{Li}}{\partial X_1}\, dA_0.
\end{aligned}
\tag{5-42}
$$

Here, $-\Gamma$ stands for contour Γ with the opposite loop direction. Application of the divergence theorem leads to

$$\begin{cases} J = J\left(\Gamma\right) = \int_A q^* \left[-\dfrac{\partial\left(w + w^P\right)}{\partial X_1} + \sigma_{Ji}^{PK1} \dfrac{\partial F_{iJ}}{\partial X_1} \right] dA_0 \\ + \int_A \dfrac{\partial q^*}{\partial X_J} \left[-\left(w + w^P\right)\delta_{1J} + \sigma_{Ji}^{PK} \dfrac{\partial u_i}{\partial X_1} \right] dA_0 \\ - \int_{\mathrm{V}_\Gamma} \left(\left.\dfrac{\partial w}{\partial C^{Li}}\right|_{\mathbf{F}^e,\theta} - \det\left(\mathbf{F}^e\right)\Omega^{Li(SF)}\sigma_m \right) \dfrac{\partial C^{Li}}{\partial X_1} dA_0. \end{cases} \tag{5-43}$$

With Eqs. (2-35)-(2-39) and (5-43),

$$\begin{cases} J = \int_A \dfrac{\partial q^*}{\partial X_J} \left[\sigma_{Ji}^{PK1} \dfrac{\partial u_i}{\partial X_1} - \left(w + w^P\right)\delta_{1J} \right] dA_0 \\ + \int_{\mathrm{V}_\Gamma} \left[\det\left(\mathbf{F}^e\right)\Omega^{Li(SF)}\sigma_m - \left.\dfrac{\partial w}{\partial C^{Li}}\right|_{\mathbf{F}^e,\theta} \right] \dfrac{\partial C^{LI}}{\partial X_1} dA_0 \\ + \int_A q^* \left[\det\left(\mathbf{F}^e\right)\Omega^{Li(SF)}\sigma_m - \left.\dfrac{\partial w}{\partial C^{Li}}\right|_{\mathbf{F}^e,\theta} \right] \dfrac{\partial C^{Li}}{\partial X_1} dA_0. \end{cases} \tag{5-44}$$

Here, Γ and C_0 are arbitrary [cf. Fig. 5.1 (a)) and Γ is not necessarily infinitesimal.

5.3. Model configurations

The analyses carried out in in the following sections concern the energy release rate for stationary cracks. Specifically, the large-deformation, mixed finite element framework of the rate form (cf. Chapter 3) is used to analyze the coupling between diffusion and stress development [18, 46]. Based on numerical solutions obtained, the energy release rate is calculated using the path-independent form in section 5.1. The issues of focus are

1) how does the mechanical driving force for diffusion affect crack-tip fields and energy release rate?

2) how does plasticity affect the energy release rate in the presence of diffusion/deformation coupling? and

3) how does lithiation-induced softening affect fracture and, in turn, battery design?

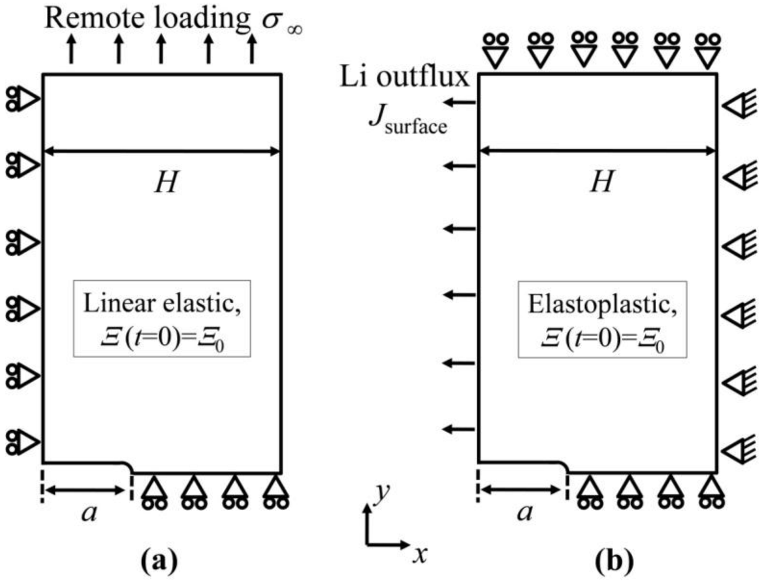

Fig. 5.2(a) A highly-simplified plane-strain system with a center crack in a 2D media, loaded by a remote stress. This configuration will be used to analyze the effect of diffusion/deformation coupling in the LEFM regime. (b) a thin-film electrode with periodic surface pre-cracks, initial homogeneous Li concentration ξ_0*, and zero initial stress undergoing discharge at a constant surface outflux. The pre-crack is modeled as a notch with a small but finite tip radius of* $\rho \ll a$ *for numerical stability.*

To address the first issue, we consider a highly-simplified plane-strain system with a center crack in a 2D media [Fig. 5.2(a)]. Lithiation-induced softening is not considered in this case and the material is assumed to be perfectly elastic. When the crack is loaded by a remotely applied stress σ_∞, the effect of diffusion/deformation coupling can be analyzed, especially in terms of crack-tip fields and energy release rate.

Based on the insights gained from the above LEFM problem, a more realistic case with material inelasticity will be considered to address the second and the third issues. Specifically, a thin-film electrode with surface cracks during delithiation will be considered [Fig. 5.2(b)]. Analyses in this regard will be carried out in two steps. The first step involves constant mechanical properties that are independent of Li concentration (section 5.5.1). After that, the implications of lithiation-induced softening will be analyzed (section 5.5.2).

Depending on the design and material, stresses in an electrode may arise via three mechanisms: (1) Li concentration inhomogeneity due to finite diffusivity, (2) lattice mismatch at phase boundaries, and (3) constraining by external agencies such as substrate or current collector. In order to focus on the effect of deformation/diffusion coupling and lithiation-induced softening on the fracture driving forces, we only consider the third mechanism (mechanical constraint) in this study. To this end, we assume that the initial material (Li/Si in this study) is fully amorphized and that the characteristic loading time T_0 is much longer than the characteristic diffusion time $\tau^{Li} \approx H^2 / D_0^{Li}$ so that the stresses in the electrode are entirely due to external loading [for Fig. 5.2 (a)] or mechanical constraint [for Fig. 5.2(b)]. The insight thus obtained can be easily extended to situations with $\tau^{Li} \sim T_0$, which will not be the focus of this study.

5.4. Linear elastic case

We first consider the linear elastic situation such that the yield stress σ_Y is infinite and Young's modulus E and Poisson ratio ν are Ξ -independent. The geometry of the stress-controlled configuration [cf. Fig. 5.2(a)] used here can be characterized by a single parameter a

which measures the crack length, as long as $H \gg a$. The pre-crack is modeled as a notch with a small but finite tip radius of $\rho \ll a$ for numerical stability. Starting from a stress-free state with homogeneous initial SOC of Ξ_0, the system is loaded by a remote stress of $\sigma_\infty = \left(t / T_0\right) E$ with $\tau^{Li} \ll T_0$. Under the condition of $\tau^{Li} \ll T_0$, the concentration and stress fields, hence the fracture driving forces, do not depend on D_0^{Li} explicitly. Our task is to analyze the effect of mechanical driving force for diffusion on crack-tip fields and the energy release rate.

Table 1 Concentration-independent material parameters for Li/Si used in the LEFM analysis.

Parameter	Symbol	Typical value	Reference/definition
Partial atomic volume of Li	$\Omega^{\text{Li (SF)}}$	14.2 Å^3	[13]
Si concentration in fully-discharged state	C_0^{Si}	49.3 atoms nm^{-3}	[108]
Young's modulus	E	80 GPa	[48]
Diffusivity	D_0^{Li}	10^{-11} cm^2 s^{-1}	[109, 112-114]
Poisson ratio	ν	0.22	[22]
Maximum charging limit of Li$_\xi$Si	$\xi_{\max}$	3.75	[62]
Chemical-to-mechanical partial atomic volume	$\tilde{\Omega}^{\text{CM}}$	0.7	$\Omega^{\text{Li(SF)}} C^{Si}$
Mechanical-to-chemical dimensionless partial atomic volume	$\tilde{\Omega}^{\text{MC}}$	274	$\Omega^{\text{Li(SF)}} E / k\theta$

Four dimensionless parameters can be identified here: the charging limit $\xi_{\max}$, the Poisson's ratio ν, and dimensionless partial atomic volumes $\tilde{\Omega}^{\mathrm{CM}} \equiv \Omega^{\mathrm{Li(SF)}} C^{Si}$ and $\tilde{\Omega}^{\mathrm{MC}} \equiv \Omega^{\mathrm{Li(SF)}} E / k\theta$. The meaning of $\tilde{\Omega}^{\mathrm{CM}}$ is straightforward: it characterizes the volume expansion ratio when Li concentration changes. Specifically, the ratio between the volume at lithiated state $\mathrm{Li}_\xi\mathrm{H}$ and the volume at fully-delithiated state $\mathrm{Li}_0\mathrm{H}$ is $J^{SF}(\xi) = 1 + \xi \tilde{\Omega}^{\mathrm{CM}}$. $\tilde{\Omega}^{\mathrm{CM}}$, therefore, determines the effect of chemical diffusion to mechanical deformation (Chemical-to-Mechanical, CM) when composition changes. To illustrate the significance of $\tilde{\Omega}^{\mathrm{MC}}$, on the other hand, we consider the dimensionless chemical potential $\mu^{Li} / k_B\theta$ which can be easily shown from Eqs. (2-38) and (5-1) to be

$$\frac{\mu^{Li}}{k_B\theta} = \left(\frac{\mu_*^{Li}}{k_B\theta} + \ln \frac{\Xi}{1-\Xi} \right) - \tilde{\Omega}^{\mathrm{MC}} \frac{\sigma_m}{E}. \tag{5-45}$$

The first term of Eq. (5-45) is the chemical contribution to $\mu^{Li} / k_B\theta$, the second term is due to mechanical stresses. Since σ_m / E is proportional to elastic strain $\boldsymbol{\varepsilon}^e$ [cf. Eq. (2-36)], one can immediately conclude from Fick's law [Eq. (2-40) and (5-3)] that $\tilde{\Omega}^{\mathrm{MC}}$ is the parameter which controls the mechanical driving force to chemical diffusion (Mechanical-to-Chemical, MC). Specifically, if $\tilde{\Omega}^{\mathrm{MC}} = 0$ there would be no stress effect on $\mathbf{J}^{Li}$.

The role of $\tilde{\Omega}^{\mathrm{CM}}$ has been widely studied, especially in the context of thermally-induced fracture. The significance of $\tilde{\Omega}^{\mathrm{MC}}$ and associated effect on fracture, however, are still not well-understood. To see how $\tilde{\Omega}^{\mathrm{MC}}$ affects crack-tip fields and energy release rate, we used the typical room-temperature ($\theta = 300\,\mathrm{K}$) values of material parameters for $\mathrm{Li}_\xi\mathrm{Si}$ (H=Si for $\mathrm{Li}_\xi\mathrm{H}$). The discussions compare two scenarios: one with $\tilde{\Omega}^{\mathrm{MC}} = \tilde{\Omega}^{\mathrm{MC}}_{\mathrm{LiSi}}$ as listed in Table 1, and the other with $\tilde{\Omega}^{\mathrm{MC}} = 0$..

5.4.1. In-plane stresses and stress intensity factor

Fig. 5.3(a) shows the redistribution of Li concentration $\Xi = \xi / \xi_{\max}$ when an initially homogeneous electrode (with *a*=500 nm and $\Xi_0 = 0.4$) is loaded by a remote stress of $\sigma_\infty = 0.005E$, under the condition of $\tilde{\Omega}^{\mathrm{MC}} = \tilde{\Omega}^{\mathrm{MC}}_{\mathrm{LiSi}}$. The spatial coordinates are normalized by the crack length *a*. It can be seen that Ξ deviates from the average value $\bar{\Xi} = \Xi_0$ such that $\Delta\Xi \equiv \Xi - \Xi_0 > 0$ in front of the crack tip. This redistribution, driven by the crack-tip hydrostatic stress σ_m, in turn relaxes σ_m [Fig. 5.3(b)], as shown by the much lower σ_m levels for the fully-coupled case ($\tilde{\Omega}^{\mathrm{MC}} = \tilde{\Omega}^{\mathrm{MC}}_{\mathrm{LiSi}}$) than the levels for the purely mechanical case ($\tilde{\Omega}^{\mathrm{MC}} = 0$).

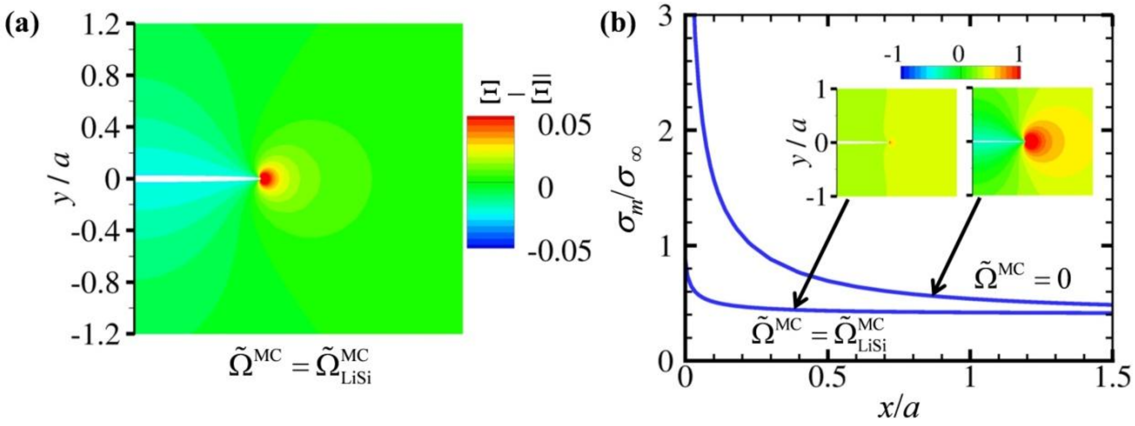

Fig. 5.3. Distributions of Li concentration and hydrostatic stress near the crack tip under a remote stress of $\sigma_\infty = 0.005E$. (a) deviation of concentration from its spatial average when $\tilde{\Omega}^{\mathrm{MC}} = \tilde{\Omega}^{\mathrm{MC}}_{\mathrm{LiSi}}$; (b) normalized hydrostatic stress σ_m / σ_∞ along the y=0 line for the fully-coupled ($\tilde{\Omega}^{\mathrm{MC}} = \tilde{\Omega}^{\mathrm{MC}}_{\mathrm{LiSi}}$) and the purely mechanical ($\tilde{\Omega}^{\mathrm{MC}} = 0$) cases. The inset in (b) shows the corresponding

σ_m / σ_∞ *contours. The length of the center-crack is a=500 nm and the initial SOC is* $\Xi_0 = \bar{\Xi} = 0.4$. *All spatial dimensions are normalized by crack length a.*

Given the dependence of σ_m on $\tilde{\Omega}^{\mathrm{MC}}$, one may conjecture that Li redistribution lowers all components of crack-tip stresses. Quite counter-intuitively, this is not the case. As shown in Fig. Fig. 5.4(a), the in-plane stress components (σ_{xx} and σ_{yy}) are both independent of $\tilde{\Omega}^{\mathrm{MC}}$. The relaxation of σ_m is entirely due to the change in σ_{zz}. Indeed, when $\tilde{\Omega}^{\mathrm{MC}} = 0$ the problem reduces to an elementary plane-strain elasticity problem with $\sigma_{zz} = \nu\left(\sigma_{xx} + \sigma_{yy}\right) > 0$. On the other hand for $\tilde{\Omega}^{\mathrm{MC}} = \tilde{\Omega}^{\mathrm{MC}}_{\mathrm{LiSi}}$, $\sigma_{zz} < 0$ [cf. Fig. 5.4(b)]. Such a tensile to compressive change of σ_{zz} significantly increases the crack-tip von Mises stress σ_{mises} [compare Fig. 5.4(c) and (d)]. The consequence of this increase of σ_{mises} will be discussed further later.

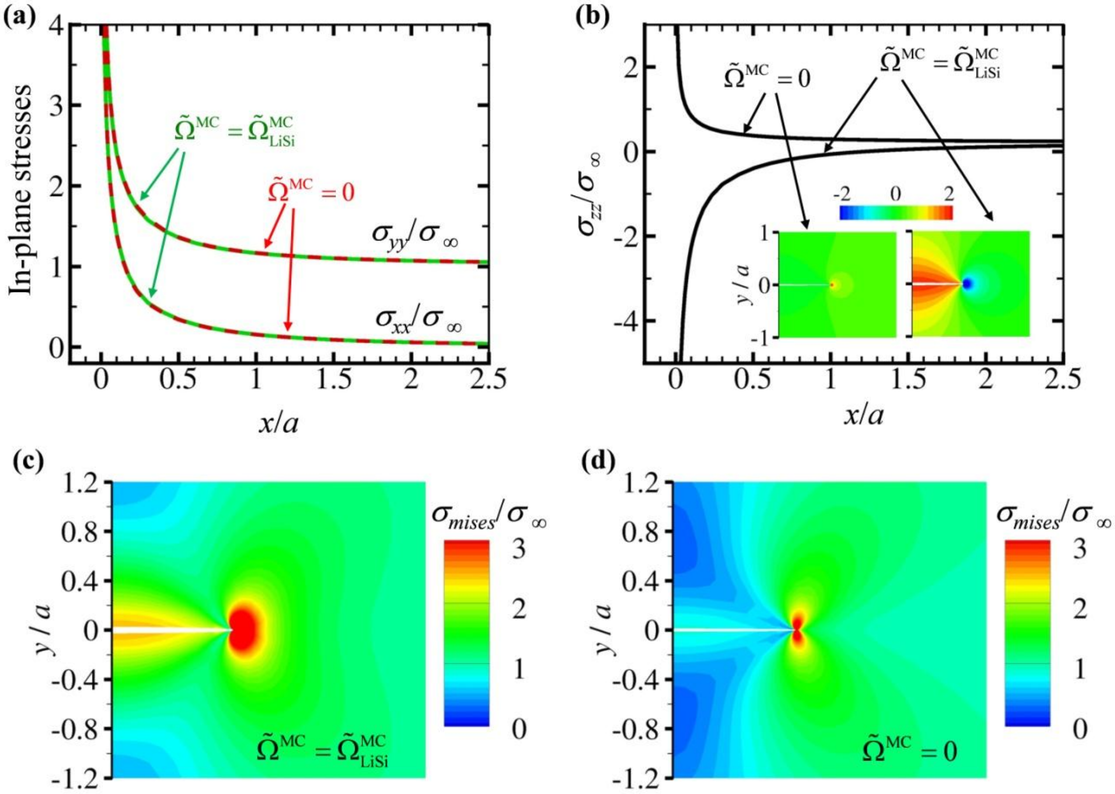

Fig. 5.4. Distributions of σ_{xx}, σ_{yy}, σ_{zz} *and the von Mises effective stress* σ_{mises} *normalized by the remote stress* $\sigma_{\infty} = 0.005E$ *. (a-b) Normalized in-plane stresses (a) and out-of-plane stress (b) along y=0. (c-d) Normalized von Mises stress for fully-coupled (c) and purely mechanical (d) cases. The length of the center-crack is 500 nm and the initial SOC is* $\Xi_0 = \bar{\Xi} = 0.4$*. All the spatial dimensions are normalized by the crack length a.*

In terms of stress intensity factor K_{I}, how does the coupled case here differ from the pure linear elastic case in without chemical transport of Li? This issue warrants a careful examination. If we follow the classic linear elastic fracture mechanics (LEFM) definition, the single parameter K_{I} that determines the in-plane stress fields near the crack tip is evaluated through

$$\lim_{r\to 0}\sigma_{ij} = \frac{K_I}{\sqrt{2\pi r}}\, f_{ij}(\theta), \quad (i, j = 1, 2), \tag{5-46}$$

where (r,θ) are the polar coordinates with origin at the crack tip. For both plane-strain and plane-stress conditions, Eq. (5-46) has the same form of $f_{ij}(\theta)$. Effect of out-of-plane constraint kicks in only through out-of-plane stress: for plane-strain, $\sigma_{zz} = \nu(\sigma_{xx} + \sigma_{yy})$; for plane-stress $\sigma_{zz} = 0$.

Although the stress states in Fig. 5.4 are computed under plane-strain conditions, the relationship of $\sigma_{zz} = \nu(\sigma_{xx} + \sigma_{yy})$ is no-longer valid. Instead, $\sigma_{zz} < 0$ for $\tilde{\Omega}^{\mathrm{MC}} = \tilde{\Omega}^{\mathrm{MC}}_{\mathrm{LiSi}}$, as seen in Fig. 5.4(b). Still, the results in Fig. 5.4(a) indicate that the in-plane stresses are independent of $\tilde{\Omega}^{\mathrm{MC}}$. In other words, as long as the material is elastic and sufficient time is given to allow diffusion to occur (i.e. $T_0 \gg \tau^{Li}$), the in-plane stresses can always be characterized by Eq. (5-46) even though stresses affect Li redistribution. The outcome is that K_I is independent of the accumulation of Li at the crack tip. Consequently, K_I is incapable of capturing the full effect of diffusion-deformation coupling on fracture.

5.4.2. Energy release rate

Similar findings on K_{I} have been made for hydrogen embrittlement of metals [53] and transformation toughening of ceramic materials [131], in the sense that the in-plane stresses are independent of dilatational eigen-strains near the stationary crack tip. This conclusion on in-plane stresses can also be proved analytically using the linear elastic compatibility conditions (which will not be elaborated here). However, previous studies have not clarified if the energy release rate, a more universal parameter for fracture analysis, changes as Li redistributes. We provide an analysis in this regard.

Fig. 5.5 (a) shows the calculated J values for the range of initial concentration of $0.2 < \Xi_0 < 0.999$. The circular symbols denote the non-coupled energy release rate $J^{\mathrm{NCP}} \equiv J\left(\tilde{\Omega}^{\mathrm{MC}} = 0\right)$ and the solid lines represent the fully-coupled values of $J^{\mathrm{CP}} \equiv J\left(\tilde{\Omega}^{\mathrm{MC}} = \tilde{\Omega}^{\mathrm{MC}}_{\mathrm{LiSi}}\right)$. For $\tilde{\Omega}^{\mathrm{MC}} = 0$, J^{NCP} coincides with the purely mechanical LEFM result of $J^{\mathrm{NCP}} / \left(aE\right) = \pi\left(1-\nu^2\right)\left(\sigma_\infty / E\right)^2$. For $\tilde{\Omega}^{\mathrm{MC}} = \tilde{\Omega}^{\mathrm{MC}}_{\mathrm{LiSi}}$, two observations can be made. First, J^{CP} depends on Ξ_0; second, $J^{CP} \geq J^{NCP}$. Specifically, for all initial concentrations J^{CP} is always higher than J^{NCP}, except for $\Xi_0 = 0.999$ when the two are essentially equal. This trend is more clearly seen in Fig. 5.5(b), which shows J^{CP}/ J^{NCP} as a function of Ξ_0 (crack length of 500 nm and remote load $\sigma_\infty = 0.005E$).

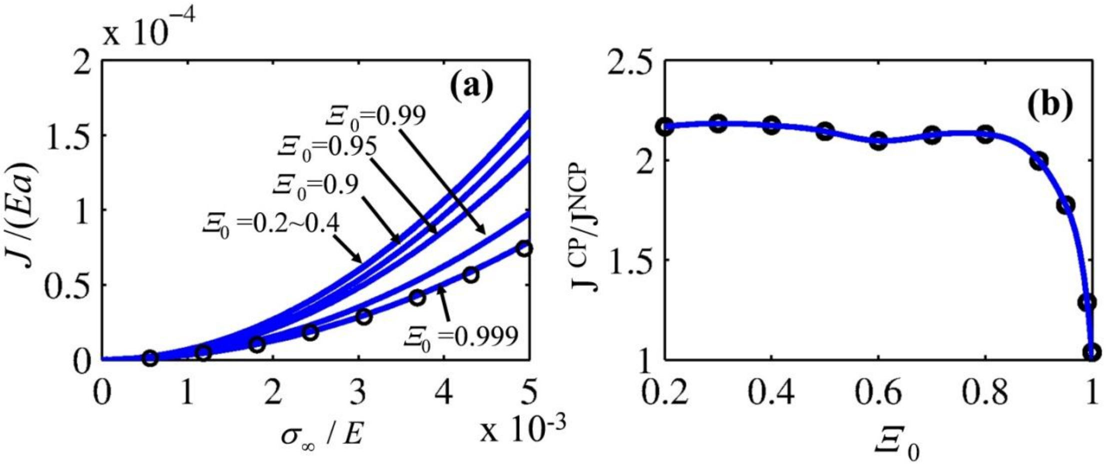

Fig. 5.5. Path-independent J integral for a stationary crack in Fig. 2a using Eq. (5-41). (a) Energy release rate for the fully-coupled case $J^{\mathrm{CP}} \equiv J\left(\tilde{\Omega}^{\mathrm{MC}} = \tilde{\Omega}^{\mathrm{MC}}_{\mathrm{LiSi}}\right)$ *as a function of remote stress for different levels of initial concentration* Ξ_0*, the circular symbols denote* $J^{\mathrm{NCP}} \equiv J\left(\tilde{\Omega}^{\mathrm{MC}} = 0\right)$ *as the baseline for comparison. (b) Dependence of* J^{CP} *on initial concentration when* K_I *(thus* J^{NCP}*) is fixed at a value that corresponds to a=500 nm and* $\sigma_\infty = 0.005E$.

The Ξ_0-dependence of J^{CP} is due to the fact that Li content Ξ cannot exceed 1, as embodied by the fact that $\mu^{Li}/k_B\theta \to \infty$ when $\Xi \to 1$ [cf. Eq. (5-45)]. If the initial content Ξ_0 is close to 1, redistribution of Li cannot happen and J^{CP} approaches J^{NCP}. The plateau for $\Xi_0 < 0.8$ [cf. Fig. 5.3(b)], on the other hand, is due to the fact that the relaxation of σ_m is nearly complete such that changes in Ξ_0 in the range of $0.2 < \Xi_0 < 0.8$ bear no significant influence on J^{CP}.

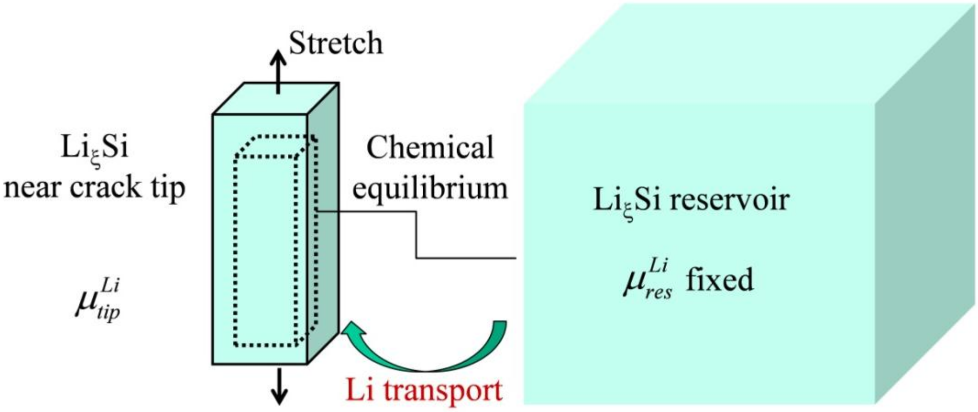

Fig. 5.6. Illustration of the negative effective Poisson's ratio effect. When material near the crack tip is subject to uniaxial tensile stresses, Li transported from a reservoir may overcome the elastic Poisson's effect and induce an overall expansion in the transverse directions. The cuboid with dotted boundary denotes the initial configuration of the isolated near-tip system before stretching, and the cuboid with solid boundary represent its stretched counterpart.

The finding that $J^{CP}/J^{NCP} \geq 1$ appears counterintuitive at the first glance: since Li redistribution is a stress relaxation mechanism, why would this redistribution cause the energy release rate to increase? It turns out that this anomaly can be associated with a negative effective

Poisson's ratio effect near the crack tip. If we conceptually isolate the Li$_\xi$Si material near the crack tip, the bulk of Li$_\xi$Si far from the crack can be regarded as a reservoir with fixed Li chemical potential μ_{res}^{Li} [Fig. 5.6]. Consider a uniaxial stretch applied to the near-tip material. During the stretch, μ_{tip}^{Li} decreases as the hydrostatic stress becomes tensile. The associated chemical potential difference $\mu_{tip}^{Li} - \mu_{res}^{Li} < 0$ drives Li from the reservoir into the crack tip. If the amount of Li so transported is large enough, the associated lithiation-induced volume change may overcome the elastic Poisson effect and lead to transverse expansion. The outcome is effectively a negative Poisson's ratio – tensile loading causes lateral dimensions to increase. This is exactly what happens here for Li$_\xi$Si.

To quantify this effect, we consider the limiting case with $D_0^{Li} = \infty$, $\tilde{\Omega}^{\mathrm{MC}} = \infty$ and $\xi_{\max} = \infty$. Under this condition, the chemical potential in the entire material is always in equilibrium and the mechanical contribution to diffusion [quantified by $\mu^{Li}/(k_B\theta)$] $-\tilde{\Omega}^{\mathrm{MC}}(\sigma_m/E)$ dominates the chemical contribution $\mu_*^{Li}/(k_B\theta) + \ln[\Xi/(1-\Xi)]$ [cf. Eq. (5-45)]. Consequently, σ_m in the near-tip region is pinned at the same level as that in the remote regions.

For $\tilde{\Omega}^{\mathrm{MC}} = 0$, the elastic response of the material is characterized by bulk modulus *K* and shear modulus *G*. For $\tilde{\Omega}^{\mathrm{MC}} = \infty$, on the other hand, the overall deformation is governed by effective moduli $G^{eff} = G, K^{eff} = 0$, and $\nu^{eff} = -1$, reflecting the fact that near-tip σ_m is pined at the remote level.

Now that K_I is independent of $\tilde{\Omega}^{\mathrm{MC}}$ [discussions in 5.4.1], the introduction of G^{eff} and K^{eff} allows $J\left(\tilde{\Omega}^{\mathrm{MC}}=\infty\right)$ to be calculated from K_I using the classic LEFM relation. Specifically,

$$J\left(\tilde{\Omega}^{\mathrm{MC}}=\infty\right)=\lim_{K^{eff}\to 0}\frac{1-\left(\nu^{eff}\right)^2}{E^{eff}}K_I^2=\frac{K_I^2}{G^{eff}}=\frac{K_I^2}{G}. \tag{5-47}$$

In contrast, the energy release rate for the purely mechanical case is

$$J^{NCP}=J\left(\tilde{\Omega}^{\mathrm{MC}}=0\right)=\frac{1-\nu^2}{E}K_I^2=\frac{1-\nu}{2G}K_I^2. \tag{5-48}$$

We therefore have shown that

$$\frac{J\left(\tilde{\Omega}^{\mathrm{MC}}=\infty\right)}{J\left(\tilde{\Omega}^{\mathrm{MC}}=0\right)}=\frac{2}{1-\nu}. \tag{5-49}$$

Indeed, for $\nu=0.22$ the ratio given by Eq. (5-49) is 2.56, which is fairly close to the plateau value (≈2.2) of J^{CP}/J^{NCP} in Fig. 5.5(b). The difference is due to the fact that the ideal case of $\tilde{\Omega}^{\mathrm{MC}}=\infty$ [Eq. (5-49)] overestimates the relaxation of σ_m compared with the realistic case of $\tilde{\Omega}^{\mathrm{MC}}=\tilde{\Omega}^{\mathrm{MC}}_{\mathrm{LiSi}}$ [Fig. 5.5(b)].

From an energetic point of view, $J^{CP}>J^{NCP}$ embodies the fact that the redistribution of Li provides another source of energy for the fracture driving force besides the mechanical fields. Two complementary processes make this additional source of energy available for fracture. The first is energy storage. For $\tilde{\Omega}^{\mathrm{MC}}\neq 0$, the external agency ($\sigma_\infty$ here) must provide extra work compared with the case with $\tilde{\Omega}^{\mathrm{MC}} = 0$ in order to induce the same remote fields. This extra work is stored as latent energy in the form of inhomogeneous Li concentration. The second mechanism is energy retrieval. Through the agency of composition-change-induced stresses, the latent energy is converted back into mechanical energy, thereby increasing the fracture driving force.

The storage process is controlled by $\tilde{\Omega}^{\mathrm{MC}}$ and the retrieval process is controlled by $\tilde{\Omega}^{\mathrm{CM}}$. If either $\tilde{\Omega}^{\mathrm{MC}}$ or $\tilde{\Omega}^{\mathrm{CM}}$ is zero, the coupling is severed and the energy release rate reduces to the purely mechanical level. On the other hand, the analysis in eqns. (5-47)-(5-49) provides an upper bound for the change of energy release rate due to this storage-retrieval mechanism. This limit is reached when the hydrostatic stress field is completely relaxed (to the remote level) so that full redistribution of Li has occurred. This upper bound is universal or the same for all cases regardless of material properties and loading, as long as the material response is elastic and the loading is slow.

It should be noted that the anti-shielding effect of *J* due to deformation-diffusion coupling (i.e., the fact that $J^{CP} > J^{NCP}$) in this study is evaluated for the steady-state of Li distribution such that $T_0 \gg \tau^{Li}$. Under this condition, stresses arise solely because of external constraint [Fig. 5.2(b)] or mechanical loading [Fig. 5.2(a)]. As pointed out earlier, in general stresses may also develop during charge/discharge due to concentration inhomogeneity when $\tau^{Li} \sim T_0$, as seen in free-standing amorphous LiSi particles or NWs [17, 32, 43, 45]. For such situations with transient effect, deformation-diffusion full coupling would manifest itself in two aspects. First, accumulation of Li near the crack tip, again, leads to an anti-shielding effect on *J* which increases the magnitude of the energy release rate. Second, remote concentrations and stresses far from the crack are governed by an effective diffusivity D_{eff} [22, 43]. This D_{eff} leads to a stress-enhanced-diffusion (SED) effect that lowers the remote stresses [43] and hence *J*. In other words, the first effect increases *J* while the second effect decreases *J*. The final outcome is the combined effect of the two. Depending on the ratio of *a*/*H*, the characteristic time scales for the two effects can be different. This transient situation of $\tau^{Li} \sim T_0$ is not the focus of this section. Instead, configurations shown in Fig. 5.2 with $T_0 \gg \tau^{Li}$ are considered in order to isolate the effect of Li accumulation near the crack tip (the first effect). The insight thus obtained can be easily combined with the effect of SED for far fields and thereby extended to situations with $\tau^{Li} \sim T_0$.

5.4.3. Remarks on K_{I}-based and *J*-based fracture approaches

We have shown earlier that K_{I} is independent of $\tilde{\Omega}^{\mathrm{MC}}$, i.e. K_{I} is unaffected by the deformation/diffusion coupling in the long-term limit (i.e. $T_0 \gg \tau^{Li}$). In contrast, Fig. 5.5 and Eqs. (5-47)-(5-49) show clearly that the coupled energy release rate does depend on $\tilde{\Omega}^{\mathrm{MC}}$. Even when the conditions of plane strain are maintained, the relationship between *J* and K_{I} is no longer unique, in the sense that the coupled energy release depends on $\tilde{\Omega}^{\mathrm{MC}}$, $\tilde{\Omega}^{\mathrm{CM}}$ and Ξ_0. Given this dichotomy, we ponder the question of which criterion, $K_{\mathrm{I}} = K_{Ic}$ or $J = J_{CR}$, is more appropriate.

To answer this question, we first note that a similar dichotomy exists in classic fracture mechanics in that the relationship between *J* and K_{I} is not always unique there either. Specifically, under the same in-plane loading, $J^{NCP} = \left(1-\nu^2\right) K_I^2 / E$ for plane-strain and $J^{NCP} = K_I^2 / E$ for plane-stress. This difference arises due to the difference in the out-of-plane constraint and, hence, crack tip stress triaxiality. Here, however, the situation is more complicated because the crack-tip stress triaxiality is not only determined by out-of-plane constraint but also by the redistribution of Li. Depending on the values of $\tilde{\Omega}^{\mathrm{MC}}$, $\tilde{\Omega}^{\mathrm{CM}}$ and Ξ_0, σ_{zz} may assume any value between $\nu\left(\sigma_{xx}+\sigma_{yy}\right)$ and $-\left(\sigma_{xx}+\sigma_{yy}\right)$, and J may be of any value between $\left(1-\nu^2\right)K_I^2/E$ [for $\tilde{\Omega}^{\mathrm{MC}}=0$] and $K_I^2/G=2\left(1+\nu\right)K_I^2/E$ [for $\tilde{\Omega}^{\mathrm{MC}}=\infty$], even under the same plane-strain conditions.

In the pure mechanical case, the fracture criterion can be stated as

$$\left.\begin{array}{l} K(d^{crack})=K_{critical}(d^{crack}),\text{ or} \\ J(d^{crack})=J_{CR}(d^{crack}). \end{array}\right\} \tag{5-50}$$

The effect of crack-tip load triaxiality can be lumped into the thickness-dependence of fracture toughness $K_{critical}(d^{crack})$ which is higher than the plane strain fracture toughness K_{Ic} and lower than the plane stress fracture toughness K_c such that $K_{Ic}\le K_{critical}(d^{crack})\le K_c$. This handling allows the stress intensity factor K_{I} calculated solely from in-plane stresses, which do not depend on out-of-plane constraints, to be compared with the thickness-dependent fracture toughness $K_{critical}(d^{crack})$ to determine the onset of fracture. As a conservative measure, the plane-strain fracture toughness K_{Ic} is most often used. A similar treatment is reflected in the *J*-integral based fracture criterion above in that both *J* and J_{CR} are thickness-dependent.

Similarly, it is also possible to state the fracture criterion for electrode materials which deforms only elastically and experience diffusion/deformation coupling as

$$\left.\begin{aligned} K(d^{crack}) &= K_{critical}(d^{crack}, \Xi_0), \text{ or} \\ J(d^{crack}, \Xi_0) &= J_{CR}(d^{crack}, \Xi_0), \end{aligned}\right\} \tag{5-51}$$

as long as both sides of these relations are specific to the same thickness *and*, in addition, the right hand sides are also specific to the initial state of charge Ξ_0. At this stage, it is unclear under what conditions the critical value functions $K_{critical}(d^{crack}, \Xi_0)$ and $J_{CR}(d^{crack}, \Xi_0)$ would assume their minima or most conservative values. These failure envelopes separating the safe and unsafe regions in the (d^{crack}, Ξ_0) space can only be determined by experiments.

As a concluding remark to this section, it should be noted the results in Fig. 5.3-Fig. 5.5 are based on the highly-idealized assumption that the material is linear elastic. Understandably, the behavior of real Li/Si, which is capable of deforming plastically, is different. The results in this section may be more applicable to cathode materials such as $LiFePO_4$ which is generally quite brittle. When significant (large-scale) plasticity is involved, the *K*-based criterion (the first of Eq. (5-51)) should not be used and the *J*-based criterion [the second of Eq. (5-51)] is the only sensible approach. Nevertheless, the analysis in this section yields insight into the behavior of alloy-based electrode materials. This discussion lays the foundation for further discussions accounting the effect of plasticity and lithiation-induced softening in the following sections.

5.5. Elasto-plastic case

We now turn our attention to the situation when the electrode material deforms plastically, especially when plastic deformation is large enough to render the LEFM approach using K invalid. To this end, we first consider a simplified case such that the yield stress σ_Y is assumed to be independent of Ξ_0 (section 5.5.1). For this purpose, we assume the same material properties and dimensionless parameters as listed in Table 1, with only one extra dimensionless number $\tilde{\sigma}_Y \equiv \sigma_Y / E \ll 1$ which quantifies concentration-independent yield stress σ_Y. The case with concentration-dependent σ_Y and elastic moduli will be considered in section 5.5.2.

When the material deforms plastically, the stress-controlled configuration [Fig. 5.2 (a)] used to facilitate comparison with pure mechanical LEFM solutions is no longer appropriate because any remote stress σ_∞ exceeding σ_Y would lead to large-scale plastic deformation. In this section, we therefore use the configuration shown in Fig. 5.2(b) which involves a thin-film electrode with initial thickness H and SOC Ξ_0 under galvanostatic discharging. Again, the pre-defect is a surface crack with length a and a small but finite crack-tip radius of $\rho \ll a$. The initial stress-free state (with SOC of Ξ_0) is taken to be the Lagrangian configuration in which the energy release rate is calculated via Eq. (5-41). A surface outflux of J_{surf} is specified to simulate galvanostatic discharging such that the average SOC $\bar{\Xi}$ in the film decreases with time t according to $\bar{\Xi}(t) = \Xi_0 - t / T_0$ for $t < \Xi_0 / T_0$, where $T_0 = (1\,\text{hour}) / (\text{C-rate})$ is the nominal discharge time. The nominal thickness H_0 is the thickness of the film in the fully discharged (i.e., $\Xi = 0$ throughout the electrode) state. It is related to the initial thickness H via $H \approx J^{SF}(\Xi_0) H_0$.

The approximation is associated with elastic strains and therefore is very reasonable. Unless indicated otherwise, H_0 is used because it is more convenient and almost exclusively used in the literature [37, 91, 132, 133].

For the calculation in this section, a typical film thickness of $H_0 = 200\,\text{nm}$ and nominal discharging time of T_0 =50 h are considered. These values are such that $T_0 \gg \tau^{Li}$ and are in the range of available experimental data. In addition, $a/H = a/\left[J^{SF}\left(\Xi_0\right)H_0\right] \le 1/4$, so that the film/substrate interface does not significantly affect crack-tip fields.

5.5.1. Effect of global yielding on energy release rate

For galvanostatic discharging, the dimensionless discharge level $\Delta\bar{\Xi} \equiv \Xi_0 - \bar{\Xi}(t) = t/T_0$ can be used to conveniently characterize the amount of Li extracted during the process. When $T_0 \gg \tau^{Li}$, all stresses are due to constraint at the film-substrate interface, and the bi-axial stress state far from the crack can be written as

$$\begin{cases} \sigma_{xx} = \sigma_{yy} = \dfrac{1}{3}\dfrac{E}{1-\nu}\dfrac{J^{SF}\left(\Delta\bar{\Xi}\right)}{J^{SF}\left(\Xi_0\right)}, & \text{for } \Delta\bar{\Xi} \le \Delta\bar{\Xi}_Y, \\ \sigma_{xx} = \sigma_{yy} = \sigma_Y, & \text{for } \Delta\bar{\Xi} > \Delta\bar{\Xi}_Y, \end{cases} \tag{5-52}$$

where $\Delta\bar{\Xi}_Y$ is the discharge level at which σ_{xx} and σ_{yy} reach σ_Y so that the film begins to yield globally. $\Delta\bar{\Xi}_Y$ is approximately independent of $\tilde{\Omega}^{\text{MC}}$ so long as $T_0 \gg \tau^{Li}$, because $\tilde{\Omega}^{\text{MC}}$ only affects the Li distribution near the crack and has no bearings on stresses far away from the crack $\left(y \gg H\right)$ where $\Xi = \Xi_0 - \Delta\bar{\Xi}_Y$ is homogeneous.

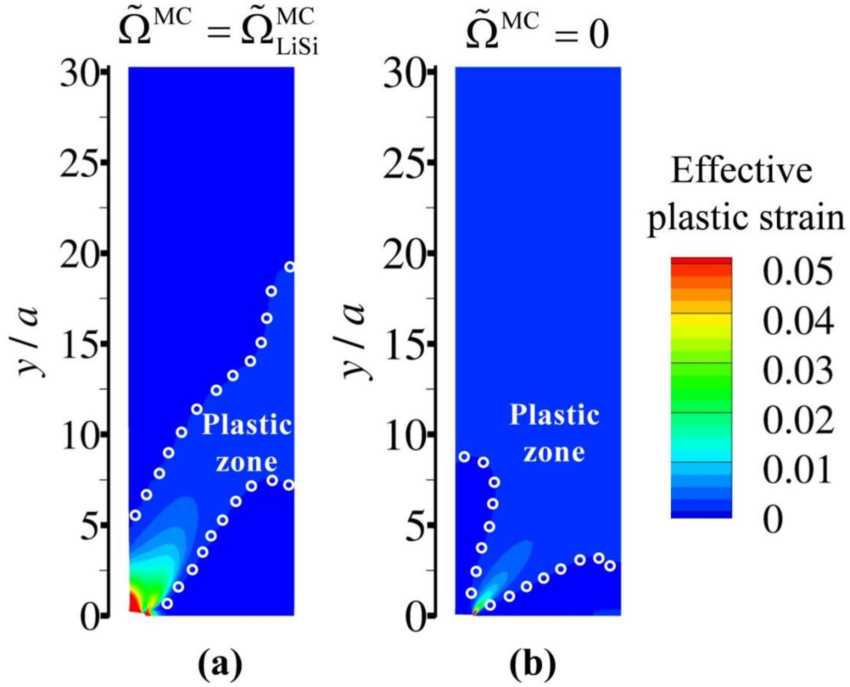

Fig. 5.7. Effective plastic strain ε^{p}_{eff} *for a stationary crack with a=50 nm in a film with nominal thickness* $H_0 = 200\,\mathrm{nm}$ *and initial concentration of* $\Xi_0 = 0.5$*, when the discharge reaches a level* $\Delta\bar{\Xi}_Y$ *such that the film begins to yield globally with* $\tilde{\sigma}_Y = 0.01$*. (a)* ε^{p}_{eff} *for fully-coupled case* $\tilde{\Omega}^{\mathrm{MC}} = \tilde{\Omega}^{\mathrm{MC}}_{\mathrm{LiSi}}$*; (b)* ε^{p}_{eff} *with* $\tilde{\Omega}^{\mathrm{MC}} = 0$*.*

Fig. 5.7 shows the distribution of effective plastic strain $\varepsilon^{p}_{eff} \equiv \int_0^t \sqrt{(2/3)\mathbf{D}^p : \mathbf{D}^p}\,dt$ for a film with $\tilde{\sigma}_Y = 0.01$, $H_0 = 200\,\mathrm{nm}$, *a*=50 nm and $\Xi_0 = 0.5$, at $\Delta\bar{\Xi} = \Delta\bar{\Xi}_Y$ as specified by Eq. (5-52). The plastic zone indeed extends through the thickness (horizontal) of the film for both $\tilde{\Omega}^{\mathrm{MC}} = \tilde{\Omega}^{\mathrm{MC}}_{\mathrm{LiSi}}$ and $\tilde{\Omega}^{\mathrm{MC}} = 0$, confirming the onset of full-scale yielding. The remote regions show slightly later yielding for $\tilde{\Omega}^{\mathrm{MC}} = \tilde{\Omega}^{\mathrm{MC}}_{\mathrm{LiSi}}$ than for $\tilde{\Omega}^{\mathrm{MC}} = 0$, mainly because of the finite dimension in the *y*-direction. This slight difference does not affect the main conclusions to be drawn. On the other hand, the plastic strain near the crack is higher for $\tilde{\Omega}^{\mathrm{MC}} = \tilde{\Omega}^{\mathrm{MC}}_{\mathrm{LiSi}}$ than for $\tilde{\Omega}^{\mathrm{MC}} = 0$, in consistency with the previous finding that Li redistribution increases the crack-tip von Mises stress [cf. Fig. 5.4 (c) and (d)]. This promotion of plastic deformation, together with the redistribution of Li, is also responsible for the observation that the crack opening is wider for $\tilde{\Omega}^{\mathrm{MC}} = \tilde{\Omega}^{\mathrm{MC}}_{\mathrm{LiSi}}$ than for $\tilde{\Omega}^{\mathrm{MC}} = 0$ [see Fig. 5.8 (a) and (b)].

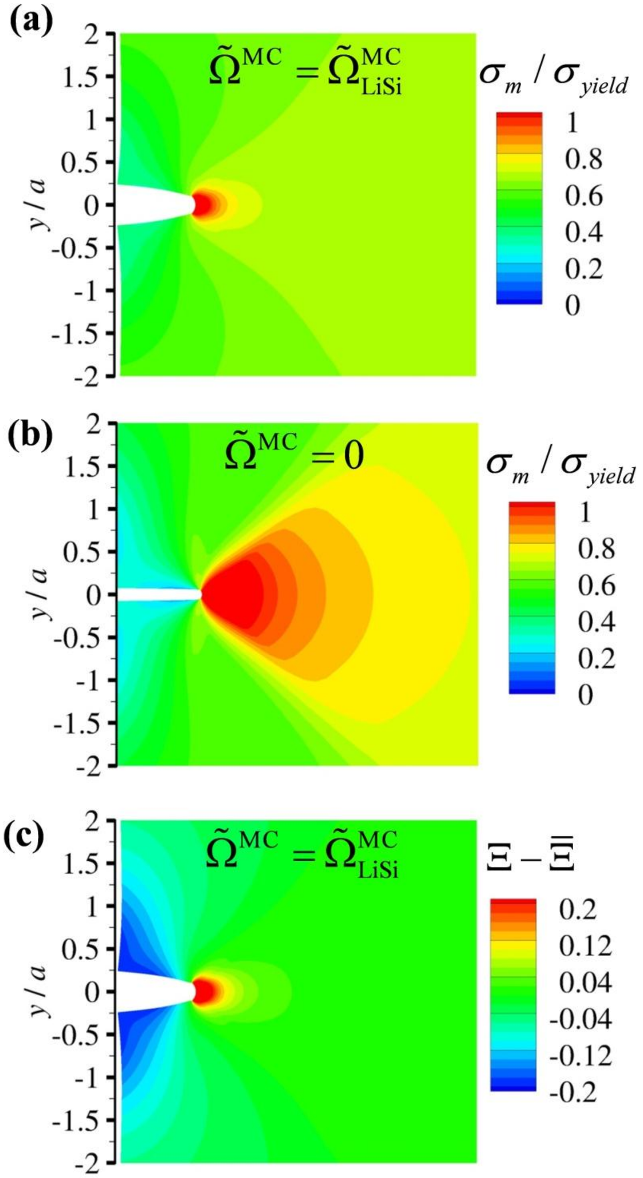

Fig. 5.8. Distributions of Li concentration and hydrostatic stress for a stationary crack with a=50 nm in a film with nominal thickness $H_0 = 200\ \mathrm{nm}$

and initial concentration $\Xi_0 = 0.5$. *The condition shown corresponds to onset of global yielding at* $\Delta\bar{\Xi} = \Delta\bar{\Xi}_Y$ *with* $\tilde{\sigma}_Y = 0.01$. *(a) hydrostatic stress normalized by yield stress for* $\tilde{\Omega}^{\mathrm{MC}} = \tilde{\Omega}^{\mathrm{MC}}_{\mathrm{LiSi}}$, *(b) hydrostatic stress normalized by yield stress for* $\tilde{\Omega}^{\mathrm{MC}} = 0$, *and (c) deviation of Li concentration from its average value* $\bar{\Xi} = \Xi_0 - \Delta\bar{\Xi}_Y$ *for* $\tilde{\Omega}^{\mathrm{MC}} = \tilde{\Omega}^{\mathrm{MC}}_{\mathrm{LiSi}}$.

The redistribution of Li and resultant relaxation of σ_m at $\Delta\bar{\Xi}_Y$ are shown in Fig. 8. Although significant plastic strains are involved, the redistribution of Li [Fig. 5.8 (c)] is rather similar to that in the fully elastic case [Fig. 5.3 (a)]. Again, this redistribution causes σ_m to relax [Fig. 8a and b]. In contrast to what is seen previously, the in-plane stresses are no longer independent of $\tilde{\Omega}^{\mathrm{MC}}$. This difference indicates that *J* is the only sensible parameter for characterizing the fracture behavior. It turns out that the path-independent form of *J* in Eq. (5-41) is highly robust numerically, with less than 0.5% difference between *J* calculated from difference contours even when $\Delta\bar{\Xi}$ reaches $\Delta\bar{\Xi}_Y$.

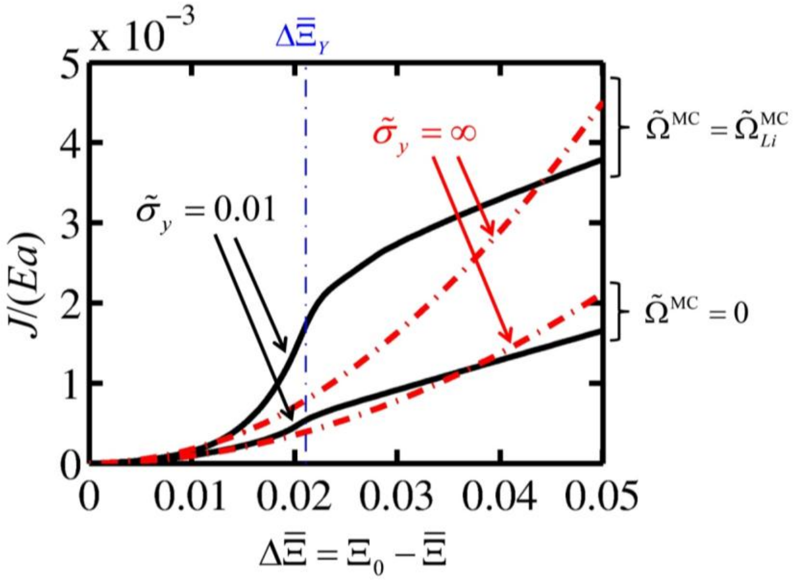

Fig. 5.9. Evolution of energy release rate J for a stationary surface crack with a=50 nm in a film with nominal thickness $H_0 = 200\,\mathrm{nm}$ *and initial*

concentration $\Xi_0 = 0.5$ *. Solid black lines indicate normalized values of* $J^{\mathrm{CP}} = J\left(\tilde{\Omega}^{\mathrm{MC}} = \tilde{\Omega}^{\mathrm{MC}}_{\mathrm{LiSi}}\right)$ *and* $J^{\mathrm{NCP}} = J\left(\tilde{\Omega}^{\mathrm{MC}} = 0\right)$ *for* $\tilde{\sigma}_Y = 0.01$ *. Dashed red lines show the corresponding* J^{CP} *and* J^{CP} *values for the corresponding elastic cases.*

Fig. 5.9 shows the evolution of *J* [normalized by (*Ea*)] for $\tilde{\sigma}_Y = 0.01$ (solid black lines). Both $J^{\mathrm{CP}} = J\left(\tilde{\Omega}^{\mathrm{MC}} = \tilde{\Omega}^{\mathrm{MC}}_{\mathrm{LiSi}}\right)$ and $J^{\mathrm{NCP}} = J\left(\tilde{\Omega}^{\mathrm{MC}} = 0\right)$ are plotted, with the corresponding curves for the purely elastic cases (red dashed lines) given for comparison. Clearly, plasticity significantly affects the energy release rate (both J^{CP} and J^{NCP}), except for the very initial stages of discharge ($\Delta\bar{\Xi} < 0.01$) when the plastic zone is small enough so that LEFM provides a good approximation.

As $\Delta\bar{\Xi}$ increases, both J^{CP} and J^{NCP} begin to deviate from their LEFM values. The most striking feature is the sudden slope changes in the $J - \Delta\bar{\Xi}$ curves (for both fully-coupled case of $\tilde{\Omega}^{\mathrm{MC}} = \tilde{\Omega}^{\mathrm{MC}}_{\mathrm{LiSi}}$ and purely mechanical case of $\tilde{\Omega}^{\mathrm{MC}} = 0$) when $\Delta\bar{\Xi}$ reaches the global yielding threshold $\Delta\bar{\Xi}_Y$ [cf. Fig. 5.7]. Before $\Delta\bar{\Xi}_Y$, plastic zone size r_y is small relative to the system dimension, and the effective K_I *and J* can be estimated using Irwin's effective crack length $a_{eff} = a + r_y$ [134]. Beyond $\Delta\bar{\Xi} = \Delta\bar{\Xi}_Y$, however, the film yields globally and Irwin's assumption no longer applies. Instead, plasticity in regions far away from the crack tip becomes important. This prevents the remote stresses from increasing further and leads to much flatter J^{CP} and J^{NCP} curves. Such global yielding is important because it significantly reduces the energy release rates, thereby lowering the fracture tendency.

The shapes of the J - $\Delta\bar{\Xi}$ curves in Fig. 5.9 are consistent with that was found by Aoki et al. [135] who calculated the energy release rate for a stationary crack in a thermally-loaded plate. What they studied corresponds to the special situation with $\tilde{\Omega}^{\mathrm{CM}} > 0$ and $\tilde{\Omega}^{\mathrm{MC}} = 0$. Our calculation confirms that the overall characteristics of the J - $\Delta\bar{\Xi}$ curve, especially the existence of inflection points, remain even for fully-coupled case with $\tilde{\Omega}^{\mathrm{MC}} \neq 0$. More importantly, Fig. 5.9 indicates that J^{CP}/ J^{NCP}>1 even when the combined effect of plasticity and diffusion/deformation coupling is considered, although the upper bound given by the linear elastic solution [Eqs. (5-47)-(5-49)] can no longer be used directly.

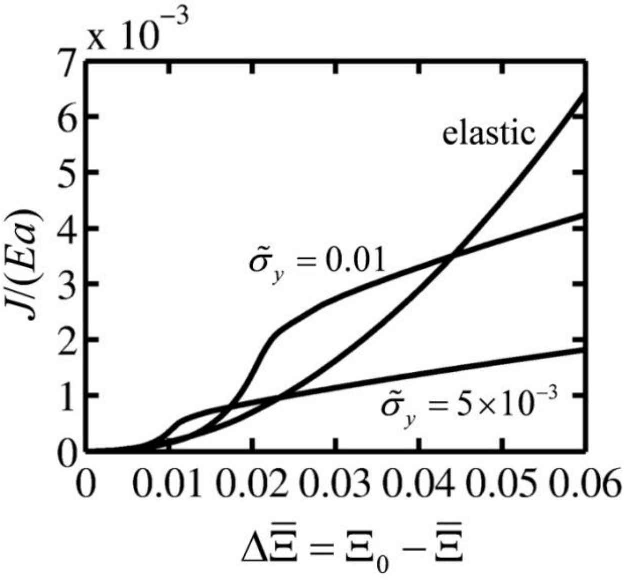

Fig. 5.10. Dependence of energy release on yield stress $\tilde{\sigma}_Y$. *The length of the surface crack is a=50 nm and the nominal film thickness is* $H_0 = 200\,\mathrm{nm}$. *The initial concentration is* $\Xi_0 = 0.5$. *Full deformation-diffusion coupling (*$\tilde{\Omega}^{\mathrm{MC}} = \tilde{\Omega}^{\mathrm{MC}}_{\mathrm{LiSi}}$ *) is considered.*

Fig. 5.10 shows the dependence of J on $\tilde{\sigma}_Y$ for the fully-coupled case of $\tilde{\Omega}^{\mathrm{MC}} = \tilde{\Omega}^{\mathrm{MC}}_{Li}$. For both $\tilde{\sigma}_Y = 0.005$ and $\tilde{\sigma}_Y = 0.01$, an inflection point is seen in the J-$\Delta\bar{\Xi}$ relation. The location of the inflection point for each case corresponds to its global-yielding threshold $\Delta\bar{\Xi}_Y$. Overall, the reduction in $\tilde{\sigma}_Y$ lowers the fracture tendency by lowering J [e.g. $J\left(\tilde{\sigma}_Y = 0.005\right) < J\left(\tilde{\sigma}_Y = 0.01\right) < J_{\text{elastic}}$ for $\Delta\bar{\Xi} > 0.05$], except for early stages before global yielding occurs so that the development of *J* is approximately governed by the effective crack length $a_{eff} \geq a$. In terms of elastic modulus, note that *J* is normalized by *Ea* so a reduction in *E* would also lead to a reduction in the fracture driving forces.

The discharge level $\Delta\bar{\Xi}_{CR}$ when critical condition $J = J_{CR}$ is reached determines the maximum extractable amount of Li without electrode failure. Designs and cycling regimens that maximize $\Delta\bar{\Xi}_{CR}$ would increase the utilizable capacity of the electrode without jeopardizing its cyclability. For the same J_{CR} and *a*, Fig. 5.10 shows that choosing materials with smaller E and $\tilde{\sigma}_Y$ (hence σ_Y) is an effective way to avoid fracture.

5.5.2. Effect of lithiation-induced softening

What we learned from Fig. 5.10 can be important for alloy-based electrode materials, because the elastic moduli and yield stress of such materials show significant dependence on Li concentration. If we manage to find a composition window $\bar{\Xi} \in \left(\Xi_0 - \Delta\bar{\Xi}_{CR}, \Xi_0\right)$ for which the combination of elastic modulus and yield stresses minimizes J, we can operate the battery in such a window to maximize the operational capacity $\Delta\bar{\Xi}_{CR}$.

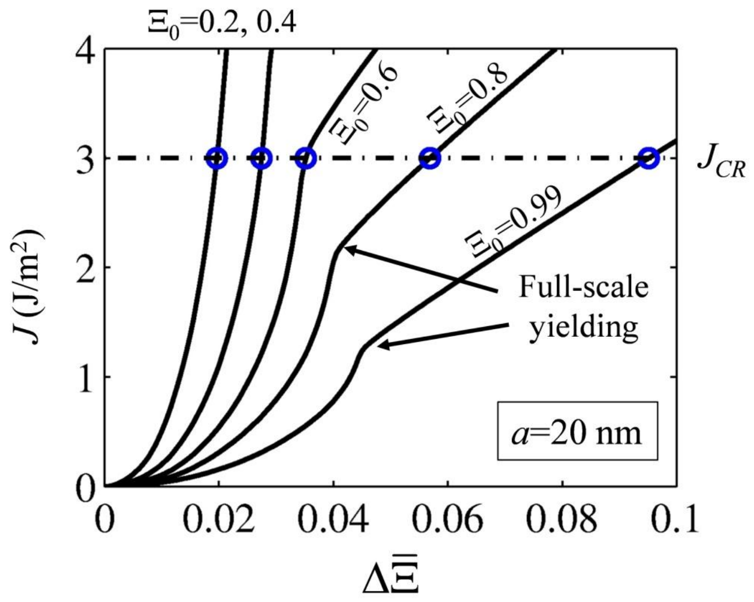

Fig. 5.11. Dependence of energy release rate on discharge level $\Delta\bar{\Xi}$ *and initial concentration* Ξ_0 *for a crack length of 20 nm. Full deformation-diffusion coupling is considered.*

To find such a window for Li/Si, we now put all the insights learned thus far together and assess the combined effect of diffusion/deformation coupling, inelasticity, and lithiation-induced softening on fracturing driving force. To this end, calculations involving composition-dependent bulk modulus $K = (12.46\xi + 65.44)/(1+\xi)$ GPa, shear modulus $G = (7.63\xi + 35.51)/(1+\xi)$ GPa [77], and yield stress $\sigma_Y = \left(1.75 + 0.167\xi\right)/\left(1+\xi\right)$ GPa, are conducted. The variation of yield stress with concentration represents a simple interpolation between $\sigma_Y = 1.75$ GPa at $\xi = 0$ and $\sigma_Y = 0.5$ GPa at $\xi = \xi_{\max}$ [15, 56] using the rule of mixture. Although it is likely that J_{CR} for Li/Si is composition-dependent, we adopt a constant value of $J_{CR} = 3\,\mathrm{J/m^2}$ due to lack of experimental data. This critical value is estimated using the toughness for pure silicon which is typically between 2.5~4.3 J/m^2 [38].

Since the mechanical properties here are concentration-dependent, dimensionless parameters $\tilde{\Omega}^{\mathrm{MC}}$ and $\tilde{\sigma}_Y$ are no-longer convenient, and all quantities will be stated in their respective physical units. The system configuration and discharge rate are the same as those in section 5.5.1 [Fig. 5.2 (b)], which is relevant for thin-film electrodes under galvanostatic discharge.

Fig. 5.11 shows the dependence of J development on initial concentration Ξ_0, for a film with nominal thickness of $H_0 = 200\,\mathrm{nm}$ and pre-crack length of a=20 nm. For each $J - \Delta\bar{\Xi}$ curve, the critical discharge level $\Delta\bar{\Xi}_{CR}$ at which $J = J_{CR}$ is marked. Two scenarios can be identified. For lower Ξ_0 [e.g., $\Xi_0 < 0.6$] the energy release rate reaches its critical value before the onset of full-scale yielding. For higher Ξ_0[e.g., $\Xi_0 \geq 0.8$], on the other hand, the material is softer and the inflection point $\Delta\bar{\Xi}_Y$ is reached before fracture.

In the first scenario, fracture is essentially governed by Irwin's effective crack length. Under this condition, the $\Delta\bar{\Xi}_{CR} - \Xi_0$ dependency is mainly due to lithiation-induced elastic softening (i.e. reduction of elastic moduli as Li concentration increases). Specifically, since J is approximately proportional to the Young's modulus [note that J is normalized by (Ea) in Fig. 5.10], the fracture driving force is lower when the operation window is chosen at higher concentrations. In the second scenario, relaxation due to global yielding comes into play, leading to much wider windows of $\bar{\Xi} \in \left(\Xi_0 - \Delta\bar{\Xi}_{CR}, \Xi_0\right)$ than that in the first scenario. The increase in $\Delta\bar{\Xi}_{CR}$ due to global yielding is much more significant compared with that due to elastic softening. For all cases, the maximum allowed operational capacity $\Delta\bar{\Xi}_{CR}$ is always higher when Ξ_0 is higher, as a combined consequence of the lithiation-induced softening of E and σ_Y.

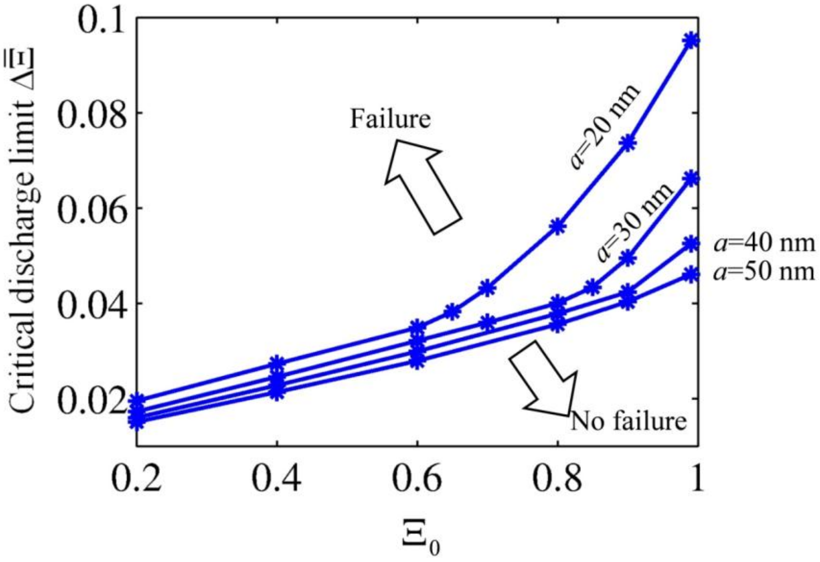

Fig. 5.12 Design map showing the maximum extractable amount of lithium $\Delta\bar{\Xi}$ *without crack growth as a function of initial SOC* Ξ_0 *for different pre-crack sizes. Full deformation-diffusion coupling is considered.*

We conclude our discussion with a design map [Fig. 5.12] which shows the maximum utilizable amount of Li (as measured by $\Delta\bar{\Xi}$) as a function of Ξ_0 when pre-cracks with different sizes are present. Again, $\bar{\Xi} \in \left(\Xi_0 - \Delta\bar{\Xi}_{CR}, \Xi_0\right)$ is the safe window in which the electrode can be operated without fracture. For each pre-crack length *a*, the corresponding $\Delta\bar{\Xi}_{CR} - \Xi_0$ curve delineates the boundary between the unsafe region (upper left) and the safe region (bottom right). In real thin-film electrodes, the smoothness of electrode surfaces is always limited by the manufacturing and operating conditions, and the existence of surface defects is inevitable. Fig. 5.12 indicates that for the same operational capacity ($\Delta\bar{\Xi}$), a thin-film electrode is always more defect-tolerant when the changing/discharging regimen is designed such that the battery operates at higher concentration windows of $\bar{\Xi} \in \left(\Xi_0 - \Delta\bar{\Xi}_{CR}, \Xi_0\right)$.

As a final remark, it should be noted that $\Delta\Xi_{CR}$ in Fig. 5.11 and Fig. 5.12 is calculated based on the assumption of a constant J_{CR}. For real alloy-based electrode materials, it is very likely that J_{CR} is concentration-dependent. Taking conventional engineering material as reference, the general trend for fracture toughness is that K_{IC} is higher for materials with lower σ_Y. If this trend is also true for Li/Si, J_{CR} would be higher at higher Li concentrations, a condition that would further reinforce the conclusion that operation at higher concentration is an effective means to mitigate failure of thin-film Li/Si electrodes. Such an analysis with composition-dependent J_{CR}, however, requires detailed experimental measurements and is not attempted in this study.

It should also be noted that the analysis here is based on a stress-free initial condition which does not consider residue stresses from prior lithiation processes. Such a simplification, however, does not affect the primary conclusions, especially the conclusion that operation windows at higher concentrations enhance battery cyclability.

5.6. Conclusions

In this final chapter, a fully-coupled finite deformation theory for analyzing the coupled mechano-diffusional driving forces for fracture in electrode materials is developed. The formulation of *J*-integral treats the crack tip as a separate thermodynamic system and entails detailed account of balances of mass and energy and evolution of entropy. It is found that the standard form of *J*-integral for energy release rate is no longer path-independent when coupled mechano-diffusion driving forces are present. Instead, an area integral must be included to maintain path-independency.

A numerical scheme for implementing this path-independent formulation through mixed finite element simulations is given. This numerical scheme is found to be highly robust, even under conditions of global yielding.

Under loading, lithium accumulates at tips, leading to relaxation of hydrostatic stress. This process does not affect in-plane stress fields or the tress intensity factor as along as the material is linear elastic and sufficient time is given for diffusion to occur (i.e. $T_0 \gg \tau^{Li}$). In contrast, the deformation-diffusion coupling increases the energy release rate (driving force for fracture). This anti-shielding effect on J can be understood through a negative effective Poisson's ratio effect. Specifically, the anti-shielding effect embodies the fact that the redistribution of Li provides another source of energy for the fracture besides the mechanical fields. Two complementary mechanisms make this additional source of energy available. These two mechanisms are controlled by two partial atomic volumes. The first is the chemical-to-mechanical $\tilde{\Omega}^{\mathrm{CM}}$, which controls storage. The second is the mechanical-to-chemical $\tilde{\Omega}^{\mathrm{MC}}$, which controls retrieval.

For electrode materials, energy release rate J and stress intensity factor K are not uniquely related. Under conditions of significant plasticity, K cannot be used and J is the only sensible choice for characterizing fracture. Before global yielding, fracture is governed by Iwrin's effective crack length; after global yielding, plastic deformation in regions far from the crack significantly reduces J and, hence, the likelihood of fracture. Global yielding marks an inflection point in the energy release rate-discharge level curve. In general, the driving force for fracture in thin-film electrodes can be lowered by operating at higher Li concentrations. A design map is developed to quantify this effect, accounting for lithiation-induced material softening, full diffusional-mechanical coupling and plasticity. This map can be used to guide the design of electrodes to improve cyclability and maximize utilizable operational capacity.

6. Concluding remarks

6.1. Significance of contribution

Electrode degradation due to internal stress build-up during cycling has been one of the key challenges for secondary battery designers. When guest atoms are inserted or extracted from the host in an electrode, the material in the electrode expands or contracts, inducing stresses that may cause material cracking. This issue is especially important in alloy-based electrode materials, which are attractive because their capacities are much higher than that of graphite, but at the same time experience much higher volume expansions. Previous studies indicate that miniaturization can be an effective means to develop electrodes for the next generation high-capacity and high-performance rechargeable batteries.

The improvement of nano-sized Li-alloy electrode materials requires a fundamental understanding of the chemo-mechanical characteristics of the coupled chemical-mechanical processes associated with the operation of batteries. While stress buildup associated with lithiation and delithiation bears certain resemblance to the development of thermo-stresses, a phenomenon better studied and relatively well-understood, the multiphysics processes in alloy-based electrodes are much more complex, challenging and intriguing. The reasons are not only because much larger deformations are involved, but also because the processes entail two-way coupling between diffusion and deformation, nonlinearity and chemical reaction. This richness of physics presents opportunities for interdisciplinary research to the solid mechanics, physics, chemistry, and materials communities. While the issues are challenging, the new phenomena are both theoretically interesting and practically important.

We have shown that the coupling between diffusion and stress is two-way and the strength of the mechanical-to-chemical coupling in Li/Si is much stronger that what has been known in other electrode materials such as intercalation cathode materials (e.g., $LiFePO_4$) and carbonaceous anode materials (e.g., LiC_6). Theoretical analyses of this coupling necessitate realistic models that account for the relevant physics and special techniques. Specifically, one of the major numerical challenges here is associated with the gradient of hydrostatic stress that appears in the governing equation for diffusion fluxes when a finite element (FE) method is used. We have proposed a method to leverage the concept of mixed finite elements to simulate the diffusion/deformation two–way coupling. Instead of using only the deformation and concentration of the diffusion species as nodal variables, the hydrostatic stress σ_m is treated as a redundant degree of freedom, thereby automatically resolve the relevant gradient needed by Fick's law.

Calculations based on the mixed finite element method indicate that lithium diffusion is very sensitive to external constraint. The design of battery electrodes involves tradeoffs among capacity, cyclability and operational charging rate. The main advantage of alloy-based electrodes, especially Li/Si, is their much higher capacity compared with carbon-based electrodes. In terms of cyclability, it has been suggested that plastic flow can be beneficial for Li/Si electrodes because it relaxes stresses and thus reduces the chance of electrode failure. Our results indicate that there is another mechanism at work. On one hand, plasticity may help avoid electrode fracture – a mechanism that can be utilized by adopting measures that promote inelastic flow through the tailoring of material properties and changing charging regimen. On the other hand, plasticity may inhibit Li transport, especially under tight mechanical constraint. Under any scenario, designs with less mechanical constraint on the electrodes are desirable because mechanical constraints diminishes stress-enhanced diffusion and magnifies the deleterious effect of plasticity and concentration-induced softening on Li transport. Because of these reasons, even in terms of operational charging rate alone, Li/Si nano-particles (e.g. nanospheres, nanoflakes, nanowires and nanotubes) are superior to Li/Si thin films or bulk materials. Our results in this regard provide further support for nano-particles as building blocks for next-generation alloy-based electrodes.

At high lithium concentrations, the diffusive migration of silicon may become non-negligible. It is found that diffusion of the host atoms can have a significant impact on stress, primarily because of the chemical interactions between the species and the effect of stress gradient on interdiffusion. In particular, under conditions of pure elastic deformation the diffusion of Si atoms can cause stress reductions up to ~20% with the modest diffusivity ratio of $D^{Si}/D^{Li}=1/50$. For amorphous Li/Si alloys, the mechanical driving force dominates the chemical driving force, resulting in the migration of Si in the direction of the gradient of the hydrostatic stress $\nabla\sigma_m$ or from the surface to the center of cylindrical electrodes. The analysis has also shown what the behavior would be for alloys with (perhaps unrealistically) high thermodynamic factors. Our results indicate that the effect of interdiffusion on stress relaxation can be important even when the stress levels are below the yield threshold of the material.

A theory of coupled chemo-mechanical fracture driving forces is formulated in order to capture the effect of deformation-diffusion coupling and lithiation-induced softening on fracture.

This measure is used to analyze the fracture tendency in Li/Si electrodes through simulations by using the mixed finite element framework. Calculations show that under tensile loading, Li accumulates in front of crack tips, leading to an anti-shielding effect on the energy release rate. For a pre-cracked Li/Si thin-film electrode, it is found that the driving force for fracture is significantly lower when the electrode is operated at higher Li concentrations -- a result of more effective stress relaxation via global yielding. The results indicate that operation at higher concentrations is an effective means to minimize failure of thin-film Li/Si alloy electrodes. A design map for avoiding failure is thereby developed.

6.2. Future directions

All models and analyses for alloy-based electrode materials ultimately have a common goal: to improve the performance of batteries in terms of capacity, cyclability, and power density. The mitigation of lithiation-induced mechanical fracture and property degradation is generally regarded the foremost issue. On the other hand, experiments also show that besides fracture, alloy-based electrodes may also fail due to the formation and coalescence of internal voids [5]. Such failure by voiding, although potentially important, has been given much less attention than the failure by brittle or ductile fracture. Future research in this regard is considered highly relevant and important by the author.

On the other hand, most research on the mechanical issues of battery electrodes have focused on the stresses and fracture in the electrode material itself. Relatively less research has been carried out to consider the effects of the solid-electrolyte interphase (SEI), a layer that forms on the surface of electrodes [136]. This is partly due to a lack of experimental data on the mechanical properties of SEI. Nevertheless, studies by Wu et al. [3] indicate that the interaction between the SEI and the electrode material may significantly affect battery cyclability. Understanding of the implications of SEI on the stresses and failure tendency is probably the most important missing link between the current mechanical models and a more comprehensive understanding of the interplays among different factors in battery operation.

Finally, it is important to point out that ultimately the design of battery electrodes must reach the macroscopic size scale. As such, it is recognized that the microstructures of electrodes consist of not only the active particles or films, but also a binder and pores. There is no doubt that the complexity of models increases significantly when one goes from isolated particles to microstructures. Almost inevitably, simplifying assumptions and approximations are needed. The porous electrode theory [137, 138] is one of the earliest successful theories to reduce the complex microstructures of battery electrodes into a more tractable 1-D homogenized picture. Christensen [139] proposed a pseudo-2D model which is essentially a multi-scale model that links the global solution of porous electrode theory to the microscopic response of an individual particle. Bottom-up models that directly simulate the coupling between electrochemistry and mechanical deformation at the microscopic level have also been developed [50, 117, 140, 141]. Despite these progresses, the chemo-mechanical properties and behaviors of electrode microstructures are much less investigated than those of stand-alone electrode particles, and the microstructure design which accounts for the essential multiphysics processes and the hierarchical nature of the materials is yet another area with significant research needs.

References

1 Larcher, D., Beattie, S., Morcrette, M., Edstroem, K., Jumas, J.C., and Tarascon, J.M.: 'Recent findings and prospects in the field of pure metals as negative electrodes for Li-ion batteries', J Mater Chem, 2007, 17, (36), pp. 3759-3772

2 Wu, H., Zheng, G., Liu, N., Carney, T.J., Yang, Y., and Cui, Y.: 'Engineering empty space between Si nanoparticles for lithium-ion battery anodes', Nano Lett, 2012, 12, (2), pp. 904-909

3 Wu, H., Chan, G., Choi, J.W., Ryu, I., Yao, Y., McDowell, M.T., Lee, S.W., Jackson, A., Yang, Y., Hu, L.B., and Cui, Y.: 'Stable cycling of double-walled silicon nanotube battery anodes through solid-electrolyte interphase control', Nature Nanotechnology, 2012, 7, (5), pp. 309-314

4 Yao, Y., McDowell, M.T., Ryu, I., Wu, H., Liu, N., Hu, L., Nix, W.D., and Cui, Y.: 'Interconnected silicon hollow nanospheres for lithium-ion battery anodes with long cycle life', Nano Lett, 2011, 11, (7), pp. 2949-2954

5 Hu, L.B., Wu, H., Gao, Y.F., Cao, A.Y., Li, H.B., McDough, J., Xie, X., Zhou, M., and Cui, Y.: 'Silicon-Carbon Nanotube Coaxial Sponge as Li-Ion Anodes with High Areal Capacity', Adv Energy Mater, 2011, 1, (4), pp. 523-527

6 Evanoff, K., Benson, J., Schauer, M., Kovalenko, I., Lashmore, D., Ready, W.J., and Yushin, G.: 'Ultra Strong Silicon-Coated Carbon Nanotube Nonwoven Fabric as a Multifunctional Lithium-Ion Battery Anode', Acs Nano, 2012, 6, (11), pp. 9837-9845

7 Chan, C.K., Peng, H., Liu, G., McIlwrath, K., Zhang, X.F., Huggins, R.A., and Cui, Y.: 'High-performance lithium battery anodes using silicon nanowires', Nat Nanotechnol, 2008, 3, (1), pp. 31-35

8 Cui, L.F., Ruffo, R., Chan, C.K., Peng, H., and Cui, Y.: 'Crystalline-amorphous core-shell silicon nanowires for high capacity and high current battery electrodes', Nano Lett, 2009, 9, (1), pp. 491-495

9 Song, T., Xia, J., Lee, J.H., Lee, D.H., Kwon, M.S., Choi, J.M., Wu, J., Doo, S.K., Chang, H., Park, W.I., Zang, D.S., Kim, H., Huang, Y., Hwang, K.C., Rogers, J.A., and Paik, U.: 'Arrays of sealed silicon nanotubes as anodes for lithium ion batteries', Nano Lett, 2010, 10, (5), pp. 1710-1716

10 Magasinski, A., Dixon, P., Hertzberg, B., Kvit, A., Ayala, J., and Yushin, G.: 'High-performance lithium-ion anodes using a hierarchical bottom-up approach', Nat Mater, 2010, 9, (4), pp. 353-358

11 Kovalenko, I., Zdyrko, B., Magasinski, A., Hertzberg, B., Milicev, Z., Burtovyy, R., Luzinov, I., and Yushin, G.: ‘A Major Constituent of Brown Algae for Use in High-Capacity Li-Ion Batteries’, Science, 2011, 333, (6052), pp. 75-79

12 Beaulieu, L.Y., Hatchard, T.D., Bonakdarpour, A., Fleischauer, M.D., and Dahn, J.R.: ‘Reaction of Li with alloy thin films studied by in situ AFM’, J Electrochem Soc, 2003, 150, (11), pp. A1457-A1464

13 Beaulieu, L.Y., Eberman, K.W., Turner, R.L., Krause, L.J., and Dahn, J.R.: ‘Colossal reversible volume changes in lithium alloys’, Electrochem. Solid State Lett., 2001, 4, (9), pp. A137-A140

14 Choi, J.W., McDonough, J., Jeong, S., Yoo, J.S., Chan, C.K., and Cui, Y.: ‘Stepwise Nanopore Evolution in One-Dimensional Nanostructures’, Nano Lett., 2010, 10, (4), pp. 1409-1413

15 Sethuraman, V.A., Chon, M.J., Shimshak, M., Srinivasan, V., and Guduru, P.R.: ‘In situ measurements of stress evolution in silicon thin films during electrochemical lithiation and delithiation’, Journal of Power Sources, 2010, 195, (15), pp. 5062-5066

16 Bower, A.F., Guduru, P.R., and Sethuraman, V.A.: ‘A finite strain model of stress, diffusion, plastic flow, and electrochemical reactions in a lithium-ion half-cell’, Journal of the Mechanics and Physics of Solids, 2011, 59, (4), pp. 804-828

17 Zhao, K.J., Pharr, M., Vlassak, J.J., and Suo, Z.G.: ‘Fracture of electrodes in lithium-ion batteries caused by fast charging’, J Appl Phys, 2010, 108, (7), pp. 073517

18 Gao, Y.F., Cho, M., and Zhou, M.: ‘Stress relaxation through interdiffusion in amorphous lithium alloy electrodes’, Journal of the Mechanics and Physics of Solids, 2013, 61, pp. 579-596

19 Haftbaradaran, H., Gao, H.J., and Curtin, W.A.: ‘A surface locking instability for atomic intercalation into a solid electrode’, Appl Phys Lett, 2010, 96, (9), pp. 091909

20 Cheng, Y.T., and Verbrugge, M.W.: ‘The influence of surface mechanics on diffusion induced stresses within spherical nanoparticles’, J Appl Phys, 2008, 104, (8), pp. 083521

21 Anand, L.: ‘A Cahn-Hilliard-type theory for species diffusion coupled with large elastic-plastic deformations’, Journal of the Mechanics and Physics of Solids, 2012, 60, (12), pp. 1983-2002

22 Ryu, I., Choi, J.W., Cui, Y., and Nix, W.D.: ‘Size-dependent fracture of Si nanowire battery anodes’, Journal of the Mechanics and Physics of Solids, 2011, 59, (9), pp. 1717-1730

23 Whittingham, M.S.: ‘Electrical Energy-Storage and Intercalation Chemistry’, Science, 1976, 192, (4244), pp. 1126-1127

24 Qi, Y., Guo, H.B., Hector, L.G., and Timmons, A.: ‘Threefold Increase in the Young's Modulus of Graphite Negative Electrode during Lithium Intercalation’, J Electrochem Soc, 2010, 157, (5), pp. A558-A566

25 Laforge, B., Levan-Jodin, L., Salot, R., and Billard, A.: ‘Study of germanium as electrode in thin-film battery’, J Electrochem Soc, 2008, 155, (2), pp. A181-A188

26 Winter, M., and Besenhard, J.O.: ‘Electrochemical lithiation of tin and tin-based intermetallics and composites’, Electrochim Acta, 1999, 45, (1-2), pp. 31-50

27 Li, J.C., Dozier, A.K., Li, Y.C., Yang, F.Q., and Cheng, Y.T.: ‘Crack Pattern Formation in Thin Film Lithium-Ion Battery Electrodes’, J Electrochem Soc, 2011, 158, (6), pp. A689-A694

28 Christensen, J., and Newman, J.: ‘A mathematical model of stress generation and fracture in lithium manganese oxide’, J Electrochem Soc, 2006, 153, (6), pp. A1019-A1030

29 Cheng, Y.T., and Verbrugge, M.W.: ‘Evolution of stress within a spherical insertion electrode particle under potentiostatic and galvanostatic operation’, J Power Sources, 2009, 190, (2), pp. 453-460

30 Cheng, Y.T., and Verbrugge, M.W.: ‘Application of Hasselman's Crack Propagation Model to Insertion Electrodes’, Electrochem. Solid State Lett., 2010, 13, (9), pp. A128-A131

31 Deshpande, R., Cheng, Y.T., and Verbrugge, M.W.: ‘Modeling diffusion-induced stress in nanowire electrode structures’, J Power Sources, 2010, 195, (15), pp. 5081-5088

32 Cheng, Y.T., and Verbrugge, M.W.: ‘Diffusion-Induced Stress, Interfacial Charge Transfer, and Criteria for Avoiding Crack Initiation of Electrode Particles’, J Electrochem Soc, 2010, 157, (4), pp. A508-A516

33 Zhao, K.J., Pharr, M., Vlassak, J.J., and Suo, Z.G.: ‘Inelastic hosts as electrodes for high-capacity lithium-ion batteries’, J Appl Phys, 2011, 109, (1), pp. 016110

34 Beaulieu, L.Y., Beattie, S.D., Hatchard, T.D., and Dahn, J.R.: ‘The electrochemical reaction of lithium with tin studied by in situ AFM’, J Electrochem Soc, 2003, 150, (4), pp. A419-A424

35 Xiao, X., Liu, P., Verbrugge, M.W., Haftbaradaran, H., and Gao, H.: ‘Improved cycling stability of silicon thin film electrodes through patterning for high energy density lithium batteries’, J Power Sources, 2011, 196, (3), pp. 1409-1416

36 Leung, K., and Neda, Z.: ‘Pattern formation and selection in quasistatic fracture’, Phys Rev Lett, 2000, 85, (3), pp. 662-665

37 Haftbaradaran, H., Xiao, X.C., Verbrugge, M.W., and Gao, H.J.: ‘Method to deduce the critical size for interfacial delamination of patterned electrode structures and application to lithiation of thin-film silicon islands’, J Power Sources, 2012, 206, pp. 357-366

38 Cook, R.F.: ‘Strength and sharp contact fracture of silicon’, J Mater Sci, 2006, 41, (3), pp. 841-872

39 Gao, Y.F., and Zhou, M.: ‘Coupled mechano-diffusional driving forces for fracture in electrode materials’, J Power Sources, 2013, 230, pp. 176-193

40 Cui, Z.W., Gao, F., and Qu, J.M.: ‘A finite deformation stress-dependent chemical potential and its applications to lithium ion batteries’, Journal of the Mechanics and Physics of Solids, 2012, 60, (7), pp. 1280-1295

41 Brassart, L., and Suo, Z.G.: ‘Reactive flow in solids’, Journal of the Mechanics and Physics of Solids, 2013, 61, (1), pp. 61-77

42 Brassart, L., and Suo, Z.G.: ‘Reactive Flow in Large-Deformation Electrodes of Lithium-Ion Batteries’, Int J Appl Mech, 2012, 4, (3)

43 Gao, Y.F., and Zhou, M.: ‘Strong stress-enhanced diffusion in amorphous lithium alloy nanowire electrodes’, J Appl Phys, 2011, 109, (1), pp. 014310

44 Gao, Y.F., and Zhou, M.: ‘Strong dependency of lithium diffusion on mechanical constraints in high-capacity Li-ion battery electrodes’, Acta Mech Sinica, 2012, 28, (4), pp. 1068-1077

45 Zhao, K.J., Pharr, M., Cai, S.Q., Vlassak, J.J., and Suo, Z.G.: ‘Large Plastic Deformation in High-Capacity Lithium-Ion Batteries Caused by Charge and Discharge’, J Am Ceram Soc, 2011, 94, pp. S226-S235

46 Bower, A.F., and Guduru, P.R.: ‘A simple finite element model of diffusion, finite deformation, plasticity and fracture in lithium ion insertion electrode materials’, Model Simul Mater Sc, 2012, 20, (4), pp. 045004

47 Hasselman, D.P.H.: ‘Elastic Energy at Fracture and Surface Energy as Design Criteria for Thermal Shock’, J Am Ceram Soc, 1963, 46, (11), pp. 535-540

48 Bhandakkar, T.K., and Gao, H.J.: ‘Cohesive modeling of crack nucleation under diffusion induced stresses in a thin strip: Implications on the critical size for flaw tolerant battery electrodes’, International Journal of Solids and Structures, 2010, 47, (10), pp. 1424-1434

49 Grantab, R., and Shenoy, V.B.: ‘Pressure-Gradient Dependent Diffusion and Crack Propagation in Lithiated Silicon Nanowires’, J Electrochem Soc, 2012, 159, (5), pp. A584-A591

50 Zhang, F., Bower, A.F., and Curtin, W.A.: ‘Finite element implementation of a kinetic model of dynamic strain aging in aluminum-magnesium alloys’, International Journal for Numerical Methods in Engineering, 2011, 86, (1), pp. 70-92

51 Bouchard, P.O., Bay, F., Chastel, Y., and Tovena, I.: ‘Crack propagation modelling using an advanced remeshing technique’, Comput Method Appl M, 2000, 189, (3), pp. 723-742

52 Hu, Y.H., Zhao, X.H., and Suo, Z.G.: ‘Averting cracks caused by insertion reaction in lithium-ion batteries’, J Mater Res, 2010, 25, (6), pp. 1007-1010

53 Sofronis, P., and Lufrano, J.: ‘Interaction of local elastoplasticity with hydrogen: embrittlement effects’, Mat Sci Eng a-Struct, 1999, 260, (1-2), pp. 41-47

54 Wu, C.H.: ‘The role of Eshelby stress in composition-generated and stress-assisted diffusion’, Journal of the Mechanics and Physics of Solids, 2001, 49, (8), pp. 1771-1794

55 Limthongkul, P., Jang, Y.I., Dudney, N.J., and Chiang, Y.M.: ‘Electrochemically-driven solid-state amorphization in lithium-silicon alloys and implications for lithium storage’, Acta Mater, 2003, 51, (4), pp. 1103-1113

56 Chon, M., Sethuraman, V., McCormick, A., Srinivasan, V., and Guduru, P.: ‘Real-Time Measurement of Stress and Damage Evolution during Initial Lithiation of Crystalline Silicon’, Phys Rev Lett, 2011, 107, (4)

57 Liu, X.H., Wang, J.W., Huang, S., Fan, F.F., Huang, X., Liu, Y., Krylyuk, S., Yoo, J., Dayeh, S.A., Davydov, A.V., Mao, S.X., Picraux, S.T., Zhang, S.L., Li, J., Zhu, T., and Huang, J.Y.: ‘In situ atomic-scale imaging of electrochemical lithiation in silicon’, Nature Nanotechnology, 2012, 7, (11), pp. 749-756

58 Wang, J.W., He, Y., Fan, F.F., Liu, X.H., Xia, S.M., Liu, Y., Harris, C.T., Li, H., Huang, J.Y., Mao, S.X., and Zhu, T.: ‘Two-Phase Electrochemical Lithiation in Amorphous Silicon’, Nano Lett., 2013, 13, (2), pp. 709-715

59 McDowell, M.T., Lee, S.W., Harris, J.T., Korgel, B.A., Wang, C.M., Nix, W.D., and Cui, Y.: ‘In Situ TEM of Two-Phase Lithiation of Amorphous Silicon Nanospheres’, Nano Lett., 2013, 13, (2), pp. 758-764

60 Kubota, Y., Escano, M.C.S., Nakanishi, H., and Kasai, H.: ‘Crystal and electronic structure of Li15Si4’, J Appl Phys, 2007, 102, (5), pp. -

61 Xu, Y.H., Yin, G.P., and Zuo, P.J.: ‘Geometric and electronic studies of Li15Si4 for silicon anode’, Electrochim Acta, 2008, 54, (2), pp. 341-345

62 Obrovac, M.N., and Christensen, L.: ‘Structural changes in silicon anodes during lithium insertion/extraction’, Electrochem. Solid State Lett., 2004, 7, (5), pp. A93-A96

63 Liu, X.H., Zhong, L., Huang, S., Mao, S.X., Zhu, T., and Huang, J.Y.: 'Size-dependent fracture of silicon nanoparticles during lithiation', Acs Nano, 2012, 6, (2), pp. 1522-1531

64 Liu, X.H., Zheng, H., Zhong, L., Huang, S., Karki, K., Zhang, L.Q., Liu, Y., Kushima, A., Liang, W.T., Wang, J.W., Cho, J.H., Epstein, E., Dayeh, S.A., Picraux, S.T., Zhu, T., Li, J., Sullivan, J.P., Cumings, J., Wang, C., Mao, S.X., Ye, Z.Z., Zhang, S., and Huang, J.Y.: 'Anisotropic swelling and fracture of silicon nanowires during lithiation', Nano Lett, 2011, 11, (8), pp. 3312-3318

65 Liu, X.H., and Huang, J.Y.: 'In situ TEM electrochemistry of anode materials in lithium ion batteries', Energ Environ Sci, 2011, 4, (10), pp. 3844-3860

66 Lee, S.W., McDowell, M.T., Choi, J.W., and Cui, Y.: 'Anomalous Shape Changes of Silicon Nanopillars by Electrochemical Lithiation', Nano Lett., 2011, 11, (7), pp. 3034-3039

67 Yang, H., Huang, S., Huang, X., Fan, F., Liang, W., Liu, X.H., Chen, L.Q., Huang, J.Y., Li, J., Zhu, T., and Zhang, S.: 'Orientation-dependent interfacial mobility governs the anisotropic swelling in lithiated silicon nanowires', Nano Lett, 2012, 12, (4), pp. 1953-1958

68 Liu, X.H., Fan, F., Yang, H., Zhang, S., Huang, J.Y., and Zhu, T.: 'Self-limiting lithiation in silicon nanowires', Acs Nano, 2013, 7, (2), pp. 1495-1503

69 Lee, S.W., McDowell, M.T., Berla, L.A., Nix, W.D., and Cui, Y.: 'Fracture of crystalline silicon nanopillars during electrochemical lithium insertion', Proceedings of the National Academy of Sciences of the United States of America, 2012, 109, (11), pp. 4080-4085

70 Chevrier, V.L., and Dahn, J.R.: 'First Principles Studies of Disordered Lithiated Silicon', J Electrochem Soc, 2010, 157, (4), pp. A392-A398

71 Huang, S., and Zhu, T.: 'Atomistic mechanisms of lithium insertion in amorphous silicon', J Power Sources, 2011, 196, (7), pp. 3664-3668

72 Sethuraman, V.A., Chon, M.J., Shimshak, M., Van Winkle, N., and Guduru, P.R.: 'In situ measurement of biaxial modulus of Si anode for Li-ion batteries', Electrochem Commun, 2010, 12, (11), pp. 1614-1617

73 Stoney, G.G.: 'The tension of metallic films deposited by electrolysis', P R Soc Lond a-Conta, 1909, 82, (553), pp. 172-175

74 Haftbaradaran, H., Soni, S.K., Sheldon, B.W., Xiao, X.C., and Gao, H.J.: 'Modified Stoney Equation for Patterned Thin Film Electrodes on Substrates in the Presence of Interfacial Sliding', J Appl Mech-T Asme, 2012, 79, (3)

75 Zhao, K.J., Wang, W.L., Gregoire, J., Pharr, M., Suo, Z.G., Vlassak, J.J., and Kaxiras, E.: 'Lithium-Assisted Plastic Deformation of Silicon Electrodes in Lithium-Ion Batteries: A First-Principles Theoretical Study', Nano Lett., 2011, 11, (7), pp. 2962-2967

76 Hertzberg, B., Benson, J., and Yushin, G.: ‘Ex-situ depth-sensing indentation measurements of electrochemically produced Si-Li alloy films’, Electrochem Commun, 2011, 13, (8), pp. 818-821

77 Shenoy, V.B., Johari, P., and Qi, Y.: ‘Elastic softening of amorphous and crystalline Li-Si Phases with increasing Li concentration: A first-principles study’, J Power Sources, 2010, 195, (19), pp. 6825-6830

78 Kim, H., Chou, C.Y., Ekerdt, J.G., and Hwang, G.S.: ‘Structure and Properties of Li-Si Alloys: A First-Principles Study’, J Phys Chem C, 2011, 115, (5), pp. 2514-2521

79 Johari, P., Qi, Y., and Shenoy, V.B.: ‘The mixing mechanism during lithiation of Si negative electrode in Li-ion batteries: an ab initio molecular dynamics study’, Nano Lett, 2011, 11, (12), pp. 5494-5500

80 Liu, X.H., Huang, S., Picraux, S.T., Li, J., Zhu, T., and Huang, J.Y.: ‘Reversible Nanopore Formation in Ge Nanowires during Lithiation-Delithiation Cycling: An In Situ Transmission Electron Microscopy Study’, Nano Lett., 2011, 11, (9), pp. 3991-3997

81 Sheldon, B.W., Soni, S.K., Xiao, X.C., and Qi, Y.: ‘Stress Contributions to Solution Thermodynamics in Li-Si Alloys’, Electrochem. Solid State Lett., 2012, 15, (1), pp. A9-A11

82 Sethuraman, V.A., Srinivasan, V., Bower, A.F., and Guduru, P.R.: ‘In Situ Measurements of Stress-Potential Coupling in Lithiated Silicon’, J Electrochem Soc, 2010, 157, (11), pp. A1253-A1261

83 Sethuraman, V.A., Srinivasan, V., and Newman, J.: ‘Analysis of Electrochemical Lithiation and Delithiation Kinetics in Silicon’, J Electrochem Soc, 2013, 160, (2), pp. A394-A403

84 Stephenson, G.B.: ‘Deformation during Interdiffusion’, Acta Metallurgica, 1988, 36, (10), pp. 2663-2683

85 Lee, E.H.: ‘Elastic-Plastic Deformation at Finite Strains’, Journal of Applied Mechanics, 1969, 36, (1), pp. 1

86 Argon, A.S., and Demkowicz, M.J.: ‘What Can Plasticity of Amorphous Silicon Tell Us about Plasticity of Metallic Glasses?’, Metallurgical and Materials Transactions A, 2008, 39, (8), pp. 1762-1778

87 Newman, J.S., and Thomas-Alyea, K.E.: ‘Electrochemical systems’ (J. Wiley, 2004, 3rd edn. 2004)

88 Christensen, J., and Newman, J.: ‘Stress generation and fracture in lithium insertion materials’, J Solid State Electr, 2006, 10, (5), pp. 293-319

89 Chandrasekaran, R., Magasinski, A., Yushin, G., and Fuller, T.F.: 'Analysis of Lithium Insertion/Deinsertion in a Silicon Electrode Particle at Room Temperature', J Electrochem Soc, 2010, 157, (10), pp. A1139-A1151

90 Golmon, S., Maute, K., Lee, S.H., and Dunn, M.L.: 'Stress generation in silicon particles during lithium insertion', Appl Phys Lett, 2010, 97, (3)

91 Li, J.C., Xiao, X.C., Yang, F.Q., Verbrugge, M.W., and Cheng, Y.T.: 'Potentiostatic Intermittent Titration Technique for Electrodes Governed by Diffusion and Interfacial Reaction', J Phys Chem C, 2012, 116, (1), pp. 1472-1478

92 Verbrugge, M.W., and Cheng, Y.T.: 'Stress and Strain-Energy Distributions within Diffusion-Controlled Insertion-Electrode Particles Subjected to Periodic Potential Excitations', J Electrochem Soc, 2009, 156, (11), pp. A927-A937

93 Tang, M., Carter, W.C., Belak, J.F., and Chiang, Y.M.: 'Modeling the competing phase transition pathways in nanoscale olivine electrodes', Electrochim Acta, 2010, 56, (2), pp. 969-976

94 Tang, M., Carter, W.C., and Chiang, Y.M.: 'Electrochemically Driven Phase Transitions in Insertion Electrodes or Lithium-Ion Batteries: Examples in Lithium Metal Phosphate Olivines', Annual Review of Materials Research, Vol 40, 2010, 40, pp. 501-529

95 Tang, M., Huang, H.Y., Meethong, N., Kao, Y.H., Carter, W.C., and Chiang, Y.M.: 'Model for the Particle Size, Overpotential, and Strain Dependence of Phase Transition Pathways in Storage Electrodes: Application to Nanoscale Olivines', Chem Mater, 2009, 21, (8), pp. 1557-1571

96 Purkayastha, R., and McMeeking, R.M.: 'A Linearized Model for Lithium Ion Batteries and Maps for their Performance and Failure', J Appl Mech-T Asme, 2012, 79, (3), pp. 031021

97 Larche, F.C., and Cahn, J.W.: 'The Interactions of Composition and Stress in Crystalline Solids', Acta Metallurgica, 1985, 33, (3), pp. 331-357

98 Yang, B., He, Y.P., Irsa, J., Lundgren, C.A., Ratchford, J.B., and Zhao, Y.P.: 'Effects of composition-dependent modulus, finite concentration and boundary constraint on Li-ion diffusion and stresses in a bilayer Cu-coated Si nano-anode', J Power Sources, 2012, 204, pp. 168-176

99 Zhang, X.C., Shyy, W., and Sastry, A.M.: 'Numerical simulation of intercalation-induced stress in Li-ion battery electrode particles', J Electrochem Soc, 2007, 154, (10), pp. A910-A916

100 Abu Al-Rub, R.K., and Voyiadjis, G.Z.: 'A direct finite element implementation of the gradient-dependent theory', International Journal for Numerical Methods in Engineering, 2005, 63, (4), pp. 603-629

101 Zienkiewicz, O.C., Taylor, R.L., and Zhu, J.Z.: ‘The finite element method its basis and fundamentals’ (Elsevier Butterworth-Heinemann, 2005, 6th edn. 2005)

102 Luscher, D.J., McDowell, D.L., and Bronkhorst, C.A.: ‘A second gradient theoretical framework for hierarchical multiscale modeling of materials’, Int J Plasticity, 2010, 26, (8), pp. 1248-1275

103 Shu, J.Y., King, W.E., and Fleck, N.A.: ‘Finite elements for materials with strain gradient effects’, International Journal for Numerical Methods in Engineering, 1999, 44, (3), pp. 373-391

104 Borja, R.I., Tamagnini, C., and Alarcon, E.: ‘Elastoplastic consolidation at finite strain - Part 2: Finite element implementation and numerical examples’, Comput Method Appl M, 1998, 159, (1-2), pp. 103-122

105 Hughes, T.J.R., and Winget, J.: ‘Finite Rotation Effects in Numerical-Integration of Rate Constitutive-Equations Arising in Large-Deformation Analysis’, International Journal for Numerical Methods in Engineering, 1980, 15, (12), pp. 1862-1867

106 Chevrier, V.L., and Dahn, J.R.: ‘First Principles Model of Amorphous Silicon Lithiation’, J Electrochem Soc, 2009, 156, (6), pp. A454-A458

107 Timoshenko, S.: ‘Theory of elasticity’ (McGraw-Hill, 1951, 2d edn. 1951)

108 Szabadi, M., Hess, P., Kellock, A.J., Coufal, H., and Baglin, J.E.E.: ‘Elastic and mechanical properties of ion-implanted silicon determined by surface-acoustic-wave spectrometry’, Phys Rev B, 1998, 58, (14), pp. 8941-8948

109 Ding, N., Xu, J., Yao, Y.X., Wegner, G., Fang, X., Chen, C.H., and Lieberwirth, I.: ‘Determination of the diffusion coefficient of lithium ions in nano-Si’, Solid State Ionics, 2009, 180, (2-3), pp. 222-225

110 Kelly, A.: ‘Strong solids’ (Clarendon Press, 1973, 2d edn. 1973)

111 Yu, H.H., and Suo, Z.: ‘Stress-dependent surface reactions and implications for a stress measurement technique’, J Appl Phys, 2000, 87, (3), pp. 1211-1218

112 Pell, E.M.: ‘Diffusion of Li in Si at High-T and the Isotope Effect’, Physical Review, 1960, 119, (3), pp. 1014-1021

113 Ruffo, R., Hong, S.S., Chan, C.K., Huggins, R.A., and Cui, Y.: ‘Impedance Analysis of Silicon Nanowire Lithium Ion Battery Anodes’, J Phys Chem C, 2009, 113, (26), pp. 11390-11398

114 Xie, J., Imanishi, N., Zhang, T., Hirano, A., Takeda, Y., and Yamamoto, O.: ‘Li-ion diffusion in amorphous Si films prepared by RF magnetron sputtering: A comparison of

using liquid and polymer electrolytes', Materials Chemistry and Physics, 2010, 120, (2-3), pp. 421-425

115 Soni, S., Sheldon, B., Xiao, X., and Tokranov, A.: 'Thickness effects on the lithiation of amorphous silicon thin films', Scripta Materialia, 2011, 64, (4), pp. 307-310

116 Kao, Y., Tang, M., Meethong, N., Bai, J., Carter, W., and Chiang, Y.: 'Overpotential-Dependent Phase Transformation Pathways in Lithium Iron Phosphate Battery Electrodes', Chem Mater, 2010, 22, (21), pp. 5845-5855

117 Garcia, R.E., Chiang, Y.M., Carter, W.C., Limthongkul, P., and Bishop, C.M.: 'Microstructural modeling and design of rechargeable lithium-ion batteries', J Electrochem Soc, 2005, 152, (1), pp. A255-A263

118 Van der Ven, A., Garikipati, K., Kim, S., and Wagemaker, M.: 'The Role of Coherency Strains on Phase Stability in Li[sub x]FePO[sub 4]: Needle Crystallites Minimize Coherency Strain and Overpotential', J Electrochem Soc, 2009, 156, (11), pp. A949

119 Cogswell, D.A., and Bazant, M.Z.: 'Coherency strain and the kinetics of phase separation in LiFePO4 nanoparticles', Acs Nano, 2012, 6, (3), pp. 2215-2225

120 Aziz, M.J., Sabin, P.C., and Lu, G.Q.: 'The activation strain tensor: Nonhydrostatic stress effects on crystal-growth kinetics', Physical review. B, Condensed matter, 1991, 44, (18), pp. 9812-9816

121 Chen, X.H.: 'Coupled hygro-thermo-viscoelastic fracture theory', International Journal of Fracture, 2007, 148, (1), pp. 47-55

122 Zhou, M., Ravichandran, G., and Rosakis, A.J.: 'Dynamically propagating shear bands in impact-loaded prenotched plates .2. Numerical simulations', Journal of the Mechanics and Physics of Solids, 1996, 44, (6), pp. 1007

123 Nakamura, T., Shih, C.F., and Freund, L.B.: 'Computational Methods Based on an Energy Integral in Dynamic Fracture', International Journal of Fracture, 1985, 27, (3-4), pp. 229-243

124 Li, Y., and Zhou, M.: 'Prediction of Fracture Toughness of Ceramic Composites as Function of Microstructure: I. Numerical Simulations', Journal of the Mechanics and Physics of Solids, 2013, 61, pp. 472-488

125 Kondepudi, D.K., and Prigogine, I.: 'Modern thermodynamics : from heat engines to dissipative structures' (John Wiley, 1998. 1998)

126 Moran, B., and Shih, C.F.: 'Crack Tip and Associated Domain Integrals from Momentum and Energy-Balance', Engineering Fracture Mechanics, 1987, 27, (6), pp. 615-642

127 Moran, B., and Shih, C.F.: 'A General Treatment of Crack Tip Contour Integrals', International Journal of Fracture, 1987, 35, (4), pp. 295-310

128 Freund, L.B.: 'Dynamic fracture mechanics' (Cambridge University Press, 1990. 1990)

129 Carka, D., McMeeking, R.M., and Landis, C.M.: 'A Note on the Path-Dependence of the J-Integral Near a Stationary Crack in an Elastic-Plastic Material With Finite Deformation', J Appl Mech-T Asme, 2012, 79, (4), pp. 044502

130 Shih, C.F., Moran, B., and Nakamura, T.: 'Energy-Release Rate Along a 3-Dimensional Crack Front in a Thermally Stressed Body', International Journal of Fracture, 1986, 30, (2), pp. 79-102

131 Heuer, A.H., Lange, F.F., Swain, M.V., and Evans, A.G.: 'Transformation Toughening - an Overview', J Am Ceram Soc, 1986, 69, (3), pp. R1-R4

132 Soni, S.K., Sheldon, B.W., Xiao, X.C., Verbrugge, M.W., Ahn, D., Haftbaradaran, H., and Gao, H.J.: 'Stress Mitigation during the Lithiation of Patterned Amorphous Si Islands', J Electrochem Soc, 2012, 159, (1), pp. A38-A43

133 Sethuraman, V.A., Van Winkle, N., Abraham, D.P., Bower, A.F., and Guduru, P.R.: 'Real-time stress measurements in lithium-ion battery negative-electrodes', J Power Sources, 2012, 206, pp. 334-342

134 Anderson, T.L.: 'Fracture mechanics : fundamentals and applications' (Taylor & Francis, 2005, 3rd edn. 2005)

135 Aoki, S., Kishimoto, K., and Sakata, M.: 'Elastic-Plastic Analysis of Crack in Thermally-Loaded Structures', Engineering Fracture Mechanics, 1982, 16, (3), pp. 405-413

136 Pinson, M.B., and Bazant, M.Z.: 'Theory of SEI Formation in Rechargeable Batteries: Capacity Fade, Accelerated Aging and Lifetime Prediction', J Electrochem Soc, 2012, 160, (2), pp. A243-A250

137 Doyle, M., Fuller, T.F., and Newman, J.: 'Modeling of Galvanostatic Charge and Discharge of the Lithium Polymer Insertion Cell', J Electrochem Soc, 1993, 140, (6), pp. 1526-1533

138 Fuller, T.F., Doyle, M., and Newman, J.: 'Simulation and Optimization of the Dual Lithium Ion Insertion Cell', J Electrochem Soc, 1994, 141, (1), pp. 1-10

139 Christensen, J.: 'Modeling Diffusion-Induced Stress in Li-Ion Cells with Porous Electrodes', J Electrochem Soc, 2010, 157, (3), pp. A366-A380

140 Garcia, R.E., and Chiang, Y.M.: 'Spatially resolved modeling of microstructurally complex battery architectures', J Electrochem Soc, 2007, 154, (9), pp. A856-A864

141 Purkayastha, R.T., and McMeeking, R.M.: ‘An integrated 2-D model of a lithium ion battery: the effect of material parameters and morphology on storage particle stress’, Comput Mech, 2012, 50, (2), pp. 209-227